Synthesis and electrochemical applications of boron- and phosphorus-doped carbon nanotubes

Dissertation

zur Erlangung des akademischen Grades
Doctor rerum naturalium

vorgelegt der Fakultät für Mathematik und Naturwissenschaften
der Technische Universität Ilmenau

von
Yudi Nugraha Thaha
geboren am 16. März 1980 in Bandung. Indonesia

vorgelegt am: 14.09.2017

Gutachter: 1. PD Dr. rer. nat. habil. Nikos Tsierkezos
2. Prof. Dr. rer. nat. habil. Stefan Krischok
3. Prof. Dr.habil. Paweł Szroeder

Verteidigung am: 31.01.2018

urn:nbn:de:gbv:ilm1-2018000035

Acknowledgements

I would like to express my deepest gratitude to my supervisors, apl. Prof. Dr. rer. nat. habil. Uwe Ritter, and PD Dr. rer. nat. habil. Nikos Tsierkezos for their encouragement, guidance, incredible support, and for sharing with me their experience and knowledge during my graduate research.

I would like to thank Univ.-Prof. Dr. rer. nat. habil. Dr. h.c. Prof. h.c. Peter Scharff and all of our research group members, Dr. rer. nat. Eric Täuscher, Sabine Heusing, Doreen Schneider, Carmen Siegmund, Katrin Risch, Susann Günther, and Yvone Raab for their help, kindness, and support during my graduate research at Technische Universität Ilmenau.

I would like to thank Dr. Marcel Himmerlich for the XPS analysis, Dr. Eoin K. McCarthy (CRANN. Trinity College Dublin) for the SEM and TEM measurements, Dr. habil. Paweł Szroeder (Nicolaus Copernicus University in Torun) for Raman spectroscopy measurements and Lars Hafferman for the synthesis of gold nanoparticles.

I am very grateful to have been able to work with numerous people who have provided support and assistance during my experimental research. I would like to thank Shereen Haj Othman, Max Puschner, Natalia Root, and Martin Kopa for the discussion, help and support during my research activities at Technische Universität Ilmenau.

I would like to thank the Indonesian student community in Ilmenau. Specially thanks to Kadek Dwi Cahaya Putra, Mirko Ante, and Diza Dirgantara for our friendship, I wish them every success in the future.

I would also like to acknowledge the funding I received from the Ministry of research, technology and higher education Republic of Indonesia and the RISET-PRO program.

Finally, I would like to thank all the members of my family, Toha D Kostana, Een Yumaeni, Dina Oktavia, Kyaneva Aisha Thaha, Herztimi Ahmed Thaha, Hendrayana Thaha, Fika Permata Thaha, Gaffarudin, Mardiana, for their invaluable support, love, and encouragement. I dedicate my thesis to my lovely wife, daughter, and son who lit up my life every time.

Zusammenfassung

Bor-dotierte (B-MWCNT) und Phosphor-dotierte (P-MWCNT) Kohlenstoffnanoröhren wurde mittels chemischer Gasphasenabscheidungstechnik erfolgreich hergestellt. Durch die Verwendung unterschiedlicher Kohlenstoffquellen und Dotierungsmitteln zeigen die Phosphor- und Bor-dotierten MWCNTs unterschiedliche Strukturen. Dabei treten neben vertikal ausgerichteten, hohlen vertikal ausgerichteten, Y-förmige auch horizontal orientierte Nanoröhren auf. Die dotierten MWCNTs wurden unter Verwendung von Raman-Spektroskopie,Rasterelektronenmikroskopie,Transmissionselektronenmikroskopie (in Kombination mit Elektronenenergieverlustspektroskopie) und Röntgen-Photoelektron Spektroskopie umfassend charakterisiert. Neben der physikalischen Charakterisierung wurden sowohl die B-MWCNTs als auch die P-MWCNTs elektrochemisch untersucht, indem als Modellredoxsystem $[Fe(CN)_6]^{3-/4-}$ in KCl Lösung angewendet wurde. Die hergestellten Elektroden wurden dann für das biologisch relevante Dopamin/Dopaminchinone Redox-System (in Phosphatpufferlösung, pH=7) angewendet. Hierfür wurden sowohl die Zyklische Voltametrie als auch die Elektrochemische Impedanz Spektroskopie verwendet. Im Folgenden wurden die Effekte der Oberflächen-funktionalisierung mit Goldnanopartikeln (AuNP), Oxidation mit Piranha Lösung und Säurebehandlung mit HCl auf die elektrochemischen Eigenschaften von B-MWCNTs und P-MWCNTs studiert. Auch hier wurde sowohl das Modellesystem $[Fe(CN)_6]^{3-/4-}$ als auch der Anwendungsfall mit dem Dopamin/Dopaminchinone Redoxsystem betrachtet. Die Ergebnisse zeigen, dass das elektrochemische Verhalten von B-MWCNTs und P-MWCNTs stark durch die Nanoröhrenstruktur und Konfiguration (einzelne Nanoröhren oder Cluster- Nanoröhren), sowie durch die Anwesenheit von amorphen Kohlenstoffstrukturen auf der Nanoröhrenoberfläche beeinflusst wird. Y-förmige B-MWCNTs zeigen einen schnelleren Elektronentransfer im Vergleich zu vertikal ausgerichteten dotierten B-MWCNTs und P-MWCNTs welche teilweise mit amorphen Kohlenstoffstrukturen bedeckt sind. Die Kinetik für den Elektronentransfer auf Y-förmige B-MWCNTs und P-MWCNTs mit Kohlenstoff auf der Oberfläche lässt sich durch den Einsatz von AuNP weiter verstärken.

Abstract

The catalytic chemical vapor deposition method was applied for the synthesis of B-MWCNTs and P-MWCNTs. P-MWCNTs and B-MWCNTs with different structures, namely vertically aligned, hollow vertically aligned, Y-shaped and horizontally oriented nanotubes were produced by using different doping and carbon source materials. The B-MWCNTs and P-MWCNTs were characterized using Raman spectroscopy, scanning electron microscopy, transmission electron microscopy in combination with electron energy loss spectroscopy and X-ray photo electron spectroscopy. The B-MWCNTs and P-MWCNTs were electrochemically studied by using either $[Fe(CN)_6]^{3-/4-}$ redox system in KCl solution or dopamine/dopamine quinone redox system in phosphate buffer solution (pH=7) by means of cyclic voltammetry and electrochemical impedance spectroscopy. The effects of surface functionalisation with AuNPs, oxidation with piranha solution, and acid treatment with HCl on the electrochemical response of B-MWCNTs and P-MWCNTs towards $[Fe(CN)_6]^{3-/4-}$ and dopamine/dopamine quinone were also studied. The results demonstrated that the electrochemical behaviour of B-MWCNTs and P-MWCNTs is strongly influenced by the nanotubes structure and configuration (sole nanotube or cluster nanotubes) as well as by the presence of reaction by-product on the nanotube surface such as carbon cluster and onion-like carbon. Y-shaped B-MWCNTs show faster electron transfer compared to either vertically aligned B-MWCNTs or P-MWCNTs with nanographitic carbon cluster. The kinetic for electron transfer on Y-shaped B-MWCNTs and P-MWCNTs with nanographitic carbon cluster enhances upon AuNPs functionalisation.

Abbreviations

BA	Boric acid
B-MWCNTs	Boron doped multi-walled carbon nanotubes
CV	Cyclic Voltammetry
CVD	Chemical vapor deposition
DOPA	Dopamine
EDX	Energy-dispersive X-ray spectroscopy
EELS	Electron energy loss spectroscopy
EIS	Electrochemical impedance spectroscopy
$FeCp_2$	Ferrocene
FWHM	Full width half maximum
HOPG	Highly oriented pyrolytic graphite
MWCNTs	Multi-walled carbon nanotubes
P-MWCNTs	Phosphorus doped multiwalled carbon nanotubes
SEM	Scanning electron microscopy
SWCNTs	Single walled carbon nanotubes
TEB	Triethyl borate
TEM	Transmission electron microscopy
TPP	Triphenyl phosphine
XPS	X-ray photoelectron spectroscopy
UV-VIS	Ultraviolet–visible

Table of Contents

Introduction and motivation

Carbon is one of the most widely used materials in electrochemistry and utilised across a wide range of applications starting from metals production, energy storage, energy conversion to electroanalysis. Carbon-based electrodes are available in a wide range of electrode sizes from submicron electrodes to electrodes with areas in square meters [1]. Carbon has relatively inert electrochemistry, low background current, and rich surface chemistry. It can be prepared with different functionalities and affinities to increase its sensitivity and selectivity [2].

In electroanalysis, carbon-based electrodes allow for the scanning of more negative potential than platinum or gold and have a large anodic potential window [2]. Performance improvement and better utilisation of carbons in electrochemical applications are needed to achieve more reliable measurement in detection limit, increased sensitivity, and improved selectivity of the electrode in an electrochemical sensor.

Carbon has an electron configuration of $1s^2$ $2s^2$ $2p^2$. Carbon has the ability to form many allotropes. Carbon allotropes are available in various crystallographic structures, ranging from a simple graphite-like structure to a complex structure. Graphite, graphene, diamond, fullerene, and carbon nanotubes are the well-known allotropes of carbon [3]. Each carbon allotrope shows different physical and chemical properties. The difference among these carbon allotropes is the relative density of the edge and basal planes of the surface which influences the electrochemical reactivity on the electrode surface [4].

Because of the various types of chemical bonding in their lattice network, the surface chemistry of carbon materials is significantly more complex than metals [2]. Since the kinetic and chemical reactivity of electrodes is an interfacial surface reaction, the structure an the electrochemical and physicochemical properties of the carbon surface are obviously important.

Carbon nanotubes (CNTs) are part of the fullerene family of carbon allotropes. A single walled carbon nanotube (SWCNT) can be viewed as a sheet of graphene rolled into a cylinder, whereas multi-walled carbon nanotubes (MWCNTs) are multiple concentric cylinders of rolled up graphene, separated by nearly the same distance as the interlayer spacing of graphite (0.34 nm) [5]. MWCNTs exist in several morphological variations depending on the production parameter. MWCNTs can be formed as a hollow tube, herringbone, or as a bamboo-like structure.

Carbon nanotubes are attractive because of their structures and electrochemical properties. The super hydrophobic properties of MWCNTs minimise the fouling of the electrode surface [6]. MWCNTs have remarkable properties to mediate fast electron-transfer kinetics for a wide range of electroactive species [7]. They also have high conductivity and a high aspect ratio, which help them to form a network of high sensitivity conductive tubes.

The conductivity of CNTs and graphene is related to their sp^2 hybridisation and density of states. In sp^2 hybridisation of CNTs and graphene, only three of the four valence electrons of a carbon atom are used in a sigma bond. It is possible for the other electrons in the p orbital to overlap with other p orbitals from their neighbour and move freely within the localised π orbitals. CNTs and graphene show good conductivity in the planar direction. Compared to CNTs, diamond has a face center cubic structure with sp^3 hybridisation. Having a very large 5.5 eV energy gap, diamond demonstrates low conductivity and high resistivity [8]. Due to their poor electrical conductivity, most diamonds are rarely used as electrode material. Boron, nitrogen, and phosphorus are usually used for the doping to increase the conductivity of diamond [9].

Although CNTs have relatively inert electrochemistry, studies revealed that the electronic properties of CNTs are sensitive to surface adsorption of various molecules [10]. These important properties form the basis of most electrochemical sensors based on chemo resistance and conductometry in electroanalysis. MWCNTs exhibit a higher adsorption capacity than SWCNT. High orientation MWCNTs have high electron transfer and specific capacitance than SWCNT [11].

Because of their capability to form various hybridisation sp, sp^2 and sp^3, carbon atoms in the MWCNTs structure are able to arrange themselves into a variety of different polygons, not just hexagons to form different structures. The theoretical calculation of a non-hexagonal structure in an atomic carbon network permits the formation of a dangling bond and generates a vacancy in the CNTs structure [12]. Theoretical simulations show that defects, associated with dangling bonds, should enhance the reactivity of CNTs sidewall [13].

The forces that govern the adsorption of molecules to CNTs are strongly influenced by the structure of the carbon atoms in the lattice network, the surface functional groups, and the structure of adsorbates. The interactions between the CNTs surface-adsorbate that control adsorption precipitation mechanism include electrostatic, hydrophobic effects, dipole-dipole interactions, induced dipoles, and covalent bonds [14]. Adsorption of molecule and nanoparticle can dramatically influence the reactivity and electrocatalytic activity of CNTs electrode [15].

CNTs are anisotropic material, which implies different properties in different directions. The side walls of an MWCNTs structure can be compared to the graphite basal plane of highly oriented pyrolytic graphite (HOPG) and the open end corresponds to the edge plane (HOPG). MWCNTs and HOPG are different in geometric shapes. MWCNTs are even more sensitive to adsorbate than HOPG surface [16]. The electrical conductivity of the carbon nanotube is anisotropic [17]. CNTs have the highest aspects ratio edge/basal plane, compared to graphite and amorphous carbon. The upper part of CNTs relate to the edge plane of HOPG, whereas the tube walls have been linked with the basal plane HOPG [18]. The observed reactivity of CNTs is strongly influenced by defect density in basal plane and edge planes. The defect density of CNTs can be modified by doping and radiation [19].

In a simple structural consideration, it has been suggested that CNTs can be regarded as having the perfect hexagonal carbon network. Substitutions of carbon atoms in the hexagonal network will generate some defects in the hexagonal network. The presence of defects in the hexagonal network of CNTs affects the materials properties such as the electronic structure, optical absorption, chemical reactivity, as well as mechanical properties [16].

MWCNTs are structurally equivalent to multiple sheets of graphene rolled into a tube. Conduction in MWCNTs occurs via the delocalised π-electron system. Since phosphorus has five valence electrons, boron has three valence electrons, and carbon has four valence electrons, the substitution of carbon atoms in the honeycomb lattice of an MWCNT by phosphorus and boron atoms will, in general, change the local hybridisation of sp^2 bond of MWCNTs. Dopant atoms modify the local electronic structure sp^2 bond carbon materials and change the basal plane structure of MWCNTs. The substitution of an atom in different size into the basal plane of the carbon nanotube will damage the perfect hexagonal carbon structure in sp^2 conjugated graphene sheets, mediate vacancy, and produce Stone-Wales defects [20].

The aspects of nanotube production, structure, defects, and the additional of electron mediators have to be considered to obtain a better relationship among the CNTs structure, the production parameter, and their electrochemical properties.

The overall objective of the present works includes the production of P-MWCNTs and B-MWCNTs, their electron microscopic, their Raman spectroscopic, and their electrochemical properties. Electrochemical characterisation by means of cyclic voltammetry and electrochemical impedance spectroscopic was done in order to study the interplaying relationship between the sidewall structure, defect, nanoparticle, sidewall-end tube functionalisation and the electrochemical properties of MWCNTs.

Chapter 1
Literature review

1.1. Carbon nanotubes

Carbon nanotubes are cylindrical molecules of carbon with a diameter of 1-100 nm. The electrochemistry of carbon nanotube represents one of the most interesting researches in carbon material. CNTs based electrodes exhibit higher sensitivities, lower limits of detection, and faster electron transfer kinetics compared to traditional electrodes [21].

The key feature of CNTs electrochemical reactivity is the curvature of the graphene sheet in the nanotubes. The uniform distribution of electron clouds around the C-C backbone in graphite is transformed into an asymmetric distribution, both inside and outside the cylindrical sheet in CNTs. When the electron clouds are distorted, a rich π-electron conjugation is formed outside the tube, resulting to higher surface activity of carbon nanotubes [22]. The hetero atom doping of MWCNTs has become an interesting subject of study, since it leads to power full controllability chemical properties of MWCNTs [23]. Consequently, there is a great interest for developing new synthesis methods for the production of new types of doped MWCNTs with different chemical properties. In this chapter, the structure, the effect of production parameters, and the electrochemical properties of CNTs are discussed.

1.1.1. Structure

A CNTs can be seen as cylinder isomers of large fullerene which is a planar-hexagonal arrangement of carbon atoms distributed in a honeycomb lattice. Structurally, CNTs can be classified into two basic forms, namely SWCNTs and MWCNTs. SWCNTs can be considered as the seamless wrapping of a single layer of graphene, whereas MWCNTs are the seamless wrapping of several concentric tubes of graphitic layers

CNTs and graphite are constructed from the same basic units, hexagons of sp^2-hybridised carbon atoms. The main difference of graphite and CNTs is the character of the C-C bonding. Due to the curvature of CNTs, the physicochemical C-C bonding of CNTs is pyramidalised, whereas C-C bonding of graphite is un-pyramidalised. Curvature in the nanotube introduces misalignment of p-orbitals within the graphene sheet. The distortion of the electron cloud generated by the curvature yields a rich π-electron conjugation outside the tube and improves the electrochemical properties of CNTs.

A SWCNT can be assumed as a rolled up sheet of graphene at a certain chiral angle with respect to a plane perpendicular to the tube's long axis. The tube chirality of SWCNT represents the atomic structure of nanotubes. The tube chirality can be defined by a chiral vector that is determined by the relation $R = na_1+ma_2$, where n and m are integers and a_1 and a_2 are the unit cell vectors of the two-dimensional lattice of graphene sheets. When m is equal to 0, the nanotubes are called zigzag nanotubes, and when *n* is equal to *m*, the nanotubes are called armchair nanotubes and when m is not equal to n, the nanotubes are called chiral (Figure 1.1) [24].

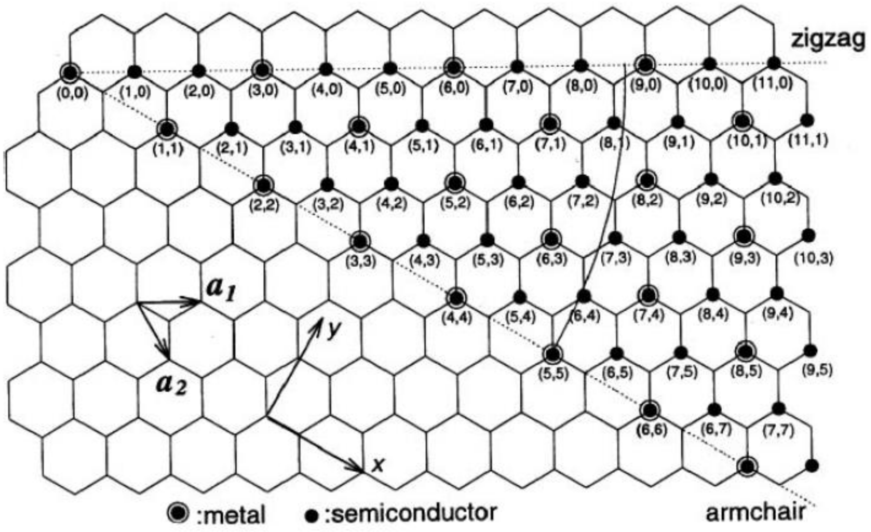

Figure 1.1 Vector notation for different chirality structure [24].

MWCNTs consist multiple rolls of concentric graphene sheets. Each graphitic shell has a specific chirality index. The structural defects and the random distribution of chirality of each concentric graphitic shell make the MWCNTs properties different from SWCNTs. The structure of MWCNTs can be described in the various models: Swiss roll, Russian doll, and mix between Russian doll and Swiss roll. In the Russian doll model, sheets of rolled graphene are arranged in a concentric cylinder. In the Swiss roll model, a sheet of graphene is rolled, resembling a spiral or a parchment (Figure 1.2) [25–27].

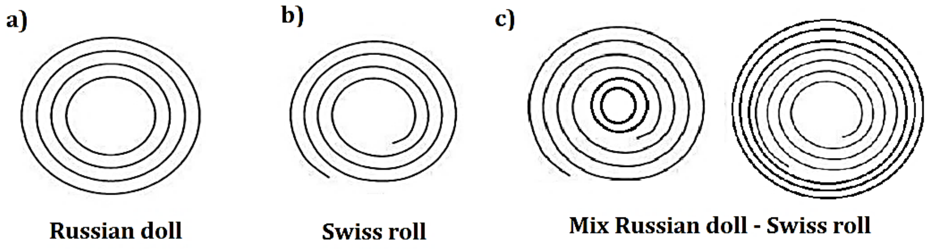

Figure 1.2 Layer model of MWCNTs [25,27].

1.1.2. General description of CNTs defects

The defect in CNTs is strongly related to the defect in a graphene sheet. Defect-free carbon nanotubes are an idealisation. Defect-free carbon nanotubes exhibit a perfection of periodical crystal structure, the carbon atom positions arrange on repeating fixed distances. Thermodynamically, it is almost impossible to obtain zero defect density even in its highly pure crystalline system. The atom vibrations still occur even at zero temperature. The higher the temperature, the more the increase in the amplitude of its atomic vibration. CNTs defects can be distinguished into the following dimension:

1. 0D zero dimension or point defect: vacancy, interstitial, impurities, re-hybridisation, Stone-Wales defect.
2. 1D linear defects: dislocation, edge, screw.
3. 2D surface defect: grain boundaries.
4. 3D bulk defect: voids, cracks.

Defects in CNTs can be intrinsic or extrinsic. Extrinsic defects are the perturbation of the crystalline order of CNTs with the presence of foreign atoms. Intrinsic defects refer to crystalline perturbation without foreign atoms. The intrinsic defect is created when an atom is missing from their ordinary position and form a vacancy related defect [28].

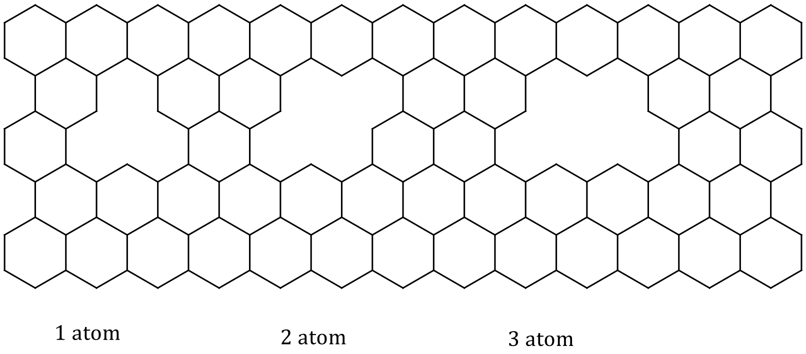

Figure 1.3 Vacancy interactions in CNTs [28].

The single vacancy is the simplest form of defect in CNTs. Missing an atom in a hexagonal network of the basal plane of CNTs is a source of a single vacancy. The coalescence of two single atom vacancies can create a double vacancy defects (Figure 1.3). The removal of more than two atoms produces more complex defect configurations. Vacancy can be produced by post synthesis of CNTs through high energy electron or neutron radiation. The presence of foreign atoms with different valences can also introduce a vacancy in a carbon hexagonal network. Vacancy can also originate from the interaction of some dangling bonds. Vacancy can be obtained by the interaction of some pentagonal structures in the hexagonal network of carbon nanotubes. It was reported that the higher defects concentration in the wall structure and at the end of the MWCNTs exhibited the higher reactivity toward thermal oxidation [29].

An interstitial defect in CNTs occurs when a small radius atom sits in an interstitial hole in a carbon lattice. The interstice of a small atom in the centre of a carbon hexagon requires a prohibitively high energy. The energetically favoured position of the intercalation is between two carbon atom bonds or in a bridge configuration. The presence of vacancies facilitates interstitial small atoms such as hydrogen in the CNTs hexagonal network [30].

There are many possible interactions between impurities and CNTs, such as chemisorption, physical adsorption, and substitutional impurities. The interaction between impurities and CNTs is strongly affected by the bonding between the impurities and the hexagonal network of CNTs. Van der Waals interaction is the main cause of physical adsorption. Chemisorption involves covalent bonding between the impurities and the hexagonal network of CNTs. Chemical bindings are generated on the surface of CNTs. Impurities in the form of a foreign atom can be introduced into the CNTs lattice network through substitutional doping. In this case, the doping atom replaces a carbon atom in their lattice position. Due to their ability to form stable covalent bonding, boron, phosphorus, and nitrogen are very promising for CNTs doping. Owing to the different electron valences, it is possible to create p-type CNTs and n-type CNTs by boron, phosphorus and nitrogen doping. In general, impurities in the hexagonal structure lead to the introduction of additional electronic states around the Fermi level and change the electronic structure of CNTs.

Because of its electron configuration, carbon has the flexibility to form different types of hybridisation (sp, sp^2, and sp^3). The carbon atoms in the graphene sheet of CNTs condense in a honeycomb lattice due to their sp^2 hybridisation. The substitution of the carbon atom in a hexagonal structures with a foreign atom perturbates its sp^2 hybridisation. The change from sp^2 to sp^3 hybridisation can be induced by the formation of a pentagon or a heptagon in a hexagonal network of carbon nanotubes [31].

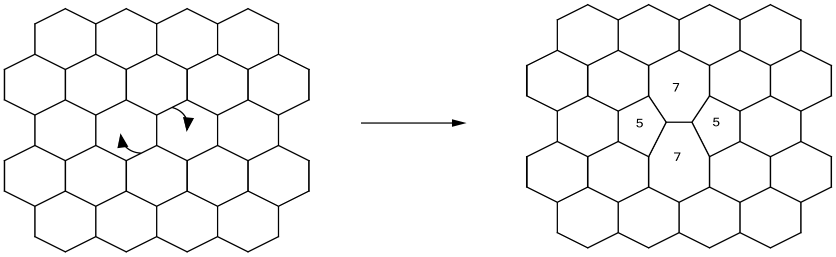

Figure 1.4 Re-arrangement of the Stone-Wales defect [32].

The presence of a geometrical size other than hexagons such as pentagon and heptagon can be seen as a local defect [31]. A single pentagon or heptagon can be considered as having a topological defect. In a graphene sheet, four hexagons can be transformed into two pentagons and two heptagons (Figure 1.4) [32]. The 5-7-7-5 configuration is known in the literature as the Stone-Wales defect [33]. The 5-7-7-5 configuration modifies topological indices (n,m) along the SWCNT. The introduction of the 5-7-7-5 defect is represented by the change of helicity of the SWCNT structure. The helicity change of SWCNT will affect the change in the electronic structure of the SWCNT[16].

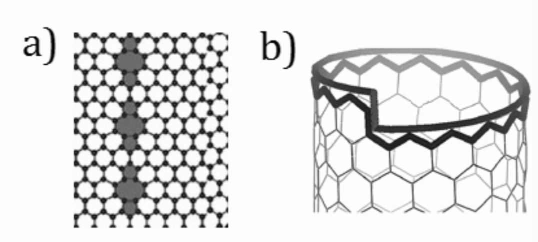

Figure 1.5 Dislocation in a).Basal plane and b).Edge plane of CNTs [34].

A dislocation in a graphene structure refers to tilt boundaries and it is separated by two domains of different lattice orientations. A Dislocation-like defect can be induced by the presence of multiple defects such as topological defect, pentagon, heptagon, and vacancies. Dislocation occurs in basal plane and edge plane of CNTs (Figure 1.5) [34]. The tubular structure of CNTs is limited by hemispherical caps at the end of the cylinder. The hemispherical caps resemble a half of fullerene. The hemispherical carbon caps contain some rings of pentagons and hexagons (Figure 1.6). Each nanotube diameter has a specific cap arrangement. The structure of a hemispherical cap determines the chirality of CNTs [35].

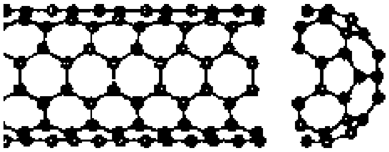

Figure 1.6 Pentagon and hexagon in nanotubes caps [35].

All dimensional defects in CNTs may influence the three-dimensional geometric structure of CNTs by causing bending, diameter changing, various types of edge plane stacking, and branch structure formation [36,37]. For instance, the coiled and the Y-shaped structure correspond with the presence of pentagon-heptagon in CNTs structure [38].

1.1.3. Production of CNTs by catalytic chemical vapor deposition

Chemical vapor deposition (CVD) is quite a promising method for producing MWCNTs. CVD allows the synthesis of MWCNTs at lower temperatures, as compared to arc discharge and laser ablation. CVD appears to be very promising because MWCNTs can be synthesized with an economically viable process in a large-scale yield based process. However, it was reported that MWCNTs synthesized by arc discharge and laser ablation show better crystallinity than

CVD synthesis [39]. The production of MWCNTs using arc furnace and laser ablation methods includes the condensation of the carbon atoms produced by source evaporation. The working temperature of arc discharge and laser ablation is similar to the melting point of graphite about 3000-4000°C, while, the synthesis temperature used in CVD is around 500-1200°C, lower than laser ablation and arc discharge [40,41].

CVD offers high efficiency and effectivity of MWCNTs fabrication. It also enables the use of various substrates and allows for the MWCNTs growth in various forms such as powder, thin film or thick film. In addition, CVD offers a better control of the growth parameters in order to synthesize the desired architecture of nanotubes on a patterned substrate. Synthesizing CNT through CVD allows to produce MWCTs in various geometric surfaces.

CVD process can be divided into a several steps series. The first is a transport of carbon source and catalyst mixture to the reaction zone, the second is a surface diffusion process and film formation, and the third is a desorption of the reactant and reaction by-products followed by transport into a bulk gas phase (Figure 1.7) [42]. The transport process involves reactant evaporation, transport via convection, and a pyrolysis of the reactant. The surface reaction process involves the adsorption of the reactant species on the substrate surface sites by surface migration, followed by catalysed surface chemical reaction between the reactant species. The CNT growth mechanism includes the pyrolysis of the carbon source over the nanoparticles surface, diffusion of carbon into nanoparticle catalyst, and the precipitation of solid carbon due to saturation in the catalyst nanoparticle.

During the MWCNTs synthesis in a CVD reactor, the precursor gas, intermediates (molecules, radicals), and final products (carbon, hydrogen and another by-product) always coexist. The interrelationships between controllable experiments and film properties in a CVD system are extremely complex. For the MWCNTs synthesis, many parameters, such as different types of carbon sources, catalyst, feeding rate, gas flow behaviour, gas carrier, gas composition, temperature, and deposition time can be controlled.

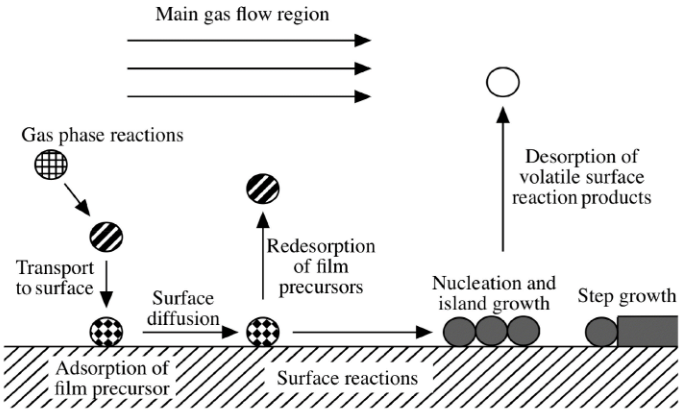

Figure 1.7 The main process in catalytical chemical vapor deposition [42].

The composition of catalyst, the temperature, and the type of carbon source material are the key points to control the CNTs synthesis. The catalyst composition and the type of carbon source material were varied in the CVD method. The lower the content of catalyst applied, the higher the content of amorphous carbon is observed; a higher content of catalyst applied results to greater quantity of residual metal nanoparticle. Amorphous carbon may appear as a product of un-catalysed pyrolysis of carbon sources, in which catalyst deactivation by amorphous carbon was reported. Catalyst deactivation leads to a decrease in the yield of CNTs [43].

The molecular structure of a carbon source has detrimental effects on the structure and characteristics of MWCNTs. For instance, in CVD experiments using C_2H_2 and C_{60} carbon precursors, it was found that C_2H_2 leads exclusively to the growth of CNTs, and in the catalyst particle size range between 25 and 500 nm. In contrast, nanotube formation from C_{60} appears only if the particle sizes are sufficiently small with an optimum condition between 20 and 30 nm [44]. The CVD of some hydrocarbons (methane, hexane, cyclohexane, benzene, naphthalene, and anthracene) over MgO-supported Fe catalyst show that the chemical structure of hydrocarbon sources related to the morphology of CNTs deposits [45]. It was reported that molecules with a linear structure such as methane, ethylene, acetylene, generally produce straight hollow CNTs [39]. On the other hand, the pyrolytic of cyclic hydrocarbons such as benzene, xylene, and cyclohexane, produces relatively curved/hunched CNTs with the tube walls often bridged inside [39]. It was also observed that an unsaturated hydrocarbon has a higher yield and higher deposition rate than saturated gas. Saturated carbon gasses tend to produce a high graphitised filament with fewer walls, compared to unsaturated gas [46]. It was reported that saturated hydrocarbons are favoured for SWCNT growth and unsaturated hydrocarbons for MWCNTs growth [46]. In some cases, the morphology of MWCNTs is not affected by carbon sources when a specific catalyst is used [46,47].

Ethanol is one of the most interesting carbon sources to produce CNTs by CVD. Since most of the metallocene catalyst can be dissolved in ethanol. In addition, for the production of CNTs, ethanol can dissolve a wide range of organic material with different functional groups for doping sources. Ethanol-based CVD enables the synthesis of various morphologies of CNTs, including random networks, vertically aligned arrays, and horizontally aligned arrays [48,49].

In situ, mass spectroscopic analysis of alcohol during CVD shows that without a catalyst, at both 800°C and 1000°C, ethanol is decomposed into C_2H_4, C_2H_3, C_2H_2, and C_2H respectively. Hydrogen and water are the other byproducts of ethanol pyrolysis. In the presence of Co/Mo catalyst, it was reported that at 600°C, ethanol pyrolysis is very active, while at 800°C, almost the entire ethanol group is decomposed [50].

A CVD study with isotope labeled ethanol by $^{13}CH_3$-$^{13}CH_2$-OH, $^{12}CH_3$-$^{12}CH_2$-OH, $^{12}CH_3$-$^{13}CH_2$-OH, $^{13}CH_3$-$^{12}CH_2$-OH shows that a carbon atom in ethanol does not contribute equally to the formation of single-walled carbon nanotubes. The second carbon atom was found to be incorporated into the SWCNT product more preferentially (up to 85%) than the first carbon. [51].

Some reports have mentioned the high yield production of CNTs with ethanol as a carbon source using various catalysts Fe, Co, Ni, Fe-Co, Fe-Ni, Fe-Mo, ferrocene, and Alumina [48,49]. Higher catalyst concentration in an ethanol solution leads to an increase of diameter of CNTs. The comparison of different aliphatic alcohol (methanol, ethanol, propanol, and butanol) in the synthesis of CNTs by CVD shows that the average diameter of CNTs varies inversely with the number of carbon atoms [52]. CVD investigation with saturated ferrocene catalyst in methanol, ethanol, propanol, butanol, pentanol, hexanol, heptanol, and decanol between 800-850 °C, shows that the length of the carbon chain in aliphatic alcohol molecules affected the product's crystallinity.

The pyrolysis of C_1-C_3 alcohol yields a product with heterogeneous morphology. The product from methanol, ethanol, and propanol contains CNT and carbon amorphous. The pyrolysis of C_4-C_5 aliphatic alcohol yields a product with more homogeneous CNT than a CNT product of C_1-C_3 aliphatic alcohol. More curved CNTs with greater and large diameters can be obtained with the decomposition of C_6-C_{10} aliphatic alcohol [53]. The comparative CVD study of alcohol and ketones using ethanol, acetone, isopropanol, and 2-butanone in a catalyst mixture of Mn and Co, impregnated in zeolite powder at 600 °C, shows that isopropanol and 2-butanone resulted in higher carbon impurities than acetone and ethanol [54].

It was reported that the morphological characteristics of CNTs produced by ethanol decomposition differ significantly from the xylene and acetylene decomposition. The addition of a small amount of ethanol to ethylene/hydrogen in CNTs synthesis using Fe/Al_2O_3 catalyst reduces the number of CNT walls without changing the outer diameter, increases the catalyst lifetime, and enhances the rate of carbon conversion [55]. The addition of alcohol to a ferrocene-xylene mixture up to a volume ratio of around 1:0,1 (xylene/alcohol) increases the average length of synthesized MWCNTs. After this optimal concentration, the increase of the alcohol content results to stronger oxidative atmosphere that hinders the MWCNTs growth [56].

The parametric study of SWCNT growth by ethanol decomposition in the presence of ferrocene catalyst indicates that the parameters such as temperature, heat transfer and substrate position in the furnace affect the morphology, the diameter and the crystallinity of nanotubes [57].

High purity SWCNTs can be formed by applying a high hydrogen flow. The high-temperature CNT synthesis studies around (1000-1200°C) using ferrocene/thiophene along with methanol, ethanol, isopropanol, and hexanol in the hydrogen-argon atmosphere show that methanol in hydrogen cannot produce any carbon product, while ethanol, isopropanol, and hexanol can produce SWCNT with amorphous carbon [58].

A catalyst plays an important role in MWCNTs synthesis. To produce MWCNTs, metal nanoparticles are commonly used to catalyse hydrocarbon pyrolysis at a lower temperature [59]. Nanoparticles have a high surface to volume ratio; whose properties are potential to provide a surface effect over bulk material. A catalyst nanoparticle has significantly depressed melting point and larger carbon solubility than a bulk catalyst [60].

A catalyst acts as an active surface in the MWCNTs growth. The nanoparticle of transition metals is considered as the most effective catalyst in the CVD synthesis of MWCNTs. The suitability of the nanoparticle of transitions metals as MWCNTs catalyst is strongly affected by some factors such as catalytic activity for the pyrolysis of the volatile organic compound, an ability to form meta stable carbides, and the ability of carbon to diffuse through and over metallic nanoparticle [61]. The active site, catalytic site and catalytic activity of the catalyst depend on the interaction among the catalyst, substrate, reactant, and temperature. Liquid nanoparticles have higher carbon solubility than solid. Thermodynamically, carbon solubility in a catalyst depends on the material of the nanoparticle, temperature, the radius of the nanoparticle and surface tension [59]. Carbon solubility in a catalyst affects the CNTs nucleation and growth in several ways, such as increasing the carbon available site for growth, creating a concentration gradient as the driving force to accelerate CNT diffusion and influencing the growth of CNT cups [62].

Iron, cobalt, and nickel are the most commonly used catalysts for CNTs fabrication [63]. The solubility of carbon at high temperature, the high carbon diffusion rate in those metals, and the adhesion between the carbon and the catalyst are the main reason for the selection of the transition metals catalyst [39]. Furthermore, the phase stability and high melting point of these transition metals offer a wide range of synthesis temperature for various precursors.

It was also reported that some organo metallocene, such as ferrocene, cobaltocene, and nickelocene show good catalytic activity for CNTs growth [64,65]. Ferrocene in high concentration has been widely used as a precursor for CNT filled ferromagnetic material [66]. A range of other metals (Cu, Pt, Pd, Mn, Mo, Cr, Au, Mg, Al) can be used as a catalyst for SWCNT growth on a quartz substrate [67]. However, the limitation of a noble metal being used to catalyse CNTs is low carbon solubility that effectively dissolves carbon when the particle size is very small (5 nm)[68]. Fe-Mo, Fe-Co, Co-Mo alloys have been used as catalysts for CNTs growth in previous studies [69–71]. Intermetallic alloy catalysts, Mo, and Co were used to increase the Fe sintering temperature. Due to chemical and thermal stability during synthesis, ceramic oxide nanoparticles like SiO_2, MgO, Al_2O_3 either in crystalline or amorphous states, are the most commonly used catalyst support for CNTs synthesis [59].

CNTs diameter represents one of the most interesting issues in CNTs synthesis. It was reported that the size of the catalyst determines the diameter and the type of CNT [72]. Investigation of growth condition by an iron nanoparticle shows that an iron nanoparticle with an average diameter of 3 nm, 9 nm and 13 nm yielded CNTs with wall diameters of 3 nm, 7 nm and 12 nm, respectively. A large diameter iron nanoparticle produces MWCNTs with two or three layer whereas a small diameter iron nanoparticle produces SWCNTs [73].

The reaction temperature is related to the kinetic and thermodynamic formation of CNTs. It has been reported that a high-temperature reaction CVD (900-1200 °C) yields SWCNT whereas a low-temperature reaction (500-900°C) favours MWCNTs growth [41]. The main effects of increasing the reaction temperature are the phase change of the catalyst, the increase in the catalyst particle size due to the sintering process, the formation of a by-product of carbon source pyrolysis, and the increase in the complexity of the carbon source vapor. Temperature has multiple effects of increasing both, the diffusion coefficient and solubility of carbon, in the metallic nanoparticle. All of those processes will be affected by the diameter of the carbon nanotube and the yield of synthesis. The higher CNTs synthesis temperature is preferred due to fewer defects and better crystallisation; however, the too high temperature is not favored because of some disadvantages such as formation of amorphous carbon and catalyst deactivation [61]. The phase transformation of the catalyst, the solid-state reaction between the catalyst and the substrate, and the solid-state reaction between the catalyst and the support lead to a growth rate reduction of CNTs because of the decreasing of catalyst surface area. The mechanisms of solid catalyst deactivation include poisoning, fouling, thermal degradation, vapor compound formation and/or leaching, accompanied by transport from the catalyst surface or particle, vapor-solid and/or solid–solid reactions, and attrition/crushing [43].

The feeding rate of carbon sources influences the synthesis duration of MWCNTs. A low feeding rate results in a low concentration of carbon source decomposition whereas a high feeding rate leads to a higher concentration of hydrocarbon decomposition. The length distribution of CNTs was influenced by the duration of the catalytic growth of a nanotube [74]. The carbon feeding rate and catalyst concentration can be used to control single- or multi-walled carbon nanotubes growth. Any excess carbon feeding rate induces disorder in the CNT structure [75]. Additionally, the laminar flow and turbulence flow of carbon source in gas phase affect the morphology of CNTs. The laminar and turbulence flows can be estimated by Reynold numbers [76].

Hydrogen prevents the poisoning of the catalyst surface by carbon deposition; hydrogen acts as an oxidising agent when it reacts with metals to form a hydride. Without a catalyst's presence, that was reported that hydrogen inhibits carbon deposition and the inhibition of carbon deposition is very sensitive as to the carbon/hydrogen ratio [77]. The studies of hydrogen concentration on CNTs morphology indicate that high concentration of hydrogen from the high conversion of methane causes the quick reduction and sintering of the iron catalyst and inhibits the nucleation of DWCNTs [78]. Hydrogen works as a reactive gas than an inert gas in carbon nanotube synthesis.

The substrate is also an important factor in the CNTs synthesis. A requirement for a substrate is thermal and chemical stability under synthesis condition. A physical and chemical interaction occurs between the catalyst, the substrate and the carbon source. The interaction mechanism includes Van der Waals forces, chemisorption, Physisorption, formation of an intermetallic compound by solid state reaction, or sintering. As reported in CNTs synthesis by alcohol catalytic chemical vapor deposition (ACCVD) on the conductive glass, porous alumina, nickel and quartz using iron and cobalt catalyst, the substrate plays an important role to determine the end of CNTs product. Successful growth of CNTs can be achieved on conducting glass, nickel plates, and porous alumina substrates. CNTs grown on conducting glass are MWCNTs. CNTs grown on nickel plates and porous alumina are SWCNTs. SWCNTs grown on nickel substrate have a higher diameter than those grown on porous alumina [79].

The formation of carbon filaments from acetylene decomposition on nickel catalyst was used as the basis of vapor liquid solid (VLS) growth model of carbon fibers [80,81]. This model was introduced in1972 [82]. In 1995, the VLS model was applied by Saito to explain the growth process of single-walled carbon nanotubes in arc discharge [83].

In the VLS mechanism, a gas, containing carbon sources, adsorbs and decomposes on the surface of the catalyst nanoparticle. Carbon, hydrogen and other molecules are formed as a decomposition product of carbon sources. The decomposed carbon diffuses within the nanoparticle to form a liquid metal carbide particle. Carbon saturation in nanoparticle occurs when the diffusion level of carbon reaches the solubility limit. Once carbon levels in the nanoparticle supersaturate, the carbon nanotube begins to grow. Depending on the diffusion process, the saturated carbon precipitate growth is often described as the tip growth or the base growth (Figure 1.8). In a tip growth model, the saturated carbon precipitate at the rear side of the nanoparticle grows to form a carbon filament in the base growth model, while the CNTs precipitate grows up with the catalyst nanoparticle rooted in the base [25]. The temperature and concentration gradient is the main driving force of the VLS mechanism [84].

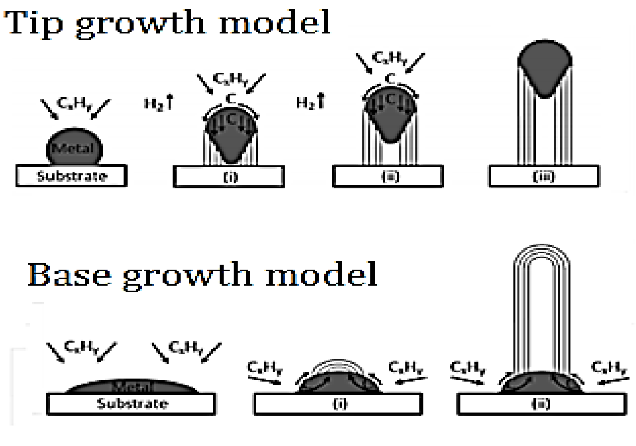

Figure 1.8 Tip growth and base growth model in vapor liquid solid [84].

The SWCNT growth mechanism cannot be directly transformed into MWCNTs, because of the simultaneous nucleation and growth of several carbon walls for MWCNT. The lifting of MWCNTs cups must be followed by the formation of additional walls and cups of MWCNTs. The carbon diffusion mechanism in the catalyst is very important to determine the growth of MWCNTs. In the nanoparticle, carbon diffusion is not only on the surface but also in the sub surface (bulk diffusion) and in the outer of few atomic layer catalysts. The formation of inner walls by bulk diffusion of the carbon in the catalyst is possible in the MWCNTs growth by VLS mechanism [80].

In a VLS mechanism, the catalyst in a liquid droplet is the core of the whole reaction in the CNTs synthesis. The morphology of CNTs is related to carbon diffusion in the catalyst nanoparticle. The process of carbon diffusion in the catalyst is reflected on the CNTs structure. Catalyst diameter size corresponds to the diameter of the CNTs. The crystalline orientation of cataslyst determines the chirality of the CNTs. The geometric feature of the catalyst depends on the activity of the catalyst surface such as dissociation mechanism, and the method of surface carbon diffusion. Surface diffusion corresponds with the hollow structure of the CNTS. In hollow CNTs, surface diffusion is preferable instead of bulk diffusion [85]. Herringbone structure is related to the diffusion in a facet geometric catalyst [86]. In a bamboo structure, bulk diffusion is responsible for carbon accumulation in the catalyst surface. [87]. Details of the comparison of the growth mechanism of hollow, herringbone, and bamboo structures can be seen in Figure 1.9.

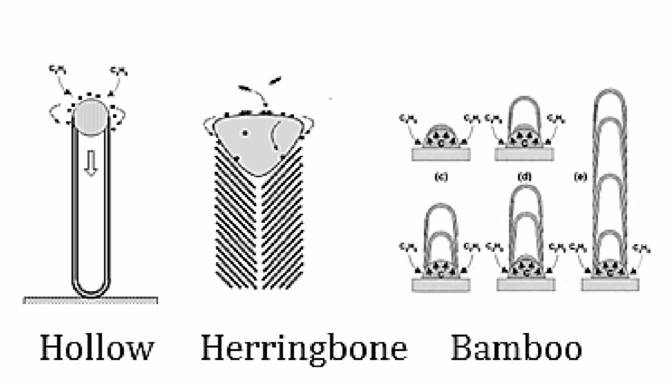

Figure 1.9 Morphology and growth mechanism of MWCNTs [85–87].

1.1.4. Doping of CNTs with boron and phosphorus.

The doping of CNTs can be endohedral, exohedral, and substitutional. In endohedral doping, the doping materials are encaged inside the CNTs structure. Exohedral doping of CNTs involves the intercalation of a small atom or molecule into available empty space of the nanotubes arrangement. Substitutional doping defines that one or several foreign atoms substitute the carbon atoms within the hexagonal network of the lattice structure of a CNT. In the sp^2 network of CNTs, it is possible to introduce some impurities as doping by replacing some carbon atoms with other elements that roughly have an atomic radius close to carbon's. It was reported that nitrogen and sulphur doping change the tubule morphology of CNT [88,89].

Theoretical studies show that the presence of foreign atoms generates structural reorganisation due to the presence of pentagon and heptagon within the sp^2 hybridised carbon lattice [90]. A boron atom contains one electron less than a carbon atom. Boron can be introduced into CNTs to manipulate their physical and chemical properties. Boron acts as p-type doping in CNTs. Since boron has a larger atomic radius than carbon, the presence of boron will result in a change in the hexagonal lattice network of CNTs. The distribution of boron inside carbon network determines the geometrical structure of the carbon nanotubes (Figure 1.10) [91].

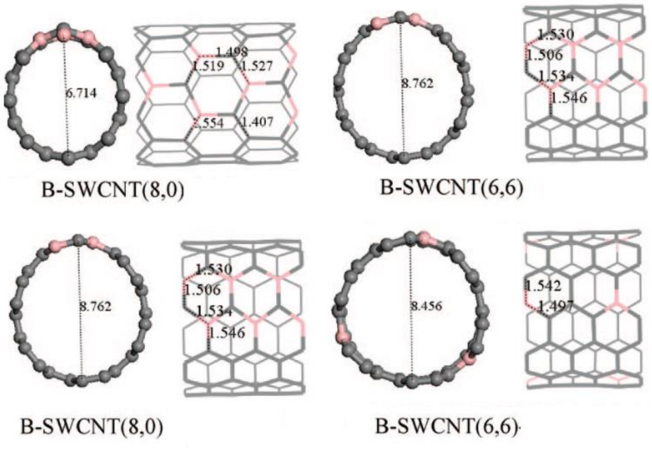

Figure 1.10 Boron doping arrangement and the geometrical structure of B-SWCNT [91].

Theoretical studies predict that if boron replaces some carbon atoms in the graphene sheets of CNTs, the sp^2 hybridisation of the hexagonal network is perturbated and local defects are formed. The substitution of a carbon atom with boron may initiate the formation of the pentagon in graphene sheet of CNTs [92]. The interactions of some pentagons in graphene sheets of CNTs induce the formation of the Stone-Wales defect and vacancies. The chirality, topology, diameter, and defect structure are strongly related to their electronic properties [93].

CNTs doping can be performed via two processes, either by post-synthesis or directly during synthesis. Doping in post synthesis method can be prepared by a solid-state reaction or by gas to the solid reaction. In solid-state reaction, doping diffuses into MWCNTs structure in the high temperature and replaces a hexagonal network of the carbon nanotube. The limitation of a solid-state reaction is inhomogeneous of the doping surface, a higher than 1000°C reaction temperature, and the formation of by-products from unreacted doping precursor. A 15% substation level of a carbon atom by boron can be achieved by solid-state reaction [94].

B-CNTs can be produced by solid-state reaction of CNT with boron oxide in an argon atmosphere at 1100°C. Boron improves the degree of carbonisation of CNTs [95]. MWCNTs are stable up to 3000°C in an argon atmosphere. At 2200°C, the solid-state reaction between boron oxide and the MWCNTs does not affect the nanotexture of the MWCNTs [96]. As compared to boron oxide, boron shows different behaviour in solid-state reaction at high temperature. It was reported that boron induced the transformation of MWCNTs to rod-like graphitic carbon at 1800°C [97].

CVD allows the doping of synthesized CNTs at a lower temperature than solid state reaction. In CVD, it was reported that the variation in the boron concentration in B-MWCNTs leads to MWCNTs with different morphologies [98]. The advantage of direct doping by CVD is that all the CNTs are uniformly doped. Diborane, boric acid, triisopropyl borate, boron trifluoride, and magnesium boride can be used as doping sources for the synthesis of B-doped CNTs [99–103]. Depending on the expected results, the synthesis of B-doped CNTs by CVD can be performed in a wide range of temperatures between 700-1200°C. It was reported that increasing the amount of boric acid in the ferrocene-xylene mixture in CVD deteriorates the crystallinity of CNTs [100].

Phosphorus atoms have one more extra valence electron than carbon atoms. P-CNTs exhibit p-type doping with an extra electron as a current carrier. Due to its larger atomic size compared to carbon, boron, and nitrogen, phosphorus may be more difficult to substitute into a hexagonal carbon lattice network. However, experimentally, it was demonstrated that phosphorus can effectively work as a dopant in CNTs, either as a single substitutional dopant or as a co-dopant with nitrogen [104,105]. Compared to carbon-carbon bonding, phosphorus-carbon bonding may exist in different bonding configurations in CNTs because the length of C-P is longer than C-C. The typical length of bond C-C is about 1.41 A, while the length of C-P bond is about 1.8 and 1.79 A. On the other hand, the phosphorus atoms have 42.9% greater atomic radius than carbon. The presence of phosphorus in carbon nanotubes produces a geometric strain of carbon nanotubes [106]. A suggested model of P-SCWNT structure can be seen in Figure 1.11. The excess of lattice strain by structure deformation creates a local defect and increases the reactivity of the CNTs [107].

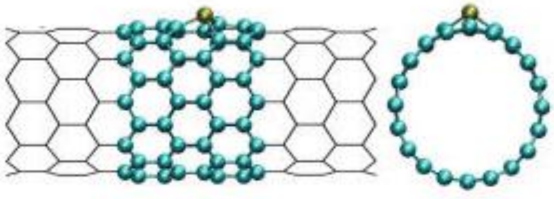

Figure 1.11 The structure of P-SWCNT due to longer P-C bond [106].

Triphenyl phosphine and phosphoric acid are typically used for the synthesis of P-CNTs. It was reported that the presence of phosphorus in MWCNTs decreases the length of the tube as compared to the un-doped tubes grown under the same conditions [104]. In the synthesis P-MWCNTs by decomposition of toluene in the presence of ferrocene catalyst, the increase of triphenyl phosphine concentration decreases the crystallinity of MWCNTs. The incorporation of phosphorus into the graphitic sheets and the formation of iron phosphide contribute to the loss of the crystallinity of CNTs [104]. P-MWCNTs can be produced by Fe/Ni catalyst, deposited on anodic alumina membrane containing phosphorus using methane/hydrogen carbon precursors. P-MWCNTs structure containing a nanoparticle surrounded graphitic shell was reported [108]. Thermal decomposition in a high vacuum CVD can be used for producing P-SWCNTs. With this method, the thermal decomposition of trimethyl phosphiphe, in the presence of an iron based catalyst, takes place at 900°C in a high vacuum condition [109]. Endohedral doping of phosphorus in SWCNTs can be obtained by means of vapor diffusion. SWCNTs and red phosphorus were reacted in a vacuum quartz tube at 440°C for 24 hours [110].

1.1.5. Purification of MWCNTs

Various types of hydrocarbons can be produced as the by-products of CNTs synthesis. The main impurities in CNTs synthesis are graphite, amorphous carbon, metal catalyst, fullerene, and polyaromatic hydrocarbons. The purification of CNTs can be divided into three main purification techniques, namely chemical purification, physical purification, and a combination of chemical and physical purification. Chemical purification can be performed by gas-phase oxidation or liquid phase purification. The limitation of gas oxidation is that the metal nanoparticle cannot be removed, and further acid treatments are needed.

Due to their chemical reactivity, fullerene and polyaromatic hydrocarbon can be eliminated by treatment with an organic solvent. Acid treatment can be used to remove the metal catalyst. Amorphous carbon exhibits higher reactivity than graphite because of the more dangling bond. A high defect density allows the amorphous carbon to be removed by oxidation. A metal catalyst encapsulated by hydrocarbon cannot be dissolved in acid. The purity of CNTs does not only depend on the purification methods but also on the type of CNTs, morphology, structure, impurity size, particle size, curvature and crystallinity of the CNTs [111].

The CNTs purification results in a change of surface area, modification of active surface area, introduction of additional functional group and enhancement of defect density [112]. The most commonly used acids for CNTs purification are HCl, H_2SO_4, and HNO_3 that help selectively eliminate amorphous carbon and iron nanoparticles. However, HNO_3 has mild oxidation ability. The limitation of HNO_3 is not only on oxidized impurities but also on the CNTs. Kinetically, the efficiency of metal nanoparticle dissolution and CNTs oxidation strongly depends on the metal content, oxidation time, CNTs structure and temperature. HCl selectively removes amorphous carbon and metal catalyst. There is no significant effect of HCl on the CNTs structure except for the removal of the amorphous carbon and metal catalyst [113]. The surfactant can be used for nanotube purification. This method allowed nanotubes to flocculate, leaving the nanoparticle in suspension [114].

1.1.6. MWCNTs functionalisation via oxidation and nano particle decoration

Oxidation is a simple method to purify CNTs and introduce oxygenated functional groups on CNTs such as hydroxyl, carbonyl, and carboxyl. The most commonly used oxidants for oxidation of CNTs are HNO_3, and mixtures of HNO_3-H_2SO_4, H_2O_2-H_2SO_4, $KMnO_4$ -H_2SO_4, and H_2O_2-HCl. End-tube functionalisation and defects can be achieved by CNTs oxidation. The yield functionalisation of CNTs with acid oxidation depends on the type of acid, concentration, time, and temperature of reflux. CNTs functional groups generate electrostatic stabilisation and enhance CNTs solubility in water or polar solvent. CNTs functional groups can be used for starting the anchoring of nanotubes for further functionalisation. On the other hand, HNO_3 can be used to open nanotube caps. CNTs, with a high density of oxygen-containing groups, can be produced via oxidation with hot concentrated HNO_3. Concentrated HNO_3 at room temperature demonstrates poor kinetic reaction for groups functionalisation of CNTs.

A binary mixture of H_2O_2-H_2SO_4 (piranha) can be used to modify the CNTs structure under specific conditions. Piranha works effectively at high temperature to attack the existing damage site, generating vacancies in the sidewall, consuming the oxidised vacancies and decreasing the length of CNTs. The reaction between piranha and CNTs at low temperature minimises carbon loss and side wall damage [115]. It is possible to cut a CNT into a small fragment and decorate it with oxygenated functional groups. The combination of fluorination and piranha can be used in order to cut CNTs at a specific location and oxidize the CNTs. The process involves the introduction of sidewall damage by fluorination and the cutting side wall damage by piranha solution. This method allows the production of CNTs in short segments [116].

CNTs with higher defects show a higher activity towards redox system. Because of this, it is reasonable to increase the disorder in the CNTs structure. Liquid phase oxidative functionalisation permits to remove the amorphous carbon and metal impurities, simultaneously decorating the CNTs

Various nanoparticles that exist as a by-product of CNTs, including the carbon nanoparticle, a catalyst, and a graphite or an amorphous carbon can be formed by CVD. Metal or molecule clusters of a nanoparticle can be introduced to enhance the surface properties of CNTs, which is then either noncovalent or covalently bound to the CNT surface. The interaction between a nanoparticle and a CNT does not only exist at the defect's site but also in a perfect hexagonal site. The electronegativity, the size of nanoparticle or cluster and the interaction between the impurity and lattice influence the physical properties of CNTs. CNTs-nano particle hybrid structure could be very sensitive to surrounding molecular species and photon illumination. The nano particle acts as a catalyst and the CNTs as transducer and catalyst support because of the high surface area, stability, and their unique mechanical properties [117].

1.2. Electrochemistry of carbon nanotube

The electrochemical properties of CNTs are greatly dependent on the structure and electronic properties, the interfacial surface structure, and the surface chemistry of CNTs. Those features determine the electrode kinetic and potential limits, background current, and interaction with molecules on electrode interfaces.

CNTs have a more complex π conjugated surface, as compared to graphene. Graphene has a planar aromatic structure with a flat π conjugated surface whereas, in CNTs, π conjugated surface of graphene sheets rolled up into a concentric cylinder. The bending of graphene sheet in a three-dimensional structure of CNTs generates strain in the carbon framework and produces a non-planar π conjugated surface. Curvature-induced sp^2 pyramidalisation of the carbon atom and the misalignment of π conjugated surface are responsible for the CNT's reactivity [118]. The difference in chemical properties between the CNT's sidewall and the CNT's cups is determined by the nanotube curvature. The cup of CNTs resembles the half of a fullerene structure. Due to the higher curvature, the cups of CNTs contain more reactive carbon atoms than the side wall [119]. The pyramidalisation angles (Θ_p) are charaterised by the angle between the π orbital and σ bonds, minus 90°[118]. (Θ_p) describes the reactivity of carbon allotropes. For comparison, graphene has (Θ_p) which equals 0° whereas C_{60} has 11.6° [120]. Theoretical calculation of SWCNT(n,n) pyramidalisation angles for n=3 to n=10, (Θp) vary between 11° and 2° [118].

In the open cups of CNTs structure, the tip of CNTs structure is attributed to the edges plane of the HOPG, and the tube walls are linked to the basal plane of the HOPG. Experimentally, it was reported in HOPG that the basal plane exhibits a slower electron transport kinetic than the edge plane. For instances in $[Fe(CN)_6]^{3-/4-}$ redox system, the heterogeneous electron transfer rate constant of basal plane HOPG is smaller than 10^{-6} cm/s whereas the edge plane HOPG is around 0.06-0.10 cm/s [121].

1.2.1. Density of states and charge transfer of CNTs

CNTs have a varied density of state (DOS) which depend on chirality and tube diameter [122,123]. DOS is related to the number of states per interval energy at each energy level that is available to be occupied. DOS can be calculated from the band structure according to the following equation:

$$DOS = \frac{dN}{dE} = \frac{dN}{dk}\frac{dk}{dE} \tag{1.1}$$

Where N is the number of states, E the energy and k a wave vector.

In an electrochemical reaction, the electrochemical potential is equivalent to the Fermi level in the DOS of a redox system:

$$\mu_{e,redox} = E_{f,redox} \tag{1.2}$$

The DOS distribution of CNTs is strongly dependent on carbon structure. The change of DOS, due to the presence of structural defect, is related to the change of electrochemical potential and bond reactivity. Thermodynamically, the electrochemical potential in simple redox reaction is given by:

$$\mu_{e,redox} = \mu^{o}_{e,redox} + kT \ln \frac{C_{ox}}{C_{red}} \tag{1.3}$$

Where $\mu_{e,redox}$, C_{ox} and C_{red} are the electrochemical potential of electron in the redox system, and the concentration of oxidation and reduction species in the solution, respectively.

Theoretical studies of P-SWCNT by the first principle based density functional theory show that the difference of concentrations and positions of phosphorus impurity in CNTs exhibits different effects on the electronic structure of CNTs [124]. Both electronic transport and DOS of B-SWCNT are affected by the distribution of boron doping in SWCNT structure [125].

The kinetics of electrochemical reaction in CNTs electrodes is strongly affected by the density of state of CNTs and solution. A suggested model of heterogeneous electron transfer by Gerischer-Marcus was used to explain the heterogeneous electron transfer kinetics in CNTs and electrolyte [126]. The Gerischer-Marcus model assumes non-adiabatic electron transfer across the electrode/electrolyte interface. In this model, electron transfer is considered to be based on the overlap between the electronic states of the electrode and those of the reactants in the solution. The main approach is that, in order to be in equilibrium, the electrochemical potential of the solution and the Fermi level of the electrode must be the same. The energies and numbers of available electrons (donors) and holes (acceptors) in the electrode are also considered in heterogeneous electron transport by this model. Figure 1.12 illustrates the electron transfer from the solution to an empty state of SWCNT to achieve an equilibrium if the Fermi level in the solution is higher than that of the electrode [127].

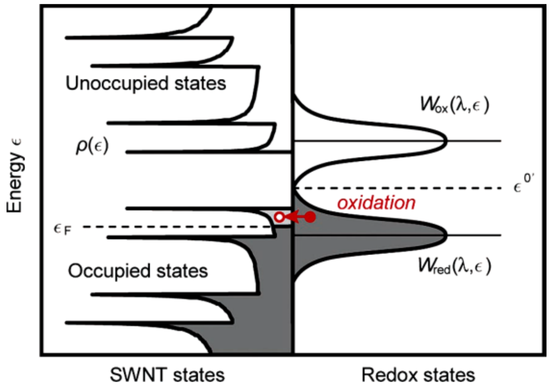

Figure 1.12 The Gerischer-Marcus model of electron transfer in SWCNT and solution [127].

In the Gerischer-Marcus model, the heterogeneous rate constant for reduction and oxidation is given by the following relations:

$$k_f = \vartheta \int_{-\sim}^{\sim} \varepsilon_{red}(E) W_0(\lambda, E) f(E) \rho(E) dE \tag{1.4}$$

$$k_f = \vartheta \int_{-\sim}^{\sim} \varepsilon_{ox}(E) W_r(\lambda, E)(1 - f(E)) \rho(E) dE \tag{1.5}$$

Where $\varepsilon_{red}(E)$ and $\varepsilon_{ox}(E)$ are proportionality factors, $\mathrm{W}(\lambda, E)$ probability density function, $f(E)$ probability that a state of energy exists, and $\rho(E)$ the density of state.

Since MWCNTs consist of multiple SWCNT structures and nanotubes, and DOS is highly sensitive about the diameter and chirality, different values can be observed in a heterogeneous electron transfer.

1.2.2. Defects site, CNTs reactivity, and sensitivity

It is almost impossible to produce defect-free CNTs. Various inherent defects can be formed during a CNTs synthesis, which includes local impurities from an encapsulated catalyst inside the CNT's structure, sidewall defects, such as the Stone-Wales defect, vacancies, and sp^3 re-hybridisation. Defects play an important role in the electrochemical properties of CNTs. For instance, sidewall defects reduce the conductivity of the CNTs because of back resonant scattering, the presence of sp^3 and many functional groups increases the resistivity of CNTs, and the presence of basal plane defects increase the chemical reactivity of the CNTs.

The sensitivity of MWCNTs is related to their conductivity. Since MWCNTs consist of several graphene sheets, the conductivity of MWCNTs involves inter shell and intra shell resistivity of each rolled graphene sheet [128].

The increase of defect density changes the DOS and chemical potential of CNTs electrodes. One dimensional defect in CNTs is commonly observed at the end of the tube. At the end tube structure of CNTs, varied bond orderings and bonding configurations can occur. End tube structure of CNTs can be half fullerene cups and open cups. Various edge defect configurations can occur in the graphene structure in open cups, as it can be seen in Figure 1.13 [30]. Configuration with the fewest dangling bond is the most unreactive one.

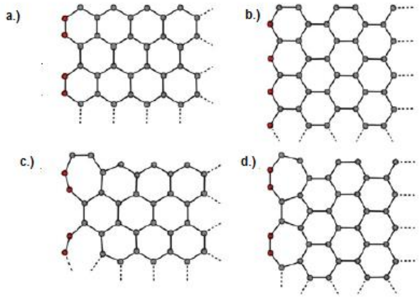

Figure 1.13 Various edge plane configuration defects [30].

The dangling bond at the end of the tube can be modified with various atoms or compounded to obtain a new local bond geometry, in which various new edge plane configurations can occur [30]. Sidewall defects work as an active site for redox sensing since such defects are more chemically reactive compared to pristine sites. Vacancies in the sidewall are sensitive for molecular adsorption. The presence of adsorbates contributes significantly to the electrochemical activity of CNTs. An adsorbate facilitates the electron transfer between the core of a redox reaction and the CNT based electrode and allows the detection of electrochemical reaction on the electrode surface. Depending on its type, the presence of adsorbate on an electrode surface can enhance the electrocatalytic activity of the electrode or block the active site of the chemical reaction.

The partially blocked electrode dramatically changes the electrode performances. The electrode performance in the partially blocked electrode is strongly influenced by unit block geometry and by the size distribution of the blocking unit [121,129]. The decrease of peak current is one of the indications of a partially blocked electrode [121]. Theoretical simulation shows that the distribution nanoparticle in a heterogeneous surface influences the voltammetry signal, as can be seen in Figure 1.14.

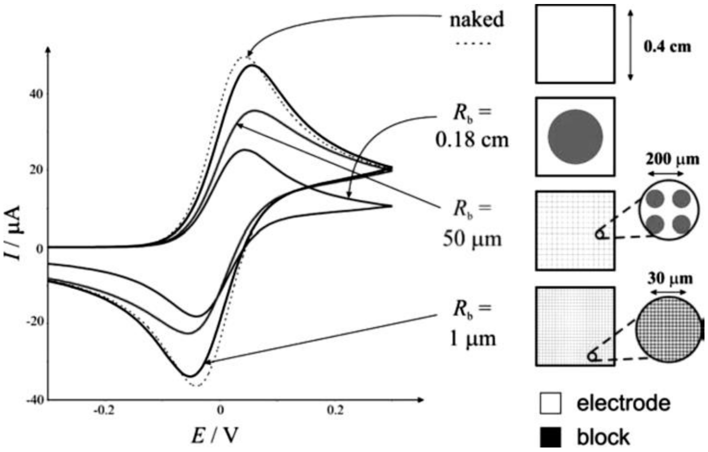

Figure 1.14 Voltammetry signal in various distributions of a nanoparticle in a partially blocked electrode [121].

1.2.3. The role of nanoparticle in CNTs reaction kinetics

In electroanalysis, nanoparticles play a specific role in each electrochemical reaction. Various kinds of nanoparticles such as metal and ceramic nanoparticles have been used in electrochemical sensors. Nanoparticles have several basic functions in a carbon modified electrode, including the immobilization of biomolecules, electrocatalyst, and increase in the electron transport between the electrode surface and reactant [130].

The integration of the CNTs and nanoparticles may lead to the combination of the different properties of the different material into a new feature of the hybrid material [131]. In nanoparticle modified CNTs, CNTs act as an active surface where nanoparticles are adsorbed. Nanoparticles can be adsorbed naked on the CNTs surface by a weak intermolecular interaction force or linked by covalent bonding. The presence of the nanoparticle on the CNTs surface modifies the microenvironment on the outer graphene sheet of the CNTs. The catalytic activity of the nanoparticle modified CNTs is attributed to the distribution of the nanoparticle on the CNTs electrode surface [121].

A nanoparticle exhibits different Butler-Volmer kinetics, compared to CNTs. The introduction of the nanoparticle can enhance the electro catalytic activity of some specific electrochemical reaction or decrease the electrochemical activity due to the formation of the partially blocked electrode or its surface area reduction. A nanoparticle modified CNT may be considered as a heterogeneous electrode. It is comprised of two or more types of spatial zones with different Butler Volmer type electrode kinetics (Figure 1.15) [121].

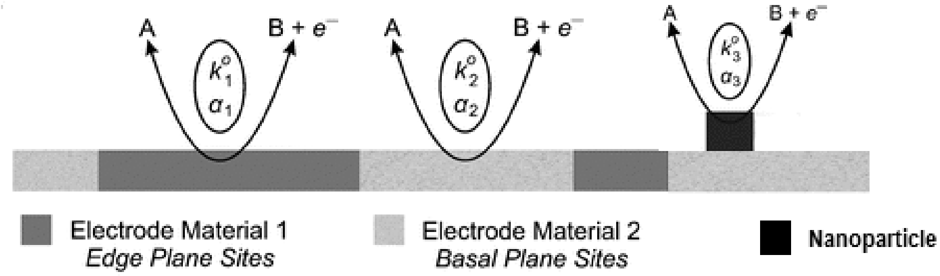

Figure 1.15 Heterogeneous electrode with different Butler-Volmer kinetics [121].

The presence of the nanoparticle on the CNT's surface leads to a convergent diffusion rather than a linear diffusion. A higher rate mass transport is allowed. Due to the increased mass transfer over potential, the signal of voltammetry can be modified. The Electrocatalytic activity of the nanoparticle leads to decrease of the reaction overpotential, leading thus to a faster kinetic of the electrochemical reaction [132].

Due to their strong sp^2 bonding and since they possess a stable hexagonal network structure, CNTs have poor chemical reactivity, thus hindering the formation of a covalent bond with most molecules. CNTs functionalisation with gold nanoparticle enhances their chemical reactivity toward specific biomolecules. Gold nanoparticle can be used to facilitate chemisorption of various functional groups through thiol mediation. Biomolecule can be attached on a nanoparticle surface. Gold possesses high oxidation potential and high conductivity. Hence, gold nanoparticle can be used to enhance the electron transfer between a biomolecule and the CNTs electrode in a certain system. It was reported that the modification of CNTs with gold nanoparticle leads to diminishing of overpotentials, increase of the peak current, and enhancement of the sensitivity and selectivity [132].

1.3. Electrochemistry of dopamine

Dopamine or 3,4-dihydroxy phenethylamine is a catecholamine neurotransmitter that plays several important roles in the human body (Figure 1.16). In the central nervous system, the primary function of dopamine is a local chemical messenger that is released by neurons to send signals to another nerve cell. Dopamine is commonly used to treat low blood pressure and a slow heart rate, which may be caused by heart attack, surgery, heart failure, trauma, and other serious medical conditions. The hemodynamic effects of a dopamine injection on the human body are dose-dependent. A low-dose of dopamine (0.5 to 3 μg/kg/min), leads to the activation of dopamine-specific receptors in the renal system, increasing the urine output and renal blood flow. An intermediate dose of dopamine (3 to 7.5 ug/kg/min), results in stimulated b-receptors in the heart, thereby increasing the cardiac output, heart rate, and cardiac contractility. A high-dose of dopamine (>7.5 ug/kg/min), can stimulate the α receptor and may increase the risk of tachyarrhythmia. The dopamine reference range in human plasma in the age range of 3-15 years is <60 pg/mL [133].

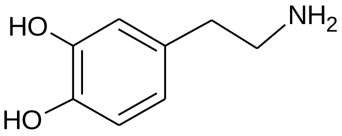

Figure 1.16 Dopamine structure.

Dopamine can be detected with electroanalytical methods, since its oxidation potential of dopamine, (+0.2 V Vs Ag/AgCl) lies within the potential limits for carbon nanotubes [134]. Dopamine oxidation to dopamine o-quinone in CNTs involves a two-electron transfer mechanism. A dopamine quinone molecule can undergo an intermolecular addition, which results in a cyclization reaction, generating leucodopaminechrome. Leucodopaminechrome can be further oxidized via another two electrons transfer to dopaminochrome. However, it was reported that the dopaminochrome can be further oxidised to indolic-o-quinone to generate the film insoluble melanin polymer, which fouls and poisons the electrode [135].

It was reported that the dopamine oxidation to dopamine o-quinone on CNTs is reversible in cyclic voltammetry [136]. The heterogeneous electron transfer between the electrode and the catecholamine is strongly affected by adsorption of the catecholamine on the electrode surface [137]. The π electron in the benzene ring of dopamine interacts with the π electron in the hexagonal network of CNTs, making the electron transfer feasible [138]. Hydroxyl and amine groups of dopamine interact with MWCNTs-COOH via hydrogen bonding.

Chapter 2

Experimental Section.

2.1. Synthesis of B-MWCNTs and P-MWCNTs

CVD is a chemical process that widely used to produce large-area, high-quality, and uniform MWCNTs film with controllable thickness. The CVD based synthesis of a carbon nanotube is a thermal dehydrogenation reaction, whereby a catalyst is used to decrease the reaction temperature to decompose a gaseous hydrocarbon into carbon, hydrogen, and other molecules. The B-MWCNTs and P-MWCNTs were synthesized by means of chemical vapor deposition technique onto oxidized porous silicon wafer using ferrocene as a catalyst. The scheme of the CVD apparatus and experimental details concerning the pyrolysis technique are shown in Figure 2.1 [139].

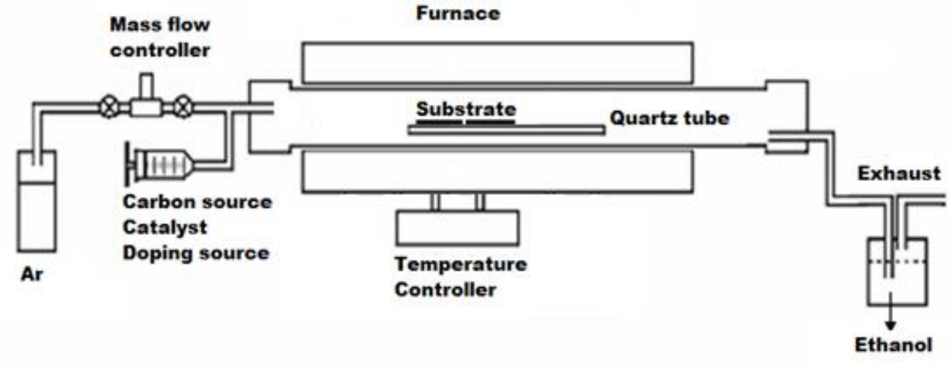

Figure 2.1 A schematic representation of direct liquid injection catalytic chemical vapor deposition

2.1.1. Ethanol based catalytic chemical vapor deposition for the production of MWCNTs

The synthesis of pristine MWCNTs was performed in a quartz tube (25 mm in diameter and 1 m long) placed inside an electric tube furnace. The Si/SiO_2 wafers with a geometrical area of 1.0 cm^2 were arranged in the middle of the quartz tube. The furnace temperature was setup to 850°C in argon gas atmosphere. A solution of ferrocene (1.0 wt %) in ethyl alcohol was introduced into the reactor through a syringe with a flow rate of 0.17 mL min^{-1}. The reaction time was fixed at about 30 min, and thus, a total volume of 5 mL of ethyl alcohol/ferrocene binary mixture was introduced into the reactor for the synthesis of the

MWCNTs. The furnace was cooled down to room temperature for 90 minutes in an argon atmosphere. The MWCNTs films on silicon/silicon oxide wafers were collected from the quartz tube.

2.1.2. Ethanol based catalytic chemical vapor deposition for the production of B-MWCNTs

The synthesis of B-MWCNTs onto Si/SiO_2 substrate (1 cm^2) was performed by alcohol catalytical chemical vapor deposition. Ethanol was used as a carbon source, and ferrocene was used as a catalyst. In order to study the effects of doping sources material on the nanotubes growth process, two different boron sources materials namely boric acid and triethyl borate (TEB) were used as the doping sources. For B-doped MWCNTs synthesis, boric acid (1.0wt %) dissolved in absolute ethyl alcohol containing ferrocene (1.0wt %) as well as triethyl borate dissolved in absolute ethyl alcohol containing ferrocene (1.0wt %) were used.

The B-MWCNTs synthesis was carried out at 850°C in an argon atmosphere. For the growth process, 5.0 ml of ternary mixtures were sprayed into a furnace at a temperature of 850°C through a syringe with controlled flow rate (0.17 mL min^{-1}). The synthesis duration time was kept constant for 30 minutes. The cooling time was set up for 90 minutes in an argon atmosphere.

The fabricated B-MWCNTs films were treated with hydrochloric acid (15wt %) for about 2 min, washed with distilled water, and dried at room temperature to remove the boron oxide and the residues of iron catalyst nanoparticles from carbon nanotubes. In order to introduce some hydroxyl and carbonyl functional group in B-MWCNTs, the unpurified B-MWCNTs films were treated with a mixture of concentrated sulfuric acid and 30% hydrogen peroxide solution at a ratio of 3:1 (piranha solution) for about 2 minutes, washed with distilled water and dried at room temperature.

The photochemical segmented flow technique was used to produce a 12.5 nm colloidal gold nanoparticle [140,141]. The B-MWCNTs/AuNPs films were produced according to following procedure: The B-MWCNTs films were immersed in sodium citrate aqueous solution (2.5

mM) for 10 minutes. Thereafter, the treated B-MWCNTs films were dried for 10 minutes at room temperature. The AuNPs colloidal solution was dropped onto the treated B-MWCNTs films using a micro-pipette. The B-MWCNTs/AuNPs films were dried at room temperature for 24 hours and then washed with distilled water.

2.1.3. Propanone based catalytic chemical vapor deposition for the production of B-MWCNTs

In order to produce the B-MCWNTs, a boron doping mixture of triethyl borate, propanone and ferrocene were used as boron doping material, carbon material, and catalyst, respectively. The synthesis was carried out by means of chemical vapor deposition technique. In order to study, the effects of doping sources concentration on the nanotubes growth process. The composition of triethyl borate was varied in the range of 0.5-3.0 wt %. The mass of ferrocene was fixed at 2.0wt %. The ternary mixture of solution was introduced into the quartz tube at 850°C via a syringe with a flow rate of 0.17 mL/min. After 17 minutes, the sprayed process was stopped, the substrate was cooled down up to room temperature in an argon atmosphere within 90 minutes and the produced samples were collected from the quartz tube.

2.1.4. Ethanol based catalytic chemical vapor deposition for the production of P-MWCNTs

P-MWCNTs were produced by means of catalytic chemicals vapor deposition onto silicon/silicon oxide substrate. Ethanol was used as a carbon source, ferrocene as a catalyst and triphenyl phosphine (TPP) as a phosphorus source for the doping material. The fabrication of the P-doped MWCNTs was performed in a horizontal quartz tube (25 mm in diameter and 1 m long) reactor placed inside an electric horizontal tube furnace. The concentration of TPP and ferrocene was fixed at 1 wt %. A ternary mixture of the spray solution was introduced into the furnace at the temperature of 850°C through a syringe with a flow rate of 0.17 mL/min. The growth processing time was kept constant at 30 min, and a total 5 ml volume of ternary compounds was sprayed into the furnace for the P-doped MWCNTs production. To eliminate the residual iron catalyst and other reaction by-products, the P-MWCNTs films were treated with hydrochloric acid (15 wt %) for about 2 min, washed with distilled water, and dried at room temperature. The hydroxyl and carbonyl functional group were introduced to P-MWCNTs via treatment with the mixture of concentrated sulfuric acid and 30% hydrogen peroxide solution at a ratio of 3:1 for about 2 minutes.

In order to study the effect of gold nanoparticles modification on P-MWCNTs on the electrochemical properties of P-MWCNTs, colloidal gold nanoparticles (AuNPs) possessing a diameter of 12.5 nm were synthesized using a photochemical segmented flow technique [140,141]. The P-MWCNTs/AuNPs films were prepared according to the following procedure: The P-MWCNTs films were dipped in sodium citrate aqueous solution (2.5 mM) for 10 minutes. The treated P-MWCNTs films were dried for 10 minutes at room temperature. The AuNPs colloidal solution was dropped onto the treated P-MWCNTs films using a micro-pipette and dried at room temperature for 24 hours. The P-MWCNTs/AuNPs films were then washed by with distilled water and dried in the air for ~24 h.

2.1.5. Cyclohexane based catalytic chemical vapor deposition for the production of P-MWCNTs

The synthesis of P-MWCNTs onto silicon/silicon oxide wafer was performed by means of catalytic chemical vapor deposition via thermal pyrolysis of cyclohexane in the presence of triphenyl phosphine (phosphorus source material) and ferrocene catalyst. The composition ratio of triphenyl phosphine/ferrocene was varied in order to investigate the effect of composition on the structure and electrochemical properties of MWCNTs. The composition of triphenyl phosphine and ferrocene ternary mixture were varied in the range of 0.5-2.0 wt %. The mass percent of ferrocene was fixed at 2.0 wt %. The ternary mixture solution was sprayed into a furnace at 900°C through a syringe with flow rate 0.17 mL/min; the growth reaction time was kept constant at 17 min, and a total 3 ml volume of a ternary compound was sprayed into the furnace for the production of P-MWCNTs. The furnace was cooled up to room temperature in an argon atmosphere within 90 minutes and, afterward, the MWCNTs films on silicon/silicon oxide wafers were collected from the quartz tube.

2.2. Characterisation

2.2.1. Scanning electron microscopy

Scanning electron microscopy (SEM) is an important tool to evaluate the characteristics of CNTs [142]. SEM imaging was used to visualise the overall morphology and topography of MWCNTs, and to quantify the degree of purity of the MWCNTs, as well as the dimensions of the tubule. SEM provides comprehensive information about the type of MWCNTs, the width/diameter, the nanotube geometry, and the characteristic of impurity. The morphology of the various unmodified and modified MWCNTs were characterized using a scanning electron microscopy (a Zeiss ultra scanning electron microscope equipped with Oxford instruments EDX detector).

2.2.2. Transmission electron microscopy

Transmission Electron Microscopy (TEM) is an image acquisition technique, in which a beam of high-energy electrons (80-400 keV) is focused by electromagnetic lenses onto a thin specimen causing an enlarged image on a fluorescent screen or a CCD camera. Contrary to light microscopy, the TEM works based on the electrons diffraction and not by absorption, whereas the intensity of the electron beam is influenced by the density and thickness of the sample. TEM has greater resolution than SEM and thus TEM was used to visualise the number of walls of the nanotube, defects, tube orientation, impurities, the size of carbon impurities and the nanoparticle [142]. The morphology of various produced MWCNTs were examined using a transmission electron microscopy (FEI Titan operating at 300 kV, images acquired using TEM and elemental analysis acquired using STEM).

2.2.3. Raman spectroscopy

Raman spectroscopy was used to obtain information about the defect and to distinguish the presence of MWCNTs relative to other carbon allotropes. Since MWCNTs are comprised of multiple SWCNTs the Raman scattering of MWCNTs is an ensemble of various nanotube diameters ranging from small to very large [143].

The monochromatic light interacts with a molecule in some fashion; it can be reflected, absorbed or scattered in some manner. When monochromatic radiation is incident upon a molecule, the light scattering occurs in all directions and may change its polarisation along with its wavelength. The scattering process can be the Rayleigh scatter and the Stokes and the anti-Stokes Raman scatter. The elastic scattering without a change of frequency is called Rayleigh scattering whereas inelastic scattering from a change in the frequency of the light is called Raman scattering. Depending upon the vibrational state of the molecule and structure of the molecule, Raman shifted photons of light can be of either higher or lower frequency. The inelastic scattering frequency is used to construct a Raman spectrum. By measuring the light scattering intensity as a function of the light scattering frequency, the downshift information about the geometrical structure of a material can be obtained.

The G band, D band, and G' band represent the characteristics of a sp^2 carbon bond. The G band (around 1600 cm^{-1}) is attributed to the tangential vibration of graphitic carbon in graphite. The G band comes from the atom displacements along the CNT axis analogous to the in-plane atom displacement of graphene. The D band (around 1300-1400 cm^{-1}) corresponds to the presence of amorphous carbon and resonance effects in sp^2 carbon. The D band is related to bond vibrations that are produced in the radial stretching/contracting of the hexagonal structure of CNTs. Its peak is a parameter of the degree of disorder in CNTs [144]. The D band intensity increases with the increase of a number of defects (pentagon-heptagon, vacancy, impurities). The G' band (around 2700 cm^{-1}) is caused by phonon scattering around the K point of the Brillion zone. The G' band is very sensitive to defect density. The ratio of the D band and the G band peak or the G' band and D band peak can be used to assess the defect of MWCNTs [145]. The influence of defect on bond vibration can be observed by monitoring the peak position, width, height and the intensity of the Raman spectra.

Raman spectra of various B-MWCNTs and P-MWCNTs films were studied using a microprobe spectrometer (Renishow, Gloucestershire, UK) coupled with a Leica confocal microscope. Laser excitation light of the length of 488 nm (2.54 eV) and power of about 20 mW were used. The laser spot diameter was about 1 μm. The main Raman feature of sp^2-carbon materials was fitted by using Lorentzian curves.

2.2.4. X-ray photoelectron spectroscopy

X-ray photoelectron spectroscopy (XPS) was used to understand the binding state of the heteroatoms on the carbon surface. XPS gives some information about the electronic structure, the composition of a sample and detailed information about the chemical bonding environment of an atom.

In XPS, the sample was irradiated by monochromatic X-ray. When the sample is struck by x-ray radiation, electrons with specific kinetic energy are ejected from the sample and detected in a hemispherical electron analyser. The yielding spectrum contains a series of photoelectron peaks of each specific core energy level of the different sample atoms. The binding energy (E_B) can be directly calculated from the kinetic energy of the photoelectrons by this following equation:

$$E_B = \hbar\omega - E_{kinetics} - E_{\Phi} \tag{2.1}$$

where E_{Φ} is a work function. Photoelectron peaks in each energy level correspond to the nature of chemical bonding of atoms. The XPS was used to charaterise this chemical bonding.

In this research work, the chemical composition and boron in MWCNTs structure were charaterised by X-ray photoelectron spectroscopy (XPS) measurements in normal emission using an ultra-high vacuum (UHV) system equipped with a Physical Electronics 10-610 X-ray source in combination with an Omicron XM1000 monochromator for the generation of Al Kα radiation (1486.7 eV). A 7 channel lEA125 hemispherical electron analyser was used as a detector. The detailed experimental condition has been already reported in the previously published article [146].

2.2.5. Cyclic voltammetry

Cyclic voltammetry was used to study the influence of the synthesis conditions of the B-MWCNTs and P-MWCNTs on electrode kinetics and the sensitivity toward studied redox system. During cyclic voltammetry, the electrode potential is applied linearly versus time in a triangular cyclical waveform at a constant scan rate.

A three-electrodes system was used to investigate the electrochemical properties of B-MWCNTs and P-MWCNTs. The system consisted of B-MWCNTs or P-MWCNTs working electrode, platinum plate counter electrode, and Ag/AgCl (saturated KCl) reference electrode. The electrochemical properties of the B-MWCNT and P-MWCNT films were determined by means of a cyclic voltammetry technique using the standard redox system $[Fe(CN)_6]^{3-/4-}$ in an aqueous KCl solution (1.0 M). For electrode sensitivity and kinetics characterisation, $[Fe(CN)_6]^{3-/4}$ in the concentration range of 0.1-1 mM was measured. The solution was prepared directly in an electrochemical cell with progressive addition of appropriate volume of stock solution in a 1.0 M KCl aqueous solution.

It is well known that the kinetics of redox system on CNTs can be significantly influenced by their surface properties such as functional groups or defects. The heterogeneous electron transfer rate constant is determined by cyclic voltammetry and impedance spectroscopy by using the $[Fe(CN)_6]^{3-/4-}$ standard redox system. The main reason of $[Fe(CN)_6]^{3-/4-}$ being used as the standard system is because this redox couple undergoes one electron transfer process, exhibits reversible behaviour, and is sensitive to an electrode surface. The reversible reaction of $[Fe(CN)_6]^{3-/4-}$ can be shown with the following equation:

$$[Fe(CN)_6]^{3-} + e \rightleftharpoons [Fe(CN)_6]^{4-}$$

The heterogeneous electron transfer rate constant at macro electrodes is generally calculated by the Nicholson equation [147] based on the peak separation between oxidation and reduction peak in a voltammogram of cyclic voltammetry.

The heterogeneous electron transfer rate constant k_s was estimated by the Nicholson equation [147] using the expression:

$$\psi = \frac{\gamma \, k_s}{(a\pi D_o)^{\frac{1}{2}}} \qquad (2.2)$$

Where,

$$a = \frac{nFv}{RT} \tag{2.3}$$

$$\gamma = (\frac{D_o}{D_r})^{1/2} \tag{2.4}$$

$$\psi = \frac{\gamma\, k_s}{(\frac{nFv}{RT}\pi D_o)^{1/2}} \tag{2.5}$$

$$k_s = \frac{\psi(\pi D_o \frac{nFv}{RT})^{1/2}}{(\frac{D_o}{D_r})^{1/2}} \tag{2.6}$$

In the equation proposed by the Nicholson, ψ is a kinetic parameter, that is calculated as a function of the anodic and cathodic peak separation (ΔEp), D_0 and D_r the diffusion coefficient of the electroactive species; n the number of electrons transferred, F the Faradays Constant, v the potential scan rate, R the gas constant, and T the temperature.

The Randles-Sevcik equation was used to determine the slope of linear variation of anodic and cathodic peak current with concentration and thus to estimates the sensitivity and the limit detection of B-MWCNTs and P-MWCNTs. The Randles-Sevcik equation is expressed by:

$$i_p = 268600\, n^{3/2} A\, {D_O}^{1/2} v^{1/2} C \tag{2.7}$$

Where I_p is the oxidation peak current, A the electroactive area, D_O the number of electrons transferred, v the potential scan rate and C the concentration of the redox species in bulk solution.

2.2.6. Impedance spectroscopy

Electrochemical impedance spectroscopy (EIS) is an electrochemical technique that measures the variation impedance of an electrochemical system as a function of frequency. Impedance is a representation of the electrochemical process on surface in an electrode. Impedance is a ratio between the AC voltage and the AC current signal that shows the ability of a circuit to resist the flow of electrical current and is represented by an impedance complex number. EIS measures the current response to small amplitude AC voltage perturbation by varying its frequency. An expression analogous to Ohm's law is used to determine the electrochemical impedance, as follows:

$$Z = \frac{V(t)}{I(t)} = \frac{V_o \cos(\omega t)}{I_O \cos(\omega t - \phi)} = Z_o \frac{\cos(\omega t)}{\cos(\omega t - \phi)} \tag{2.8}$$

$$Z = \frac{V(t)}{I(t)} = Z_o e^{j\phi} = Z_o(cos\phi + jsin\phi) \tag{2.9}$$

Where Z is impedance, t the time, ω the radial frequency (radian/s), and ϕ the phase shift.

The impedance complex system can be expressed as a combination of real impedance and imaginary impedance using the expression:

$$Z = Z_{real} + jZ_{imaginer} \tag{2.10}$$

The real and imaginary impedance describes the Ohmic and capacitive nature of the electrochemical system respectively. The phase angle is defined as follows:

$$\phi = tan^{-1}\left(\frac{-Z_{imaginer}}{Z_{real}}\right) \tag{2.11}$$

EIS was used to charaterise the electrochemical properties of the CNTs electrolyte interface. To give a snapshot of the various kinetics processes in CNTs, an equivalent electrical circuit is used as a macro model to represent the electrode process in the electrochemical system. EIS identifies the mechanism of the electrochemical process of CNTs electrode by monitoring the phase and impedance characteristics of the system simultaneously over a wide range of frequency. A Randles equivalent electrical circuit with Warburg impedance was used to describe polarisation controlled by combination kinetic and diffusion process in electrode electrolyte interface (Figure (2.2)) [148].

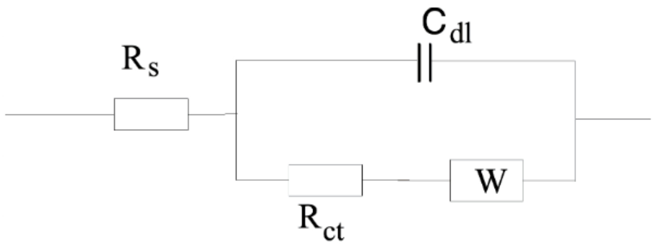

Figure 2.2 Randles circuit with Warburg Impedance, Mixed Kinetic and Charge-Transfer Control equivalent circuit

The equivalent circuit in Figure (2.2) can be modeled by:

$$\mathrm{Z} = \mathrm{R_s} + \frac{1}{\frac{1}{(\mathrm{R_{ct}} + \mathrm{W})} + \frac{1}{\left(\frac{1}{\mathrm{j\omega C_{dl}}}\right)}} \tag{2.12}$$

$$\mathrm{Z} = \mathrm{R_s} + \frac{1}{\frac{1}{(\mathrm{R_{ct}} + \mathrm{W})} + \mathrm{j\omega C_{dl}}} \tag{2.13}$$

Double layer impedance is defined by:

$$\mathrm{Z_{dl}} = \frac{1}{\mathrm{j\omega C_{dl}}} \tag{2.14}$$

Warburg impedance representing the diffusion process can be defined as:

$$\mathrm{W} = \frac{\sigma}{\sqrt{\omega}}(1 - \mathrm{j}) \tag{2.15}$$

$$\boldsymbol{\sigma = \frac{RT}{n^2F^2A\sqrt{2}}\left(\frac{1}{C_o\sqrt{D_o}} + \frac{1}{C_r\sqrt{D_o}}\right)} \tag{2.16}$$

The equivalent circuit in Figure (1.15) can be defined analytically in real impedance (Z_{real}) and imaginary impedance (Z_{imaginer}) using this following equation:

$$Z_{imaginer} = \frac{\boldsymbol{\omega C_{dl}}(R_{ct} + \boldsymbol{\frac{\sigma}{\sqrt{\omega}}})^2 + \boldsymbol{\frac{\sigma}{\sqrt{\omega}}}\ (\boldsymbol{C_{dl}\sigma\sqrt{\omega} + 1})}{(\boldsymbol{C_{dl}\sigma\sqrt{\omega} + 1})^2 + \boldsymbol{\omega^2 C_{dl}}^2(R_{ct} + \boldsymbol{\frac{\sigma}{\sqrt{\omega}}})^2} \tag{2.17}$$

The charge transfer resistance is connected directly to the electrode kinetics reaction by Butler-Volmer, through this following equation:

$$\boldsymbol{R_{ct} = \frac{RT}{n^2F^2AK_sC}} \tag{2.18}$$

Chapter 3
Results and discussion

3.1. Raman spectroscopy of B-MWCNTs and P-MWCNTs

To understand the relationship between the structure and defects of MWCNTs induced by phosphorus and boron doping, Raman spectroscopy was used to characterise the MWCNTs films. The Raman intensity ratio of D-bands and G-bands (I_D/I_G) was used to quantitatively describe the MWCNTs defects. The D-band at around 1300 cm^{-1} in the first-order Raman spectra of carbon nanotubes is induced by the first-order scattering process that involves a substitutional atom, vacancies, grain boundaries or other defects which lower the crystallinity symmetry of the quasi-infinite lattice [149].

Defects concentration quantification, based on (I_D/I_G) ratio, relies on the assumption that the G band intensity is independent of defect concentration and interference-free with any other defects [150]. The G-band, at around 1600 cm^{-1}, corresponds to the tangential mode vibration of the sp^2 carbon atoms in the planar graphene sheets. The G-band-FWHM is strongly affected by d_{002} interlayer graphitic structure [151].

The small intensity of D-peak, compared to G-peak, indicates a higher degree of C-C sp^2 order. The high D peak intensity, compared to the G peak, indicates a lower degree of C-C sp^2 order. The increase of I_D/I_G ratio indicates the increasing level of disorder in nanotube structure and the decreasing crystallinity level of the carbon structure [152].

Molecular vibration properties of MWCNTs can be modified by the introduction of some dopants to their structure. The obtained Raman spectra is strongly dependent on the type of doping material [153]. The Raman spectra comparison of B-MWCNT from boric acid, B-MWCNTs from triethyl borate and P-MWCNTs from triphenyl phosphine are shown in Figure 3.1 and Table 3.1.

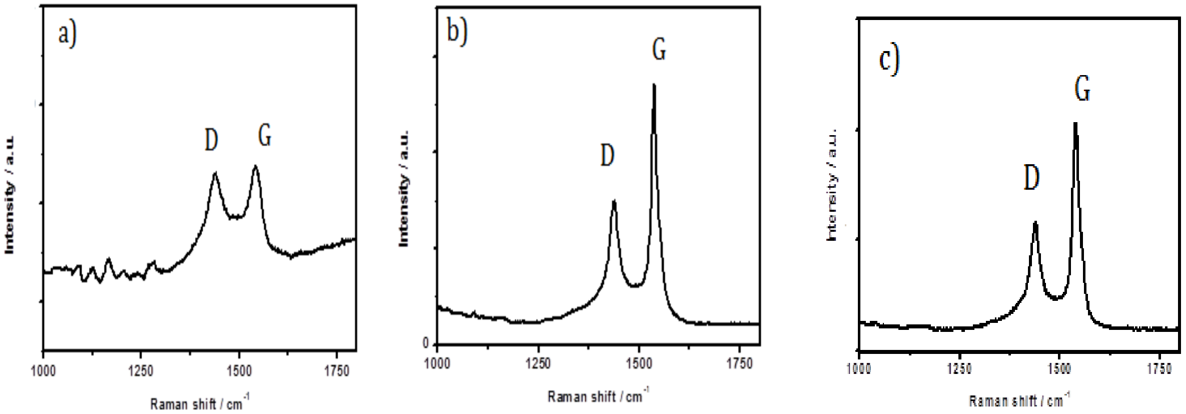

Figure 3. 1 The comparison of Raman spectra of a).B-MWCNTs (Boric acid), b).B-MWCNTs (Triethyl borate), c).P-MWCNT (Triphenyl phosphine)

The comparison of I_D/I_G ratios of B-MWCNTs (boric acid), B-MWCNTs (triethyl borate) and P-MWCNTs (triphenyl phosphine) displayed in Table 3.1 exhibit that the defect density of MWCNTs is strongly influenced by the type of doping precursors. B-MWCNTs from boric acid shows the highest defect density. Boric acid shows stronger influence on the increasing defects density than triphenyl phosphine. Comparison of I_D/I_G ratio confirms that the disorder level and crystallinity of nanotubes can be modified with different doping precursors.

Table 3.1 The intensity ratio of D and G bands (I_D/I_G) for B-MWCNTs and P-MWCNTs from different doping precursors

Material	Carbon precursor	Catalyst	Doping precursor	I_D/I_G
B-MWCNT	Ethanol	$FeCp_2$	Boric acid 1 wt %	0.97
B-MWCNTs	Ethanol	$FeCp_2$	Triethyl borate 1 wt %	0.51
P-MWCNTs	Ethanol	$FeCp_2$	Triphenyl phosphine 1 wt %	0.52

Various polyaromatic hydrocarbons and residual catalysts can be existed as by-products during B-MWCNTs synthesis. HCl is not an oxidation agent, and thus treatment with HCl can be used to remove a metal catalyst and polyaromatic hydrocarbon on the nanotubes surface [154]. To modify the B-MWCNTs, B-MWCNTs were treated with a mixture of concentrated H_2SO_4 and 30% H_2O_2 (3:1). Those cases lead to an increase in the structural disorder of B-

MWCNTs due to the formation of defects on the nanotube's surface. Raman spectroscopy was used to quantify the effects of HCl treatment and oxidative functionalisation on the change defect density of B-MWCNTs. A comparison of Raman spectra recorded for B-MWCNTs, B-MWCNTs with HCl treatment and B-MWCNTs with oxidative functionalisation by piranha solution can be seen in Figure 3.2 and Table 3.2

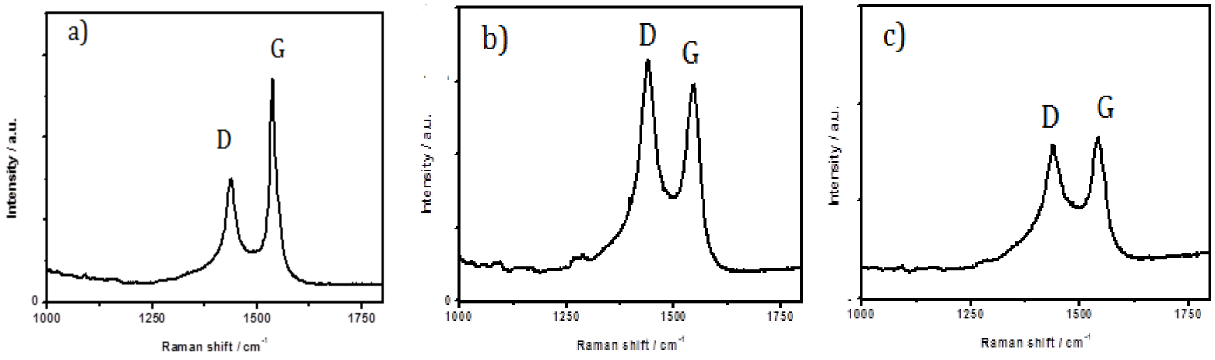

Figure 3.2 The comparison of Raman spectra of a).B-MWCNTs (triethyl borate 1 wt %), b).B-MWCNTs (triethyl borate 1 wt %)/HCl, c).B-MWCNTs (Triethyl borate 1 wt %)/Piranha

The comparison of I_D/I_G ratio of B-MWCNTs before and after HCl treatment and the oxidative functionalisation indicates that the disorder level of B-MWCNTs increase after the oxidative functionalisation and HCl treatment. HCl treatment and oxidative functionalisation decreases the crystallinity level of B-MWCNTs and increase the defect density.

Table 3.2 The intensity ratio of D and G bands (I_D/I_G) for B-MWCNTs before and after HCl treatment and oxidative functionalisation.

Material	Carbon precursors	Catalyst	Doping Precursors	I_D/I_G
B-MWCNTs	Ethanol	$FeCp_2$	TEB 1 wt %	0.51
B-MWCNTs/HCl	Ethanol	$FeCp_2$	TEB 1 wt %	1.13
B-MWCNTs/Piranha	Ethanol	$FeCp_2$	TEB 1 wt %	0.96

The high intensity of D-band, as well as high I_D/I_G ratio in B-MWCNTs with oxidative functionalisation, is probably caused by the presence of hydroxyl and carboxyl functional groups on nanotube surfaces.

Raman spectra is highly sensitive to structural imperfection, such as the finite size of crystallite, lattice defect, and the edges of the graphitic layer [155]. To study the effect of the defect density, activated by the increasing of dopant concentration on Raman spectra, the B-MWCNTs were grown by CVD at 850°C using propanone with 2.0wt % of $FeCp_2$, and TEB as boron precursor, at different concentration. The B-MWCNTs charaterisations were performed by Raman spectroscopy. Figure 3.3 shows the Raman spectra of different compositions of triethyl borate concentration in B-MWCNTs from propanone carbon feed stock. The I_D/I_G ratios are summarized in Table 3.3

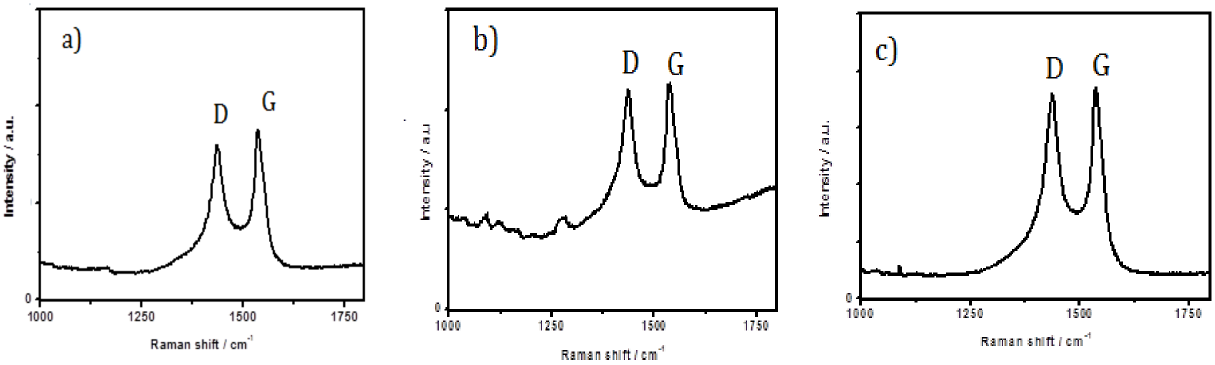

Figure 3. 3 The comparison of Raman spectra of a).B-MWCNTs (TEB 0.5 wt %), b).B-MWCNTs (TEB 2 wt %) c).B-MWCNTs (TEB 3 wt %).

The I_D/I_G ratios from 0.89 to 1.00 as the increase of TEB concentration indicated an increasing disorder level of nanotubes, decreasing the nanotubes crystallinity. The increase of I_D/I_G value demonstrates high degree of defects in the B-MWCNTs structure. The quantitative analysis of Raman spectra (Table 3.2 and Table 3.3) shows that the I_D/I_G ratio of propanone based B-MWCNTs is higher than ethanol based B-MWCNTs. The results confirmed that the defect density in the B-MWCNTs was strongly affected by the type carbon precursors and the catalyst/doping ratio.

Table 3.3 Intensity ratio of D and G bands (I_D/I_G) for B-MWCNTs with different doping concentrations.

Material	Carbon precursor	Catalyst $FeCp_2$ (wt %)	Doping TEB (wt %)	I_D/I_G
B-MWCNTs	Propanone	2	0.5	0.89
B-MWCNTs	Propanone	2	2	1.00
B-MWCNTs	Propanone	2	3	0.96

To study the effect of the catalyst/doping ratio in the P-MWCNTs synthesis on defects density, the P-MWCNTs were grown by CVD at 900°C using cyclohexane at different $FeCp_2$/TPP concentrations. The Raman intensity ratio I_D/I_G of D and G bands was used to quantify the change in defect density. The relationship between doping/catalyst ratio in P-MWCNTs and the Raman spectra is shown in Figure 3.4 and Table 3.4. The D, G, G' bands represent the characteristics of the P-MWCNTs.

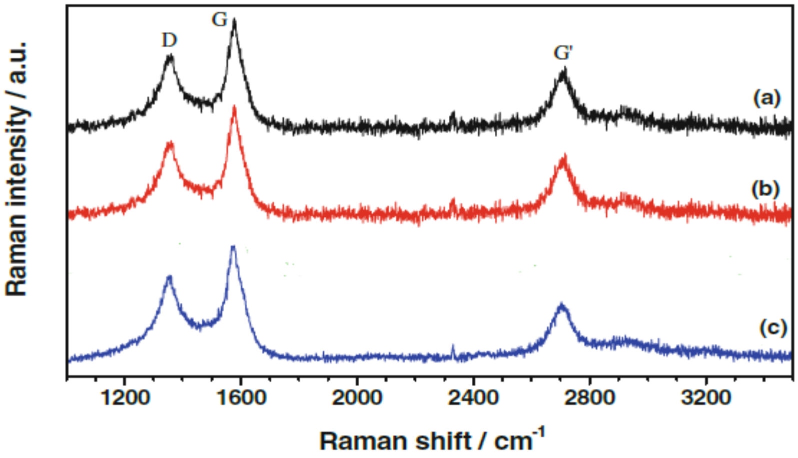

Figure 3.4 Raman spectra of P-MWCNTs composite films a).$FeCp_2$/TPP (5:2 wt %), b). $FeCp_2$/TPP (2:2 wt %) c).$FeCp_2$/TPP (2:1wt %).

The I_D/I_G ratio of the Raman spectra of the P-MWCNTs shows that the increasing of the catalyst concentration from 2% to 5% does not significantly influence the increase of the defect density of P-MWCNTs.

Table 3.4 The intensity ratio of D and G-bands (I_D/I_G) for P-MWCNTs with different catalyst/doping concentrations.

Material	Carbon precursors	Catalyst $FeCp_2$ (wt %)	Doping TPP (wt %)	I_D/I_G
P-MWCNTs	Cyclohexane	5	2	0.66
P-MWCNTs	Cyclohexane	2	2	0.66
P-MWCNTs	Cyclohexane	2	1	0.53

Raman spectra reveals that P-MWCNTs with $FeCp_2$/TPP (2:1 wt %) exhibits higher (I_D/I_G) as compared to P-MWCNTs with $FeCp_2$/TPP (2:2 wt %). This result indicates that P-MWCNTs with $FeCp_2$/TPP (2:1 wt %) show lower crystallinity and higher defect density compared to P-MWCNTs with $FeCp_2$/TPP (2:2 wt %). The excess of TPP relative to $FeCp_2$ suppress the MWCNTs growth and does not cause the higher concentration of phosphorus in sp^2 bonded MWCNTs [156]. It was reported that in a P-MWCNTs synthesis using ferrocene-triphenyl phosphine, Fe_2P, Fe_3P, and Fe_3C can be produced as reaction by-product [105].

3.2 Boron doped MWCNTs.

3.2.1. Electrochemical characteristics of B-MWCNTs

Low magnification SEM images, shown in Figure 3.5, revealed that CNTs with different morphologies grow on Si/SiO_2 substrate from two different sources of doping (boric acid and triethyl borate) in ferrocene and ethanol catalyst carbon precursors mixture. The SEM shows that the B-MWCNT is clean from amorphous carbon. Tiny nanotubes, homogenously distributed on silicon-silicon oxide wafer surface, were observed.

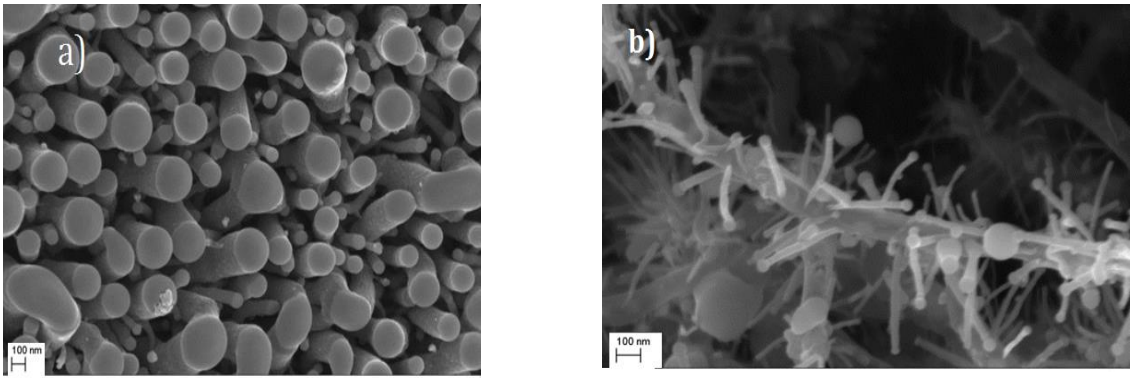

Figure 3.5 SEM micrographs of B-MWCNTs using two different doping precursors a).boric acid (1.0 wt %), b).triethyl borate (1.0 wt %).

A different source of boron doping material in a ternary mixture of doping,catalyst and carbon feedstock showed different behaviors towards B-MWCNTs synthesis. In the presence of ferrocene catalyst, vertically aligned B-MWCNTs can be produced by the decomposition of ethyl alcohol and boric acid (Figure 3.5a) whereas Y-shaped B-MWCNTs can be synthesized by decomposition of ethyl alcohol and triethyl borate (Figure 3.5b). In Y-shaped structure, it was found that the nanotube branch had a smaller diameter than the rod. Since the reactivity of CNTs is sensitive to the diameter and the nanotube curvature, the different diameter value may lead to the formation of a new heterogeneous electrochemical system in the CNTs. The Y-shaped structure in the nanotube branch indicates the presence of a non-hexagonal shape in the CNTs structure. The structural model of Y-shaped CNTs can be seen in Figure 3.6. The folded carbon ring and non-hexagonal carbon structure appear in a Y-shaped CNTs structure [157,158].

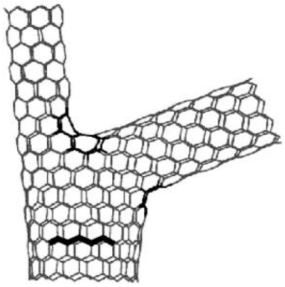

Figure 3.6 The structural models of asymmetric Y-shaped CNTs non-hexagonal carbon rings highlighted in black [157,158]

TEM analysis (Figures 3.7a and 3.7b) show that the end tube caps curvature of B-MWCNTs is related to the type of doping sources. Triethyl borate doping shows higher end tube curvature than boric acid in B-MWCNTs.

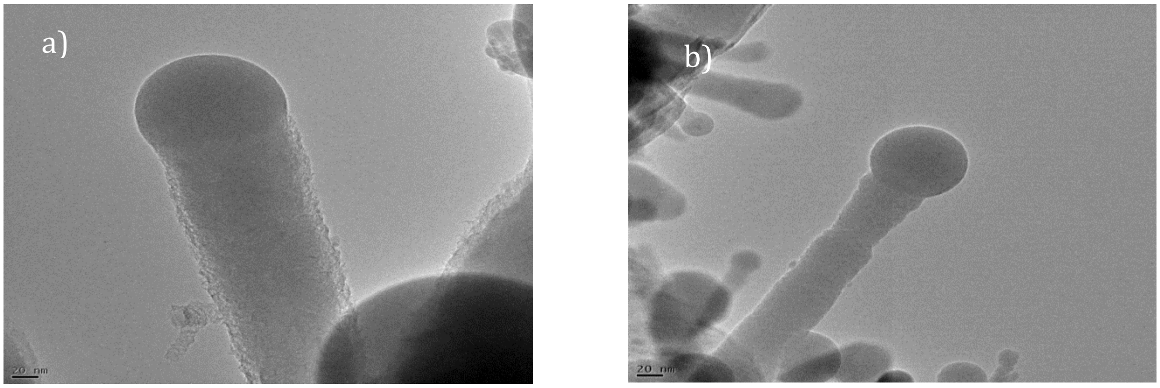

Figure 3.7 TEM micrographs of B-MWCNTs using two different doping precursors a).boric acid (1wt %), b).triethyl borate (1wt %)

Energy loss near the edge structure (ELNES) in the EELS spectrum in the scanning TEM mode was used to provide information on the boron existence in the Y-shaped B-MWCNTs structure (Figure 3.8). The nanotubes gave edge characteristic in EELS related to K-shell ionisation 1s π* and 1s σ* of boron at 195.6 eV and 202.2 eV, respectively. The 1s π* peak indicates that boron is substituted with carbon in the sp^2 carbon nanotubes network. A high boron dopant can be found in the upper cups of the MWCNTs.

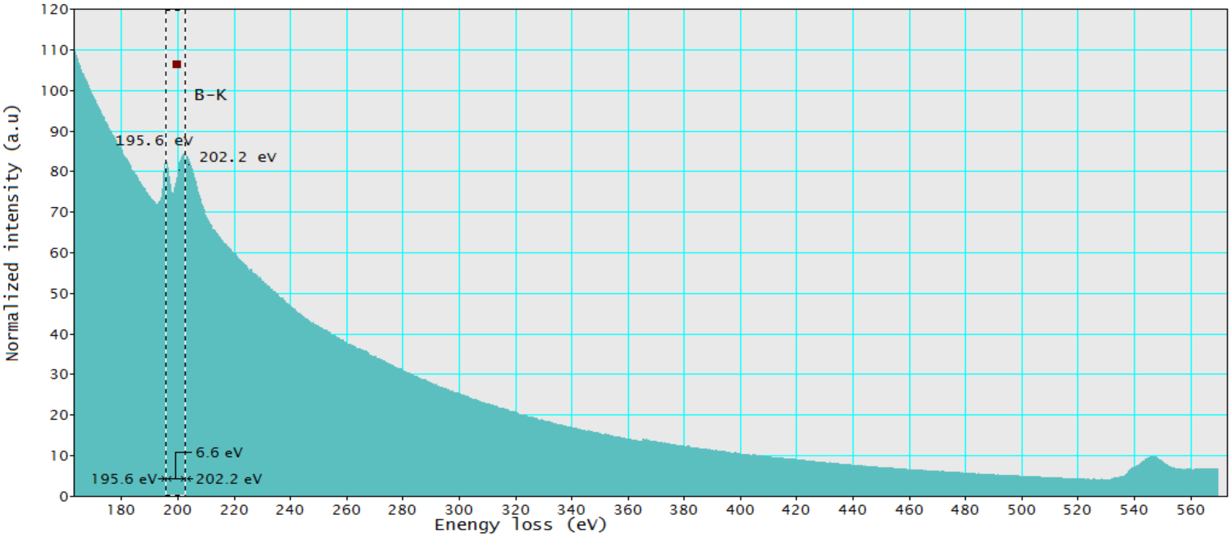

Figure 3.8 EELS spectrum of Y-shaped B-MWCNTs caps

The electron energy loss spectroscopy (EELS) spectra analysis of B-MWCNTs clearly indicates the presence of boron in the samples along with carbon, oxygen, and iron in both

B-MWCNTs sample. It is well known that boric acid displays good solubility in concentrated HCl. The SEM images taken for HCl treated B-MWCNTs films confirm that after treatment with hydrochloric acid the upper parts of carbon nanotubes are completely eliminated, and that fairly empty (unfilled) carbon nanotubes are formed (Figures 3.9a and 3.9b).

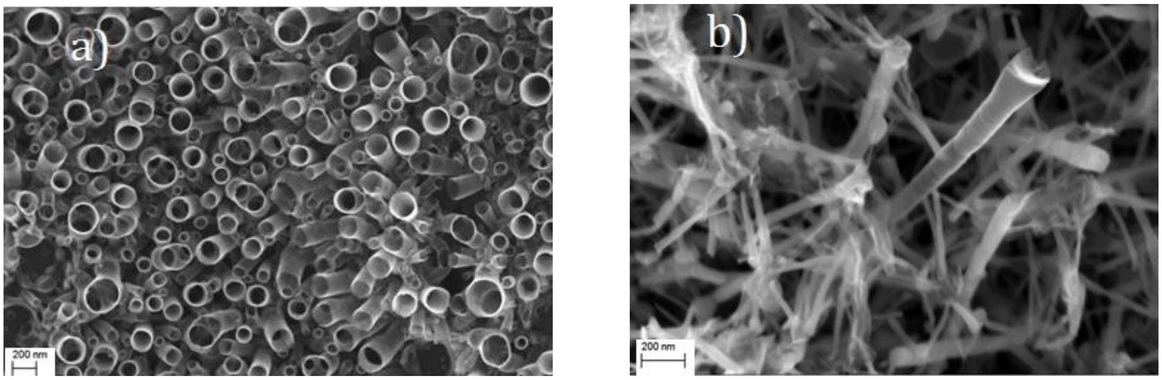

Figure 3.9 SEM micrographs of a).B-MWCNTs (BA 1.0wt %)/HCl, b).B-MWCNT (TEB 1.0wt %)/HCl

TEM analysis of HCl treated B-MWCNTs films confirms that the source of boron doping not only affects the B-MWCNTs morphology and B-MWCNTs upper parts structure, but also the properties of the inner structure of MWCNTs (Figure 3.10a). Hollow B-MWCNTs can be produced by HCl treatment of B-MWCNTs (BA 1.0 wt %), whereas bamboo-like B-MWCNTs with open caps structure can be synthesized by HCl treatment of B-MWCNTs (TEB 1.0 wt %) (Figure 3.10b).

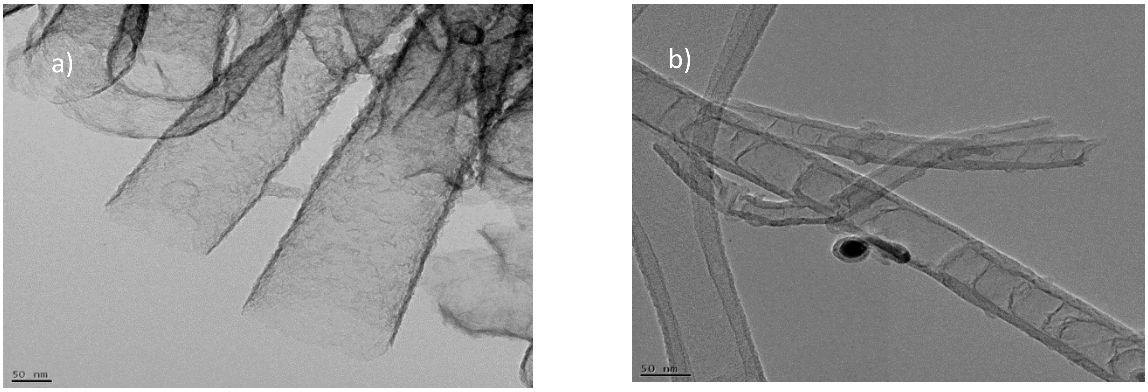

Figure 3. 10 TEM micrographs of a).B-MWCNTs (BA 1.0 wt %)/HCl, b).B-MWCNTs (TEB 1.0 wt %)/HCl

XPS is one of the surface characterisation techniques that is used to provide feature information on the nature of the functional groups, composition, and chemical bonding on the nanotubes surface. Figure 3.11 displays the XPS spectra of the B-MWCNTs and B-MWCNTs/HCl. Boron, iron, oxygen, carbon, and silicon were detected in the MWCNTs films. Assuming a film with homogenous element distribution, the film composition was determined by an XPS quantitative analysis. Table 3.5 shows the elemental composition (%) of the B-MWCNT and B-MWCNTs/HCl on silicon/silicon oxide wafers, estimated by XPS.

Table 3.5 Elemental composition analysis of B-MWCNTs and B-MWCNTs/HCl (H_3BO_3 doping source) by XPS.

Sample	Fe	O	C	B	Si
B-MWCNTs	1.8	13.9	74.9	6.9	2.4
B-MWCNTs/HCl	<0.1	2.0	96.9	0.3	0.8

The XPS spectra reveals that boron and iron are incorporated into the B-MWCNTs film, both are in their oxidised form (iron oxide and boron oxide) with a $Fe_2P_{3/2}$ and B_1s binding energy of 711.4 eV, and 192.2 eV, respectively. The O_{1s} spectrum at 523.3 and 531.1 eV, reflecting the different oxide phases of iron, boron, and silicon in the B-MWCNTs films. After the HCl treatment of the B-MWCNTs films, it was found that the amount of iron, boron, and silicon were reduced. The HCl-treated B-MWCNTs show a significant decrease in the oxygen amount on the nanotube surface as compared to the untreated B-MWCNTs. The excess amounts of oxygen corresponding to boron and iron were removed from the B-MWCNTs sample using HCl treatment.

The C1 signal with maximum intensity at 284.3 eV is typical for the sp^2 peak of MWCNTs [154,159]. There is no indication for the hydrogen-rich carbon molecules, residual graphite-like structure and carbon functional group that exist in B-MWCNTs and B-MWCNTs/HCl films. The three peaks of B1s at 192.2 eV, 189.5 eV, and 186.7 eV indicate the B-C in different stoichiometry in the sp^2 carbon network. The XPS spectra show that boron can be incorporated into MWCNTs structure by a CVD synthesis.

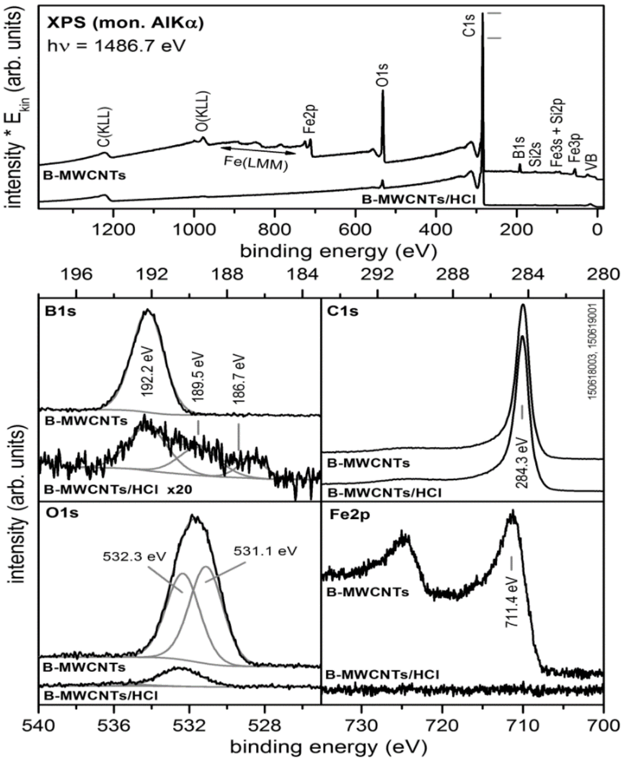

Figure 3.11 XPS measurement spectra (transmission-corrected) as well as C1s, B1s (enhanced by a factor of 20 for the HCl-treated sample), O1s and Fe2p detail spectra of B-MWCNTs and B-MWCNTs/HCl composite films on Si/SiO2 substrates [160].

The oxidation of B-MWCNTs can be an effective process to decorate the graphitic surface with oxygen-filled contained groups, mainly carboxyl, and hydroxyl. The presence of oxygen-contained groups in MWCNTs leads to a change in the double layer characteristics of carbon nanotubes.

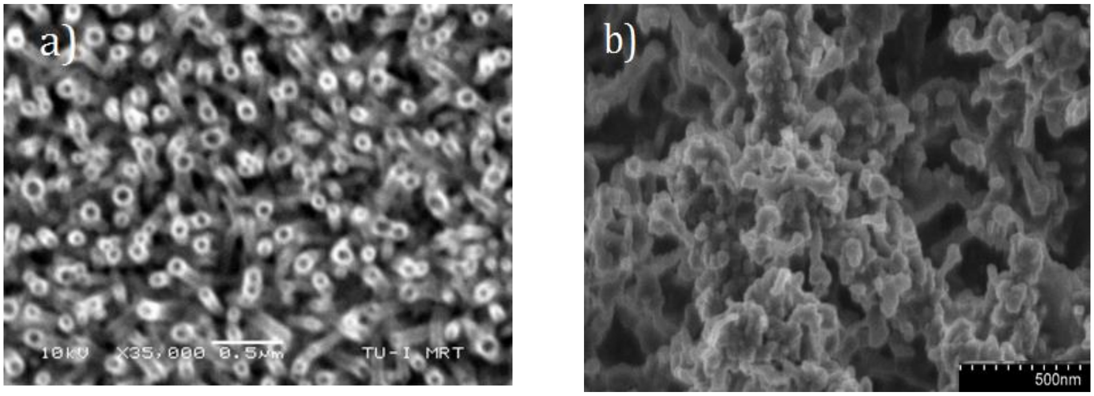

Figure 3.12 SEM micrographs of B-MWCNTs oxidation with piranha solution a). Vertically aligned B-MWCNTs, b). Y-shaped B-MWCNTs.

Figure 3.12 shows the oxidation of vertically aligned B-MWCNTs and Y-shaped B-MWCNTs with piranha solution. SEM was used to observe the morphological changes on the B-

MWCNTs. The changes in the B-MWCNTs morphologies were detected in the vertically aligned B-MWCNTs structure and Y-shaped B-MWCNTs. From the Figure 3.10, it can be seen that the treatment of vertically aligned B-MWCNTs with piranha solution eliminates the upper parts structure of B-MWCNTs. Meanwhile, piranha treated Y-shaped B-MWCNTs film eliminates the nanotube branch in the B-MWCNTs.

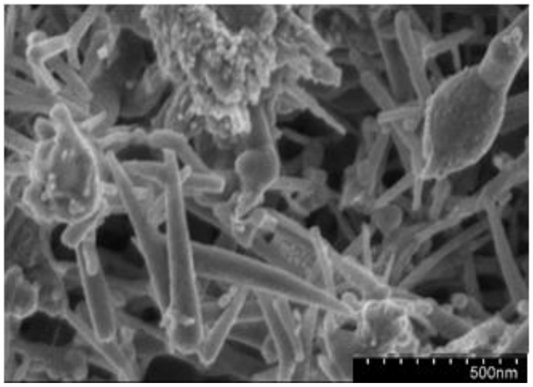

Figure 3.13 Y-shaped B-MWCNTs decorated with gold nanoparticle

Representative SEM images of Y-shaped B-MWCNTs decorated with gold nanoparticle is shown in Figure 3.13. The SEM micrographs, taken for B-MWCNTs modified gold nanoparticle, reveal that the gold nanoparticles are dispersed onto the B-MWCNT's surface. An agglomeration of gold nanoparticles can be seen in the Y-shaped B-MWCNTS branch. SEM micrographs exhibit that the morphology of Y-shaped B-MWCNTs changes slightly after being coated by gold nanoparticle.

Cyclic voltammetry and impedance spectroscopy were used to investigate the electrochemical characteristics of the vertically aligned B-MWCNTs and the Y-shaped B-MWCNTs. The electrochemical properties of the vertically aligned B-MWCNTs and the Y-shaped B-MWCNTs were characterised by using the standard redox system $[Fe(CN)_6]^{3-/4-}$ in aqueous KCl solution (1.0 M) in the concentration range of 0.1-1 mM. The CVs recorded for these electrodes are presented in Figures 3.14a. and 3.14b.

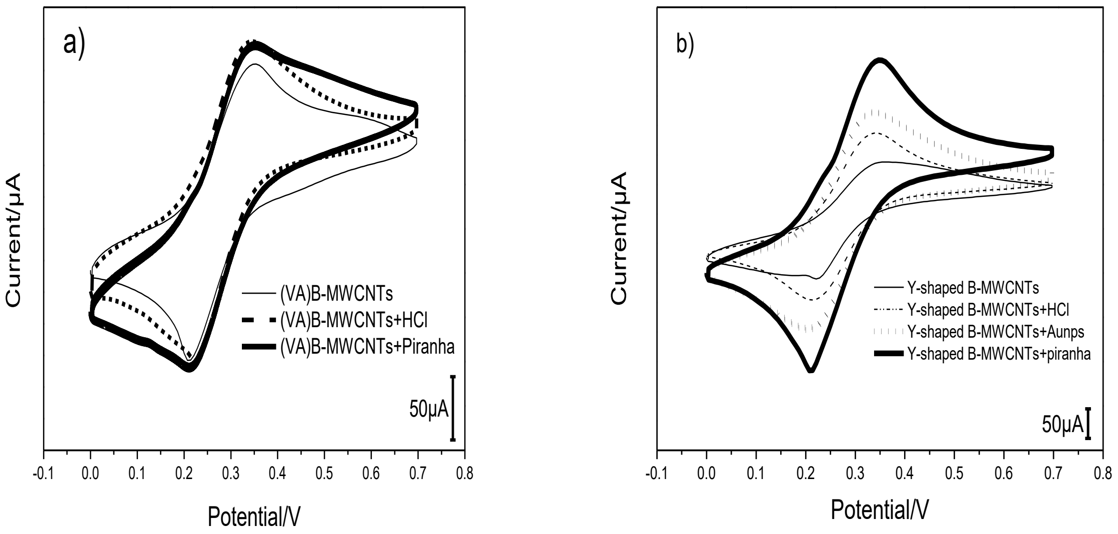

Figure 3.14 CVs recorded for 0.5 mM $[Fe(CN)_6]^{3-/4-}$ (1.0 M KCl) at scan rate 0.02 V s^{-1} on a).vertically aligned B-MWCNTs b).Y-shaped B-MWCNTs films (vs Ag/AgCl).

Figure 3.14a shows the voltammetric response at three different electrodes (vertically aligned B-MWCNTs, vertically aligned B-MWCNTs after HCl treatment, and vertically aligned B-MWCNTs after oxidation functionalisation). The treated B-MWCNTs electrodes show a slight shift in the peak separation (ΔE_p) below the untreated vertically aligned B-MWCNTs. The same behavior was observed for the Y-shaped B-MWCNTs (Figure 3.14b). The variation in ΔE_p illustrates the variability of the electrode structure.

The peak to peak potential separation is related to the heterogeneous electron transfer constant. The heterogeneous electron transfer constants (K_s) of vertically aligned B-MWCNTs and Y-shaped B-MWCNTs was estimated through peak potential separation (ΔE_p) via the Nicholson equation [147]. The peak separation and K_s value for the vertically aligned B-MWCNTs and Y-shaped B-MWCNTs electrodes toward $[Fe(CN)_6]^{3-/4-}$ redox system are summarized in Table 3.6.

Table 3.6 The estimated ΔE_p and K_s parameters for B-MWCNTs.

Films	ΔE_p /(V)	K_s /(cm s^{-1})
Vertically aligned B-MWCNTs	0.143	5.6 x 10^{-4}
Vertically aligned B-MWCNTs /HCl	0.114	8.9 x 10^{-4}
Vertically aligned B-MWCNTs/Piranha	0.132	6.5 x 10^{-4}
Y-shaped B-MWCNTs	0.136	6.1 x 10^{-4}
Y-shaped B-MWCNTs/HCl	0.132	6.5 x 10^{-4}
Y-shaped B-MWCNTs/Piranha	0.131	6.6 x 10^{-4}
Y-shaped B-MWCNTs/ AuNPs	0.123	7.4 x10^{-4}

The electrodes kinetics of B-MWCNTs toward $[Fe(CN)_6]^{3-/4-}$ redox system is strongly influenced by the type of B-MWCNTs, end tube structure, surface chemistry of B-MWCNTs and defect density. The HCl treatment of B-MWCNTs relates to a modification of the upper parts nanotube structure, an increase of the amount of dangling bond and the defect density in B-MWCNTs structure due to boron dissolution.

Oxidative functionalisation of B-MWCNTs with piranha solution incorporates several chemical functional groups on the electrode surface such as hydroxyl, carbonyl, and carboxyl groups. Oxidation makes MWCNTs more hydrophilic [161]. The decrease of ΔE_p in B-MWCNTs after oxidation indicates the barrier for interfacial electron transfer is decreased after oxidative functionalisation.

AuNPs deposition on B-MWCNTs electrode decreases the oxidation and reduction peak separation of $[Fe(CN)_6]^{3-/4}$ redox system. The results indicate that the presence of AuNPs improves the electrocatalytical properties of the B-MWCNTs electrodes.

CVs recorded for $[Fe(CN)_6]^{3-/4-}$ (1.0 M KCl) standard redox system on vertically aligned B-MWCNTs and Y-shaped B-MWCNT films at the scan rate of 0.02 V s^{-1} showing the effect of variation of concentration of the redox system in the concentration range of (0.1-1 mM) are displayed in Figure 3.15a, Figure 3.15c, Figure 3.15e, Figure 3.16a, and Figure 3.16c, Figure 3.16e, Figure 3.16g, respectively. The change of anodic current response of the vertically aligned B-MWCNTs and the Y-shaped B-MWCNTs film with the variation of concentration of

$[Fe(CN)6]^{3-/4-}$ is presented graphically in Figure 3.15b, Figure 3.15d, Figure 3.15f, Figure 3.16b and Figure 3.16d, Figure 3.16f, Figure 3.16h, respectively. From the linear concentration-current calibration curve, the detection limit and sensitivity values of the Y-shaped B-MWCNTs and the vertically aligned B-MWCNTs were estimated. Sensitivity is defined as the response of the curve slope or the response/dose [162]. The detection limit is the lowest amount of the analyte in a sample that can be detected. Based on the signal-to-noise approach, the limit of detection can be expressed as:

$$\text{limit of detection} = 3\,\sigma/\text{m} \qquad (3.1)$$

Where σ is the standard error and m is the slope of calibration line [163]. The detection limit and sensitivity of Y-shaped B-MWCNTs and vertically aligned B-MWCNTs are summarized in Table 3.7.

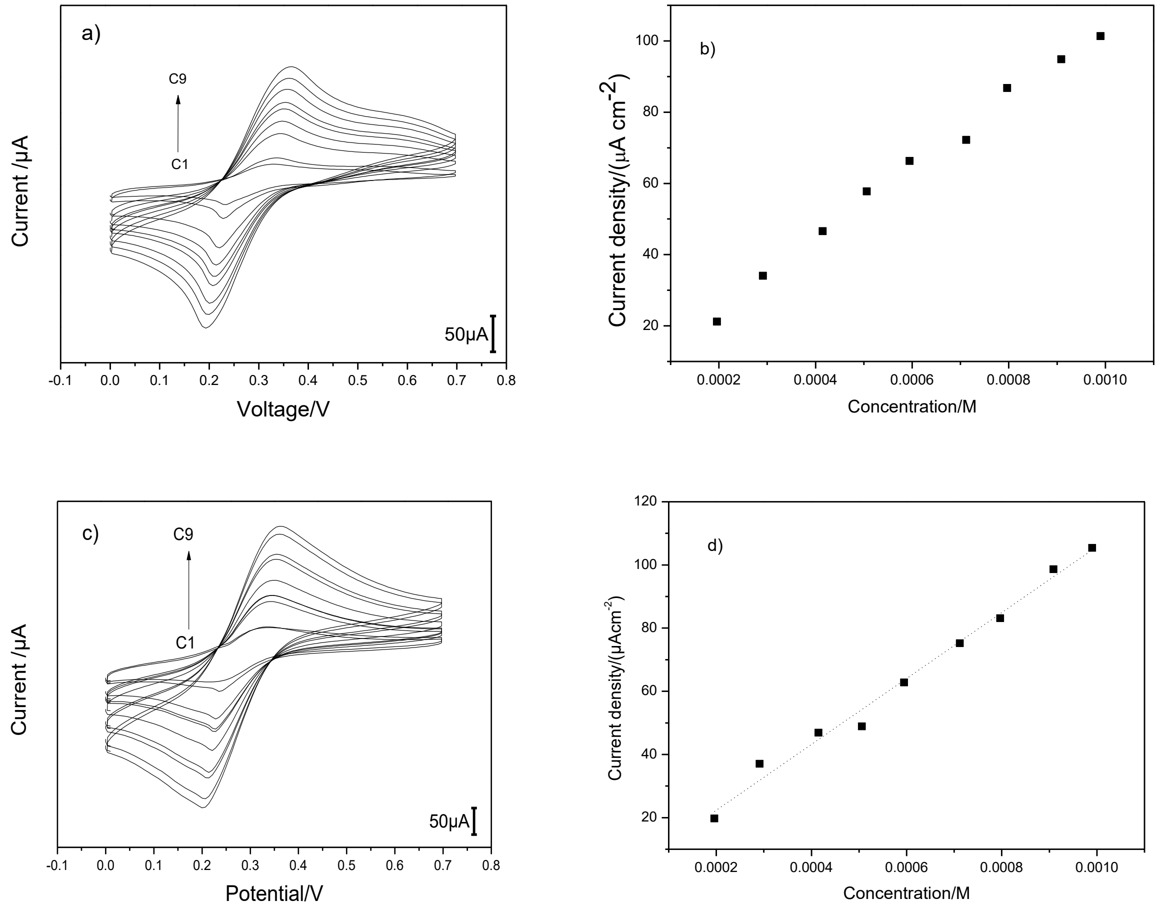

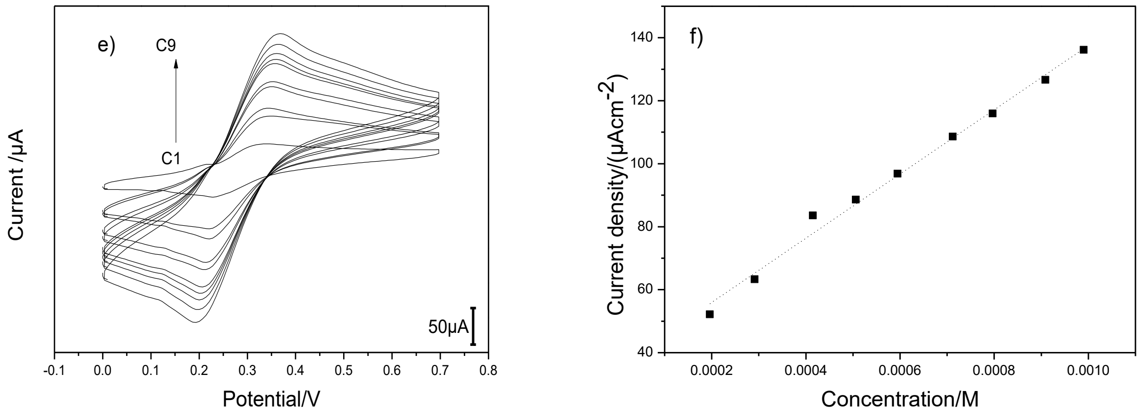

Figure 3.15 CVs and calibration curves for 0.1-1 mM $[Fe(CN)_6]^{3-/4-}$ (1.0 M KCl) at scan rate of 0.02 V s^{-1} on a,b).vertically aligned B-MWCNTs c,d).vertically aligned B MWCNTs/HCl e,f).vertically aligned B-MWCNTs/piranha (vs Ag/AgCl).

The results presented in Table 3.7 shows that the HCl treatment and the oxidative functionalisation of vertically aligned B-MWCNTs slightly change the sensitivity of the vertically aligned B-MWCNTs toward $[Fe(CN)_6]^{3-/4}$ redox system. The slightly changes in the sensitivity of vertically aligned B-MWCNTs after the HCl treatment and oxidative functionalisation can be related to the increase of active surface area due to the formation of the hollow tube structure.

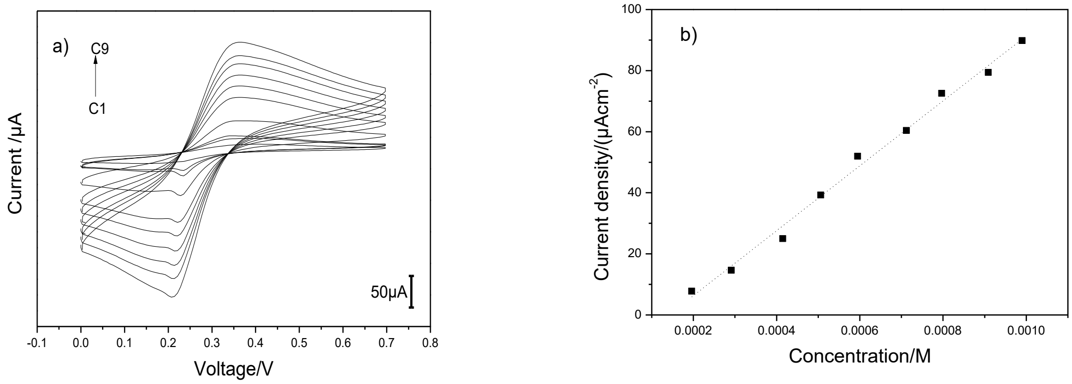

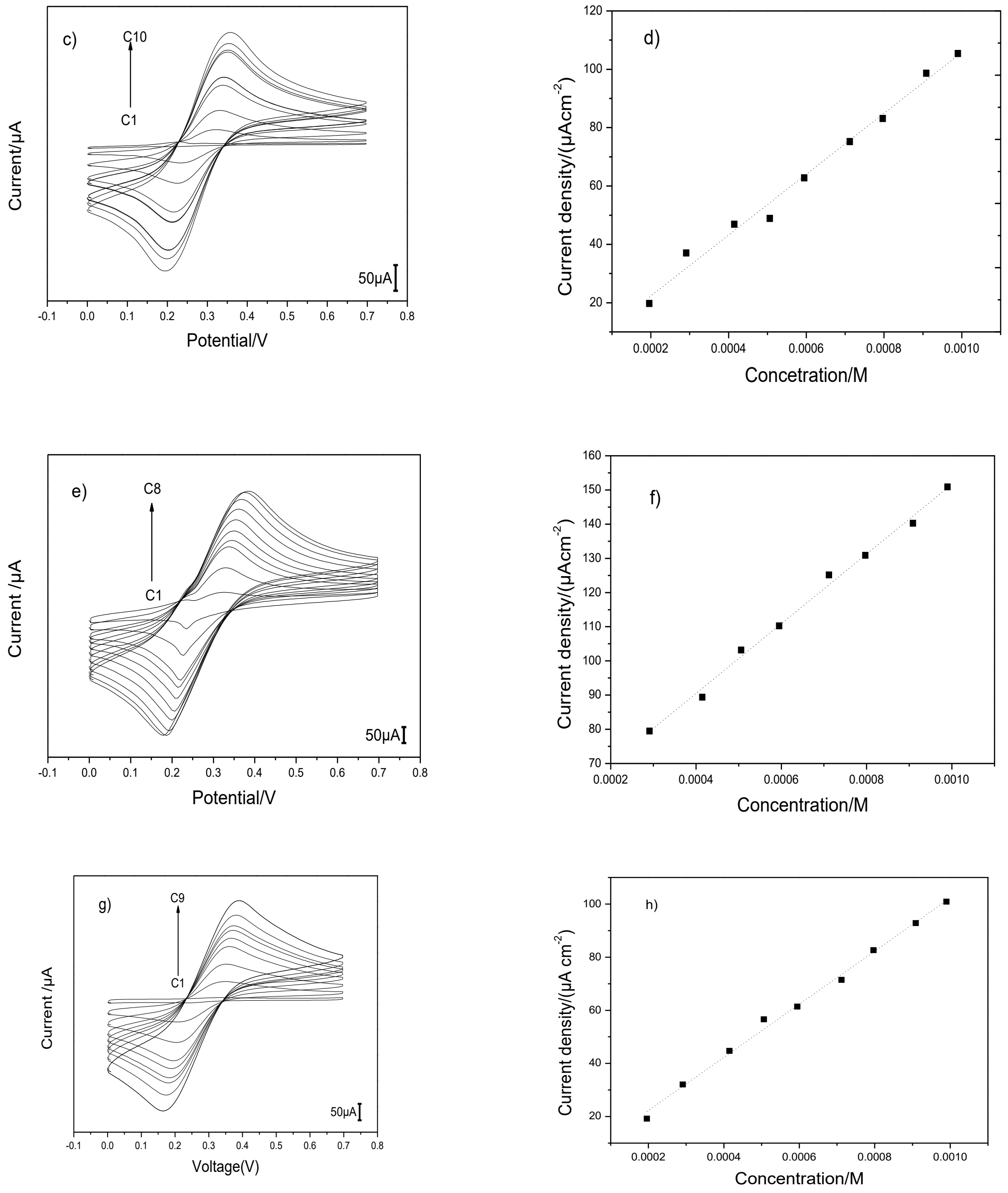

Figure 3.16 CVs and calibration curves for 0.1-1 mM $[Fe(CN)_6]^{3-/4-}$ (1.0 M KCl) at scan rate of 0.02 V s^{-1} on a,b).Y-shaped B MWCNTs, c,d)Y-shaped B MWCNTs/HCl, e,f).Y-shaped B - MWCNTs/piranha, g,h).Y-shaped B MWCNTs+ AuNPs (vs Ag/AgCl).

The agglomeration of gold nanoparticle on the Y-shaped B-MWCNTs surface and the structural damage of Y-shaped B-MWCNTs after oxidative functionalisation leads to a slightly changes the sensitivity of Y-shaped B-MWCNTs. Y-shaped B-MWCNTs decorated with AuNPs showed the highest detection limit toward the $[Fe(CN)_6]^{3-/4}$ redox system compared HCl treated and oxidative functionalisation of Y-shaped B-MWCNTs. The Y-shaped B-MWCNTs/AuNPs demonstrated better noise/sensitivity ratio than the Y-shaped B-MWCNTs/HCl and the Y-shaped B-MWCNTs/piranha. The lowering of limit detection of the Y-shaped B-MWCNTs and the vertically aligned B-MWCNTs towards the $[Fe(CN)_6]^{3-/4}$ redox system was comparable with pillar and horizontal MWCNTs but higher than carbon paste modified electrodes [164–166].

Table 3.7 Electrochemical sensing parameters computed using vertically aligned B-MWCNTs and Y-shaped B-MWCNTs.

Films	Sensitivity/ ($A\ mM^{-1}\ cm^{-2}$)	LOD/(µM)
Vertically aligned B-MWCNTs	99.6	64.2
Vertically aligned B-MWCNTs /HCl	104.3	79.4
Vertically aligned B-MWCNTs/Piranha	101.9	69.0
Y-shaped B-MWCNTs	106.3	63.4
Y-shaped B-MWCNTs/HCl	104.3	78.2
Y-shaped B-MWCNTs/Piranha	101.9	61.9
Y-shaped B-MWCNTs/ AuNPs	100	49.9
Pillar MWCNTs [a]		51
Horizontal MWCNTs [b]		78
$CP/BMPyBF_4$ [c]		100
CP/PEG [d]		100

[a] Pillar MWCNTs [164]
[b] Horizontal MWCNTs [164]
[c] 1-butyl-4-methylpyridium tetrafluoro Borate Modified Carbon Paste Electrode [165]
[d] Polyethylene glycol Modified Carbon Paste Electrode [166]

EIS can reveal information regarding the process occurring and the electrochemical characteristics of an electrochemical system, including double layer capacitance, charge transfer resistance, solution resistance and diffusion impedance In EIS, the electrochemical parameters are measured as a function of applied perturbation frequency [167].

In order to understand the electrochemical properties of B-MWCNTs electrode, impedance spectroscopy was carried out for the vertically aligned B-MWCNTs and the Y-shaped B-

MWCNTs, before and after the acid treatment and oxidative functionalisation. Figure 3.17 and Figure 3.18 display the impedance plots in the frequency range from 0.1 Hz to 100 KHz at B-MWCNTs electrode in the presence of 0.5 mM $[Fe(CN)6]^{3-/4-}$ in 1.0 M KCl. The EIS results in Figure 3.17 and Figure 3.18 were simulated by using the Randles equivalent circuit. Electrochemical parameters were estimated based on nonlinear curve fitting methods, using Thales and MEISP Kumho 3.0 software package [168]. The R_{ct} results in Figures 3.17 and 3.18 are summarized in Table 3.8.

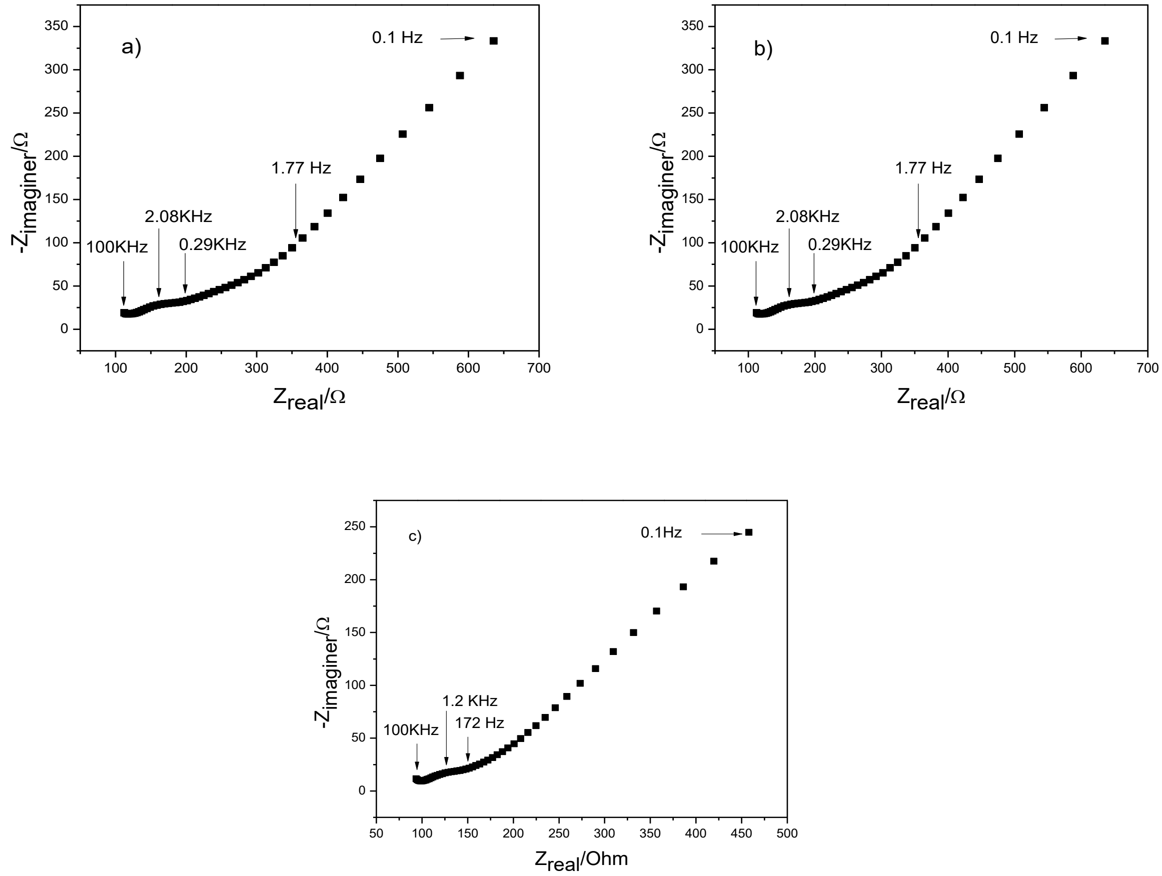

Figure 3.17 EIS recorded for 0.5 mM $[Fe(CN)_6]^{3-/4-}$ (1.0 M KCl) on a). vertically aligned B - MWCNTs, b). vertically aligned B-MWCNTs/HCl, c). vertically aligned B-MWCNTs/piranha.

In Nyquist plots, the diameter of a semicircle in high-frequency represents the electron transfer resistance (R_{ct}). The general relation between R_{ct} and the reaction kinetic by Butler Volmer is given by:

$$R_{ct} = \frac{RT}{nFI_o} \qquad (3.2)$$

Where I_o represents the exchange current of the reaction [169]. The relationship between the exchange current and the heterogenous electron transfer is given by the equation:

$$I_0 = nFAk_sC. \qquad (3.3)$$

The analysis of Figure 3.17 in Table 3.8 shows that the R_{ct} of the vertically aligned B-MWCNTs decreases with oxidative functionalisation and HCl treatment. A decrease in R_{ct} is evident of the change in electrodes kinetics. This result is in agreement with the CV measurements demonstrating that faster electrodes kinetics can be produced by opening the upper parts of nano tubes caps and by increasing the defect density through oxidative functionalisation.

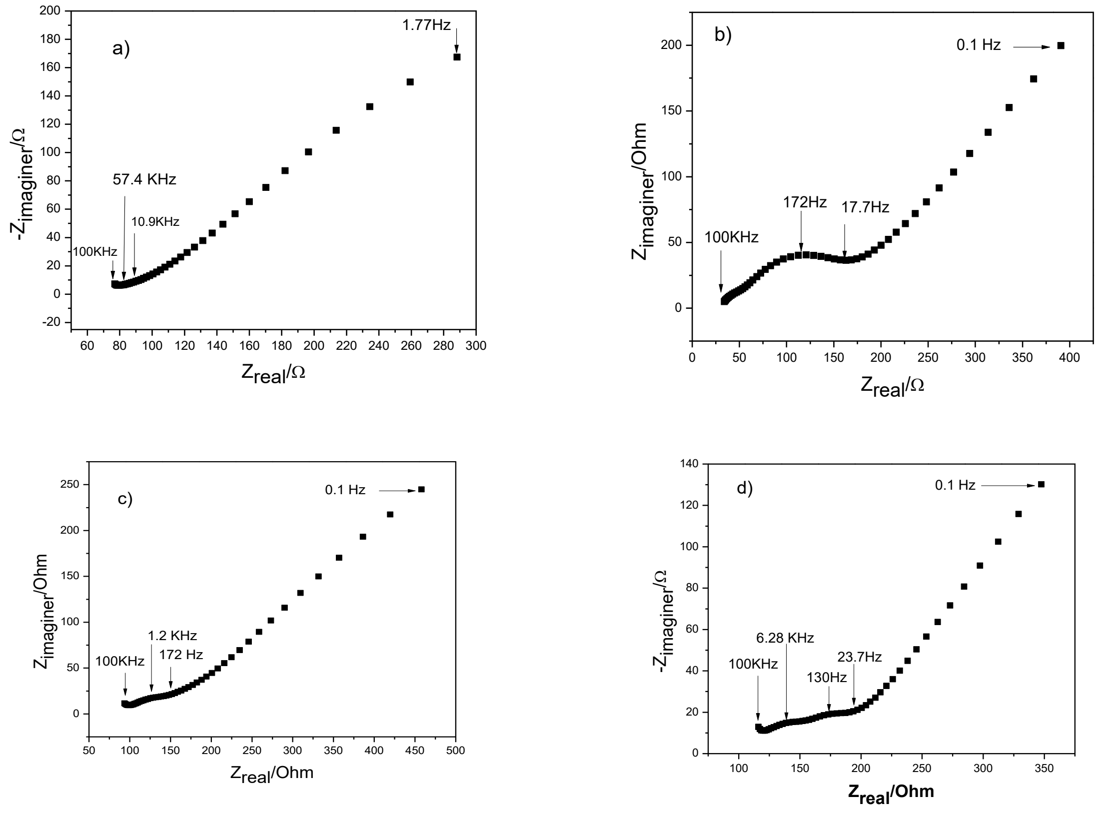

Figure 3.18 EIS recorded for 0.5 mM $[Fe(CN)_6]^{3-/4-}$ (1.0 M KCl) on a).Y-shaped B-MWCNTs, b).Y-shaped B-MWCNTs/HCl, c).Y-shaped B-MWCNTs/piranha d).Y-shaped B MWCNTs+ AuNPs.

The Nyquist diagram of $[Fe(CN)_6]^{3-/4-}$ at different Y-shaped B-MWCNTs electrodes in Figure 3.18 shows that the R_{ct} of Y-shaped B-MWCNTs decreases after the oxidative functionalisation and surface modification with AuNPs. The change of R_{ct} value was a strong proof that Y-shaped B MWCNTs have a significant impact on their kinetic after surface functionalisation by oxidation and gold nanoparticle. The modification of the Y-shaped B-MWCNTs with oxidation and gold nanoparticle had significantly enhanced the activity of electrode surface.

Table 3.8 Estimated EIS parameters for vertically aligned B-MWCNTs and Y-shaped B-MWCNTs.

Films	R_{ct} /(Ω cm^{-2})	C_{dl} /(μF)
Vertically aligned B-MWCNTs	92.1	1.56
Vertically aligned B-MWCNTs /HCl	34.1	1.51
Vertically aligned B-MWCNTs/Piranha	48.5	3.6
Y-shaped B-MWCNTs	27.2	6.2
Y-shaped B-MWCNTs/HCl	21.9	4.4
Y-shaped B-MWCNTs/Piranha	17.0	21.7
Y-shaped B-MWCNTs/ AuNPs	16.0	3.2

Oxidative functionalisation increases the C_{dl} value of vertically aligned B-MWCNTs and Y-shaped B-MWCNTs. The increasing of the C_{dl} is due to the surface charge effects and the change of the hydrophobic surface to hydrophylic of B-MWCNTs. It is well known that the C_{dl} value is affected by many variables such as electrode potential, temperature, ionic concentration, oxide layer, roughness and impurity adsorption [170].

3.2.2. The effects of carbon source on electrochemical characteristics of B-MWCNTs.

Figure 3.19 shows the SEM micrographs of B-MWCNTs film from two different carbon precursors, fabricated by the decomposition of ethanol and propanone in the presence of ferrocene catalyst and triethyl borate doping sources material. The SEM micrographs show that B-MWCNTs produced from propanone contained many carbon cluster on the nanotube surface, whereas, B-MWCNTs produced from ethanol are quite clean from carbon nano cluster of other carbon structures. An asymmetric nanotube branched with Y-shaped structure was observed in B-MWCNTs from ethanol-ferrocene-triethyl borate ternary mixture.

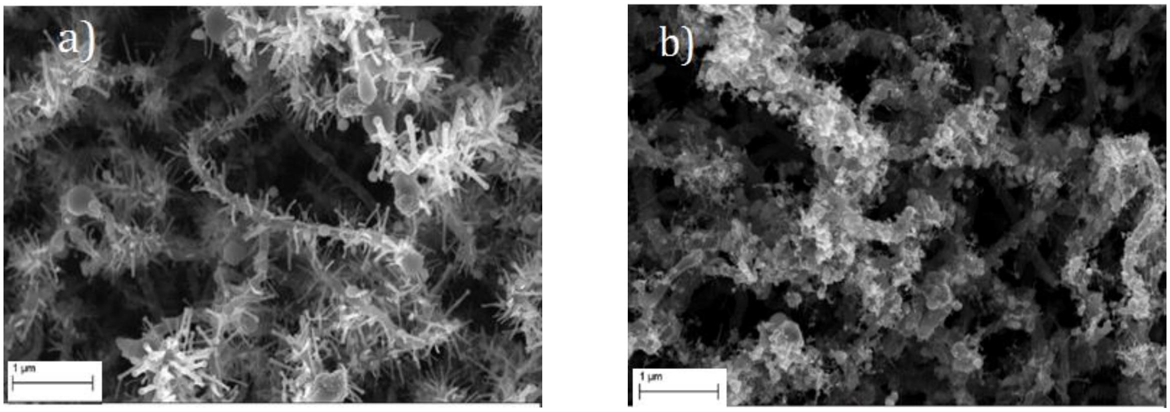

Figure 3.19 SEM of B-MWCNT produced from a).ethanol, b).propanone

The TEM investigations showed that the caps structure and surface morphology of B-MWCNTs were sensitive to carbon sources (Figure 3.20a and 3.20b). B-MWCNTs from ethanol have a hemispherical cap, whereas, B-MWCNTs from propanone have a relatively flatter cap. Propanone produces B-MWCNTs with heterogenous surfaces. The TEM images in Figure 3.20b confirms the presence of heterogeneous carbon cluster in the B-MWCNTs surface produced from propanone. Ethanol produces more homogenous B-MWCNTs surface than propanone.

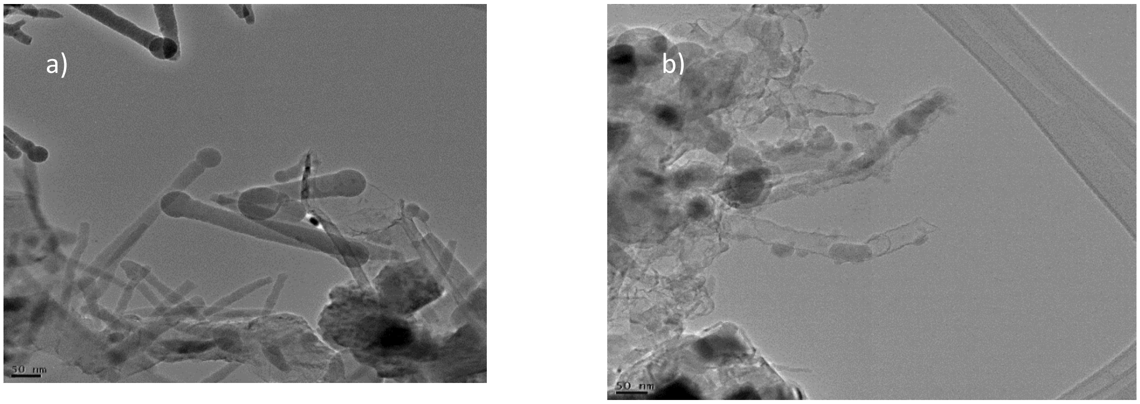

Figure 3.20 TEM of B-MWCNT produced from a).ethanol, b).propanone

Figure 3.21 shows the cyclic voltammograms of 0.5 mM $[Fe(CN)_6]^{3-/4}$ in (1.0 M KCl) at different B-MWCNTs films. It was observed that B-MWCNTs electrodes with carbon cluster have lower ΔE_p (0.112 V) than Y-shaped B-MWCNTs (0.136 V). This finding clearly indicates a strong influence of synthesis methods to the electrochemical properties of B-MWCNTs. The corresponding variation of electrode kinetic was also observed. The K_s value of Y-shaped B-MWCNTs is about 6.1 x 10^{-4} cm s^{-1}, whereas the Ks value of B-MWCNTs with nano graphitic cluster is about 9.2 x 10^{-4} cm s^{-1}. It was reported that amorphous carbon impurities play an active role in redox process of carbon nanotubes. Amorphous carbon black decreases the ΔE_p and increases the heterogenous electron transfer [171].

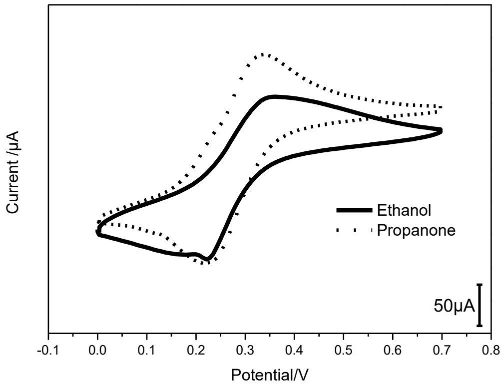

Figure 3.21 CVs recorded for 0.5 mM $[Fe(CN)_6]^{3-/4-}$ (1.0 M KCl) at scan rate 0.02 V s^{-1} on B-MWCNTs synthesis from different carbon source (ethanol and propanone) (vs Ag/AgCl).

The EIS measurement of the various structures of B-MWCNTs electrodes provides information regarding the electrochemical reaction on an electrode surface and is required in order to study the effect of the impurities and nanotube structure on the electrochemical properties of carbon electrodes. Figure 3.22 displays the impedance plots in frequency range of 0.1 Hz-100 KHz at the B-MWCNTs electrode in the presence of 0.5 mM $[Fe(CN)_6]^{3-/4}$ in 1.0 M KCl.

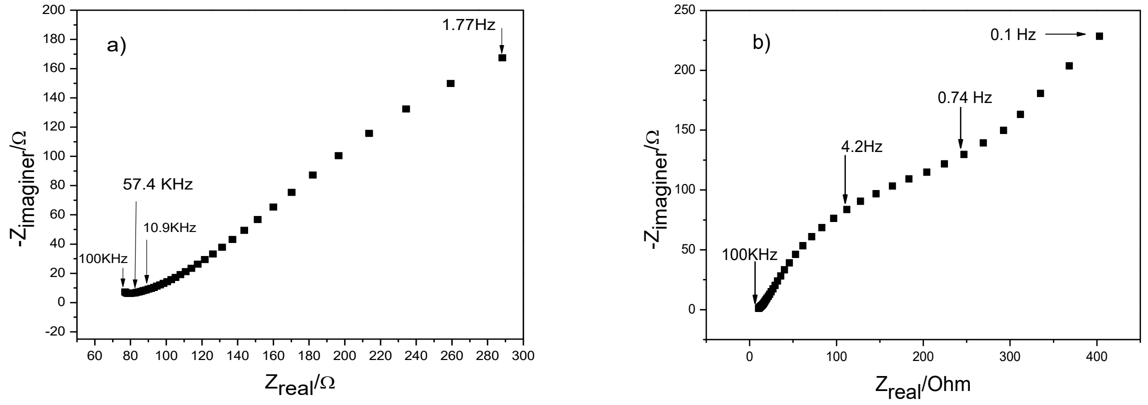

Figure 3.22 EIS recorded for 0.5 mM $[Fe(CN)_6]^{3-/4-}$ (1.0 M KCl) on B-MWCNTs synthesis from different carbon sources a).ethanol, b).propanone.

Considering the case of interfacial electrochemical reactions in presence of semi-infinite linear diffusion of electroactive particle to flat electrodes, the Randles equivalent circuit was used to fit the Y- shaped B-MWCNTs electrodes impedance. The contribution of the cluster of nanoparticle was calculated in the impedance curve fitting for B-MWCNTs with nano graphitic carbon [172,173]. Small particle and porous electrodes show low-frequency arc characteristics in an impedance spectroscopy [172]. A high-impedance frequency is needed for a small value capacitance double layer characterization. Table 3.9 summarizes the electrochemical properties of electrodes that were obtained from the fitting process.

Table 3.9 The comparison of electrochemical properties for B-MWCNTs from different carbon sources.

Films	ΔE_p/(V)	K_s/ (cm s^{-1})	R_{ct}/ (Ω cm^{-2})	Sensitivity/ (A mM^{-1} cm^{-2})	LOD/ (μM)
B-MWCNTs (ethanol)	0.136	6.1×10^{-4}	27.2	106.3	63.9
B-MWCNTs (Propanone)	0.112	9.2×10^{-4}	19.4	102.3	110.7

As shown in Table 3.9, it can be seen that B-MWCNTs with carbon cluster show lower charge transfer resistance than Y-shaped B-MWCNTs. The electrode kinetic of B-MWCNTs containing nano graphitic carbon is faster than that of Y-shaped B-MWCNTs. However, Y-shaped B-MWCNTs have a better detection limit than B-MWCNTs which contain nano graphitic carbon.

3.2.3. The effects of doping concentration on electrochemical characteristics of B-MWCNTs.

Figure 3.23 shows SEM micrographs of the effects of various triethyl borate concentrations (0.5-3.0 wt %) in B-MWCNTs film synthesis from ferrocene-propanone, a catalyst-carbon precursors mixture. The main advantage of this composition production method lies on the possibility of introducing high boron doping concentration to the B-MWCNTs structure. Triethyl borate shows very good solubility in a propanone-ferrocene mixture.

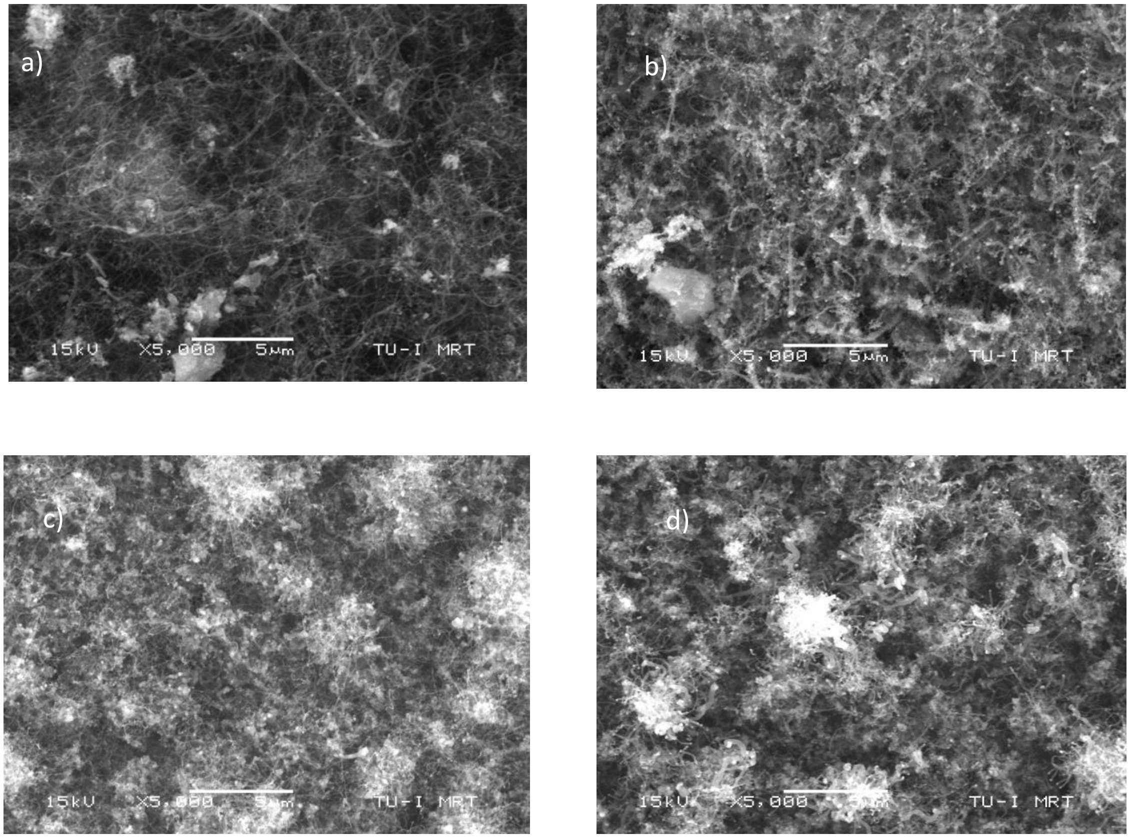

Figure 3.23 SEM images of a).MWCNTs, b).B-MWCNT (TEB 1 wt %), c).B-MWCNT (TEB 2 wt %), d).B-MWCNT (TEB 3 wt %).

The SEM investigation showed that the presence of triethyl borate leads to decrease the length of MWCNTs. An increase of doping source concentration would, therefore, increase the inclusion on B-MWCNTs surface. The TEM image in Figure 3.24 showing the morphology of B-MWCNTs exhibits that an inhomogeneous graphitic nanoparticle is distributed along B-MWCNTs surfaces.

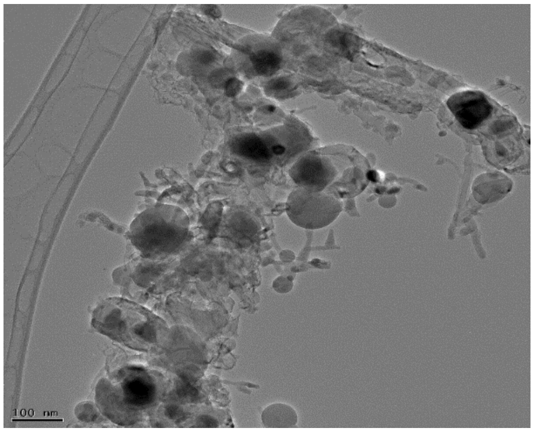

Figure 3.24 TEM images of B-MWCNT (TEB 2wt %)

In order to investigate the effect of concentration of doping material in B-MWCNTs synthesis on their electrochemical response, the electrochemical behaviour of 0.1- 1 mM $[Fe(CN)_6]^{3-/4-}$ in 1.0 M KCl at the B-MWCNTs electrode was examined by cyclic voltammetry (Figure 3.25a, 3.25c, 3.25e). The calibration curves are shown in Figures 3.25b, 3.25d, and 3.25f. The electrochemical sensing parameters estimated using B-MWCNTs electrodes are summarised in Table 3.10.

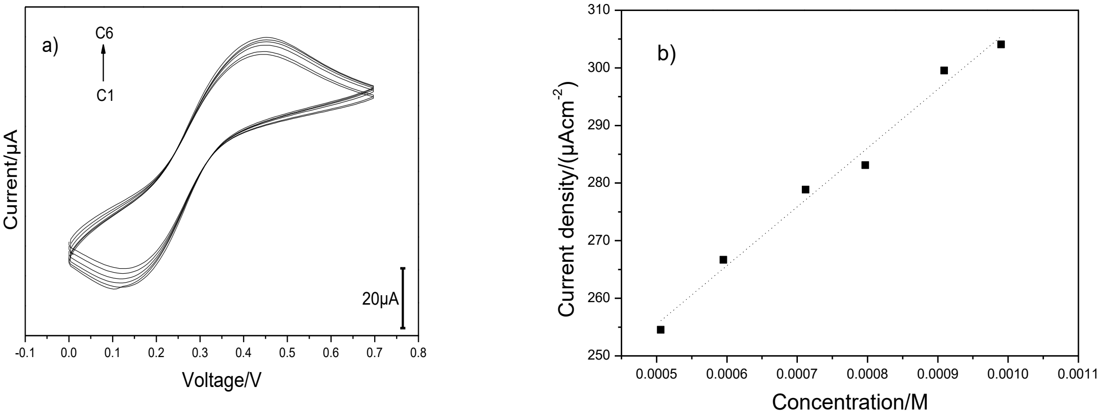

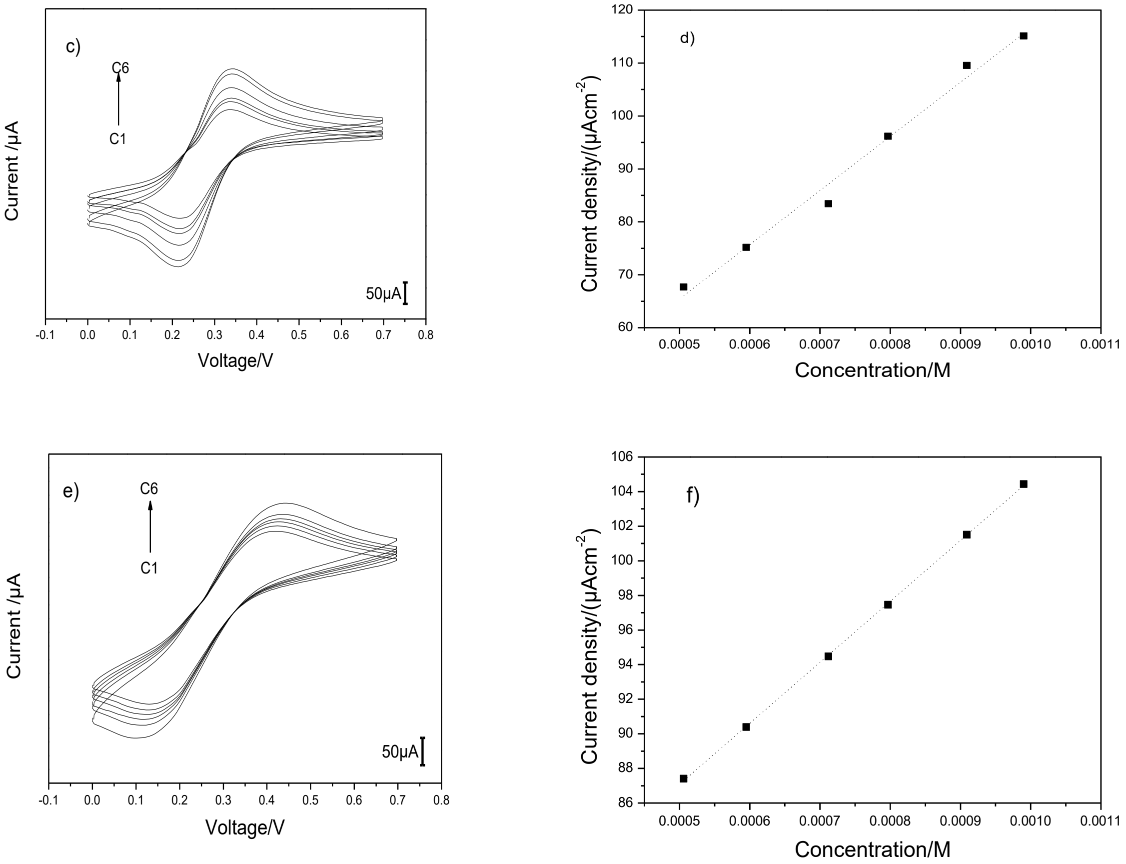

Figure 3.25 CVs and calibration curves recorded for 0.1-1 mM $[Fe(CN)_6]^{3-/4-}$ (1.0 M KCl) at scan rate of 0.02 V s^{-1} on a,b).B-MWCNT (0.5% TEB), c,d).B-MWCNT (2% TEB), e,f).B-MWCNT (3% TEB) (vs Ag/AgCl).

Compared to B-MWCNTs with 0.5 wt % and 3.0 wt % TEB, B-MWCNTs with 2 wt % TEB shows the lowest peak-to-peak separation (ΔE_p = 0.115 V). A large peak separation of B-MWCNTs electrodes (ΔE_p > 300 mV) indicates a high resistance and slow reaction kinetics on these particular electrodes. The different shapes of the cyclic voltammogram represent the different characteristics of linear diffusion domain on the electrode surface [174]. The detection limit of B-MWCNTs was slightly changed with the variation of doping concentration (0.5-3.0 wt % TEB). The variation of doping concentration (0.5-3.0 wt % TEB) in B-MWCNTs synthesis from propanone-ferrocene mixture does not significantly affect the sensitivity of B-MWCNTs electrodes. The variation of doping concentration (0.5-3.0 wt % TEB) in B-MWCNTs synthesis significantly affects the kinetic of electron transfer and the diffusion process in on electrode surface.

Table 3.10 The comparison of electrochemical properties for B-MWCNTs with different doping source concentrations (0.5-3.0% TEB)

Films	ΔE_p/(V)	Sensitivity/ (A $mM^{-1}cm^{-2}$)	LOD/(μM)
B-MWCNTs, $FeCp_2$/TEB (2:0.5)	0.302	102.6	103.5
B-MWCNTs, $FeCp_2$/TEB (2:2)	0.115	102.3	110.7
B-MWCNTs, $FeCp_2$/TEB (2:3)	0.298	102.1	92.1

The effects of the doping concentration in B-MWCNTs synthesis on the electron transport features were investigated with 0.5 mM $[Fe(CN)_6]^{3-/4-}$ in 1.0 M KCl using EIS in the frequency range of 0.1 Hz-100 KHz. Figure 3.26 displays the Nyquist plots of impedance spectroscopy for different B-MWCNTs electrodes. A diffusion in the porous electrode with the particle in different sizes was considered in the fitting process [173]. The electrochemical properties of B-MWCNTs electrodes extracted from fitting process are summarized in Table 3.11

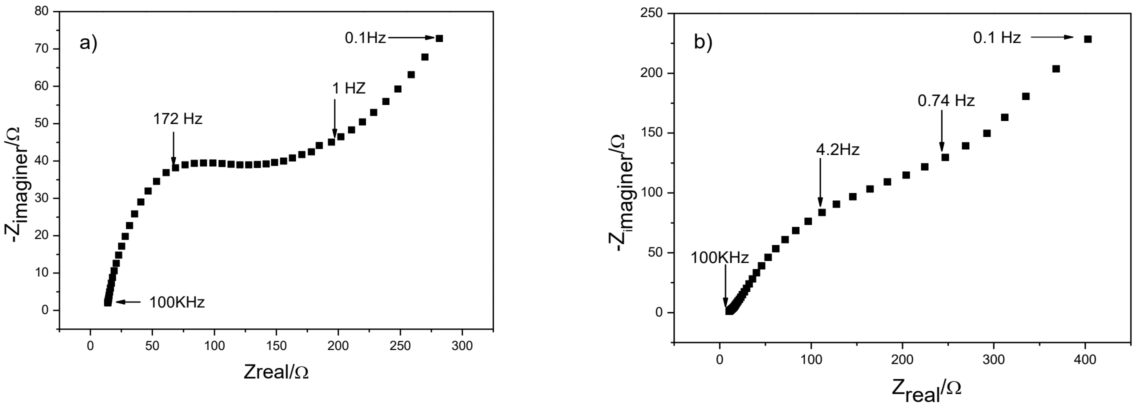

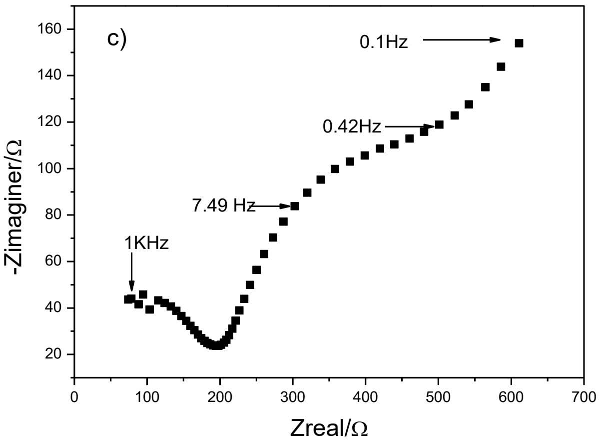

Figure 3.26 EIS recorded for 0.5 mM $[Fe(CN)_6]^{3-/4-}$ (1.0 M KCl) on a).B-MWCNT (0.5% TEB), b).B-MWCNT (2% TEB) c).B-MWCNT (3% TEB).

The EIS results reveal that the charge transfer resistance of B-MWCNTs differs significantly depending on the boron source concentration. The difference in the low-frequency arc characteristics of B-MWCNTs indicates the specific diffusion process for each electrode. Double layer capacitance decreases with the increase of triethyl borate concentration. The capacitance of carbon nanotube reflects its active surface area. The capacitance also increases with the increase of its surface area.

Table 3.11 Impedance data obtained for B-MWCNTs with different boron precursors concentration.

Films	$R_{ct}/(\Omega\ cm^{-2})$	C_{dl} /(μF)
B-MWCNTs, $FeCp_2$/TEB (2:0.5)	99.9	5.8
B-MWCNTs, $FeCp_2$/TEB (2:2)	19.4	2.1
B-MWCNTs, $FeCp_2$/TEB (2:3)	125.7	0.08

3.3. Phosphorus doped MWCNTs

3.3.1. Electrochemical characteristics of P-MWCNTs.

Typical SEM micrographs of P-MWCNTs produced by the decomposition of ethanol and triphenyl phosphine in the presence of ferrocene catalyst (triphenyl phosphine/ferrocene 1:1) are shown in Figure 3.27a. HCl treated P-MWCNTs are displayed in Figure 3.27b. The SEM micrographs taken for P-MWCNTs reveals that sole long nanotube and carbon clusters are grown on Si/SiO_2 substrate. The HCl treatment of P-MWCNTs films removes some part of the carbon cluster on the P-MWCNTs surface.

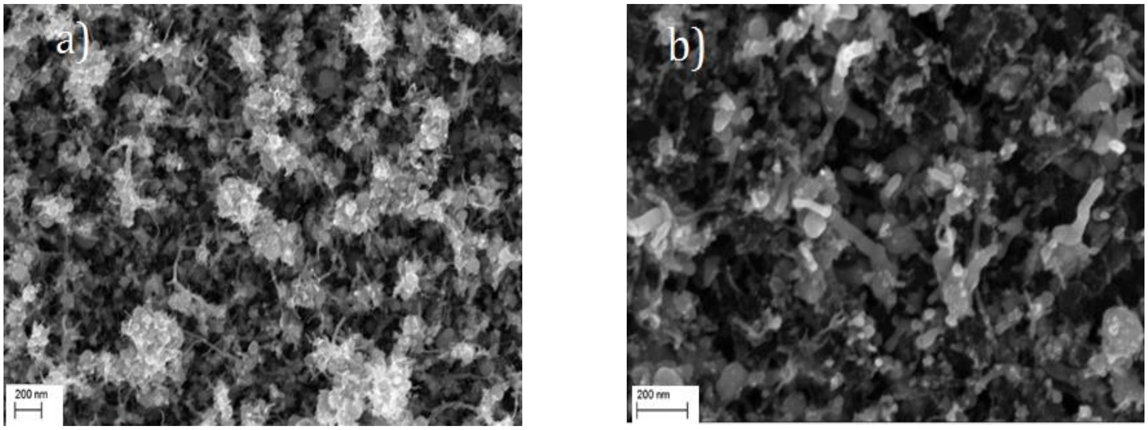

Figure 3.27 SEM images of a). P-MWCNTs, b). P-MWCNTs + HCl

Figure 3.28 shows the oxidation of P-MWCNTs from the ethanol carbon source with sulphuric acid/hydrogen peroxide mixture (piranha). The SEM micrograph reveals that the nanotube structure in P-MWCNTs was completely eliminated after the oxidation process. A dense carbon film was observed on Si/SiO_2 substrate.

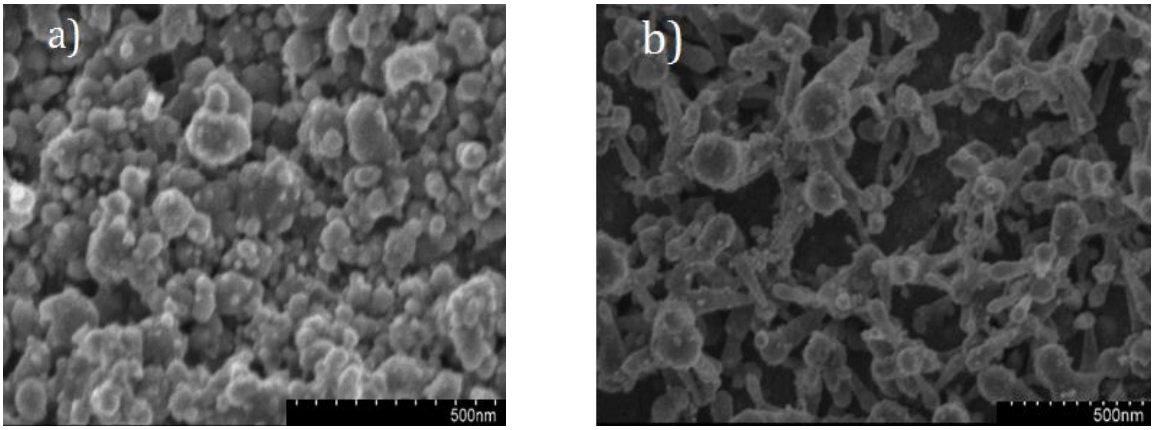

Figure 3.28 SEM images of P-MWCNTs a).Piranha oxidation, b).Decorated with AuNPs

Figure 3.28 b shows SEM micrographs of P-MWCNTs decorated with gold nanoparticles. The SEM images reveal that the gold nanoparticles were distributed homogenously onto the surface of P-MWCNTs so that no agglomeration of the nanoparticle occurs. The nanoparticle can be recognised as the small bright dots on the P-MWCNTs surfaces.

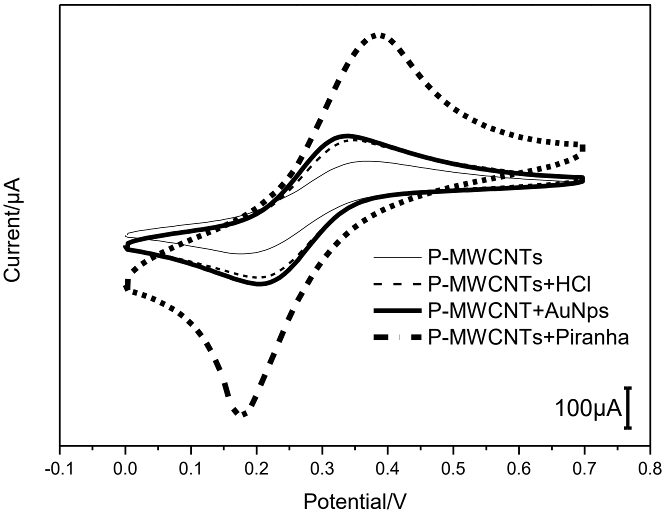

Figure 3.29 CVs recorded for 0.5 mM $[Fe(CN)_6]^{3-/4-}$ (1.0 M KCl) at the scan rate of 0.02 V s^{-1} on different P-MWCNTs electrodes (vs Ag/AgCl).

Figure 3.29 shows the cyclic voltammograms obtained over a range of 0 to 0.7 V for P-MWCNTs with HCl treatment, oxidative functionalisation with sulfuric acid/hydrogen peroxide mixture, and nanoparticle functionalisation with gold. A summary of the cyclic voltammetry data obtained for $[Fe(CN)_6]^{3-/4-}$ on P-MWCNTs before as well as after their treatment and functionalization are presented in Table 3.12.

The results show that an acid treatment with HCl and nanoparticle functionalisation with gold, significantly decreases the ΔE_p of P-MWCNTs, whereas oxidative functionalisation leads to increase the ΔE_p of P-MWCNTs. Corresponding to the SEM data, the above results illustrate that the ΔE_p of P- MWCNTs is highly sensitive to surface structure. It can be seen that the surface functionalisation of P-MWCNTs with AuNPs shows the lowest ΔE_p (0.126 V).

According to the theory, ΔE_p directly corresponds with the heterogenous electron transfer kinetics. A smaller ΔE_p indicates higher heterogenous electron transfer kinetics [147]. P-MWCNTs modified with AuNPs demonstrate faster kinetics toward the $[Fe(CN)_6]^{3-/4-}$ redox system than the oxidative functionalisation of P-MWCNTs and HCl treatment of P-MWCNTs. The decrease of ΔE_p observed for the surface treated P-MWCNTs electrodes with HCl and AuNPs indicates electrocatalytic effects due to the increase of surface chemistry area available to electroactive species. The increase of the ΔE_p of P-MWCNTs after oxidation with the piranha solution is connected to the damage of the nanotube structure on the P-MWCNTs films. The damage of the nanotube structure on the P-MWCNTs film leads to a decrease in the electrode active surface area. A higher current-concentration response in the cyclic voltammetry of P-MWCNTs after oxidation corresponds with the formation of dense film P-MWCNTs after oxidation.

CVs recorded for 0.1-1mM $[Fe(CN)_6]^{3-/4-}$ (1.0 M KCl) standard redox system at P-MWCNTS, P-MWCNTs/HCl, P-MWCNTs/piranha, P-MWCNTs/AuNPs are shown in Figure 3.30 a, Figure 3.30c, Figure 3.30d, and Figure 3.30f, respectively. The calibration curves in Figure 3.30 b, Figure 3.30d, Figure 3.30e, and Figure 3.30 g show the linear relationship between the current and concentration and following the Randles-Sevcik equation. The sensing parameters estimated for $[Fe(CN)_6]^{3-/4-}$ on P-MWCNTs electrodes in Figure 3.30 are summarised in Table 3.10.

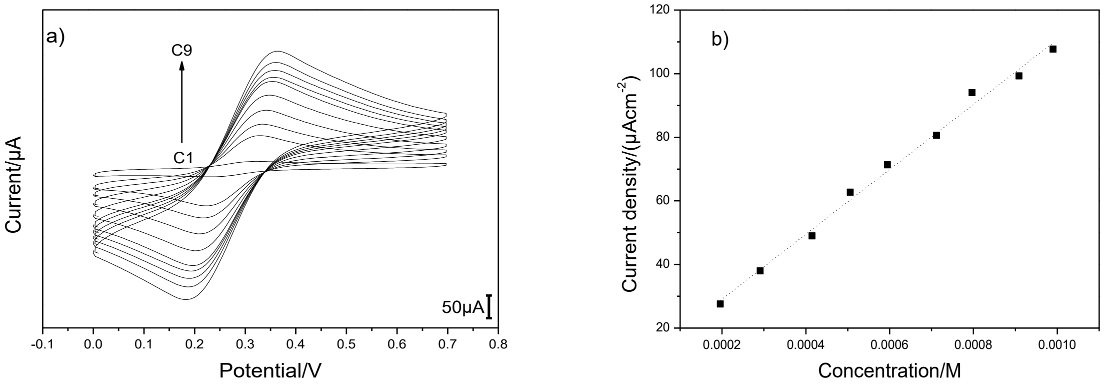

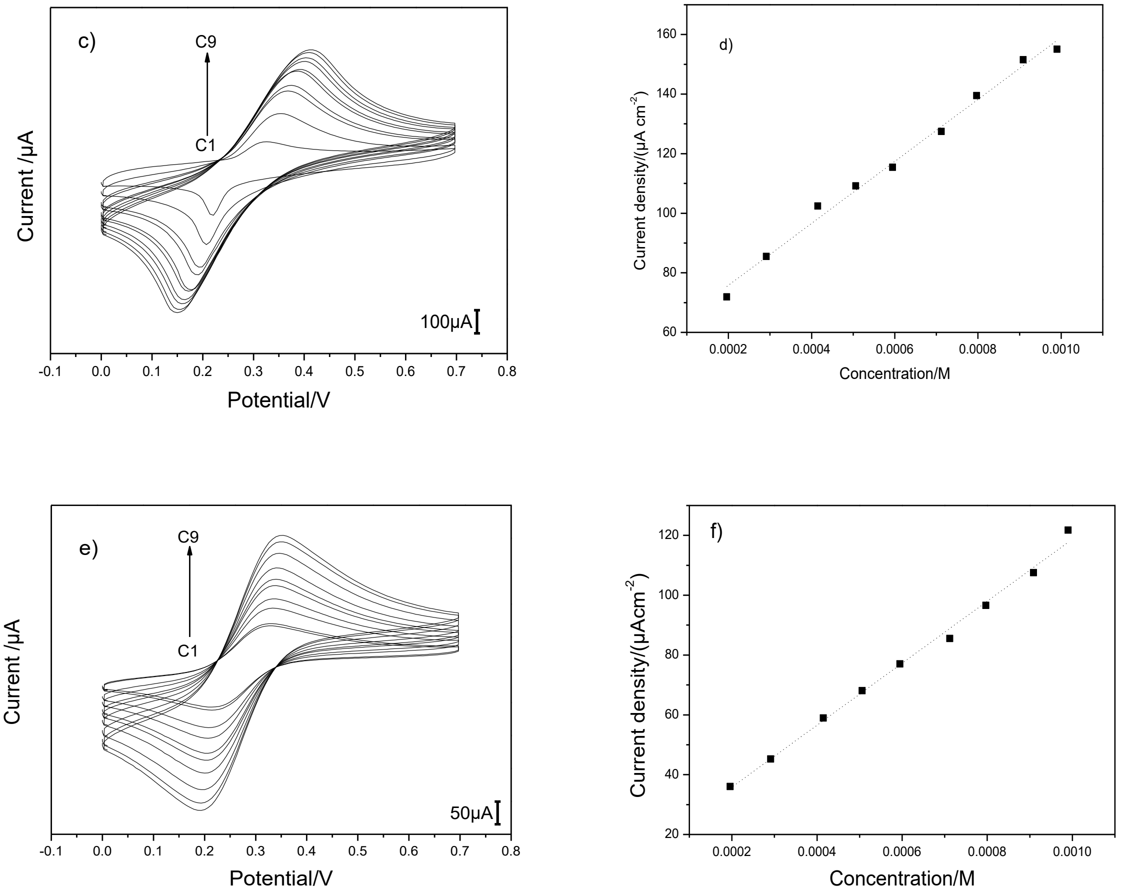

Figure 3.30 CVs and calibration curves recorded for 0.1-1 mM $[Fe(CN)_6]^{3-/4-}$ (1.0 M KCl) at scan rate of 0.02 V s^{-1} on a,b).P-MWCNTs/HCl, c,d).P-MWCNTs/piranha e,f).P-MWCNTs+ AuNPs (vs Ag/AgCl).

Surface treatment of P-MWCNTs with HCl and modification with AuNPs does not significantly change the sensitivity of P-MWCNTs. The oxidative functionalisation only slightly increases the sensitivity of P-MWCNTs. The increase of P-MWCNTs sensitivity after oxidative functionalisation can be explained by the reduction of the film porosity and the dense film formation as it can be seen from SEM micrographs as shown in Figure 3.28a. An increase in the film conductivity increases the current-concentration response of the electrodes.

As shown in Table 3.12, it can be clearly seen that acid treatment with HCl, the oxidative functionalisation with sulfuric acid/hydrogen peroxide mixture, and the gold nanoparticle functionalisation slightly changes the detection limit of P-MWCNTs. Thus P-MWCNTs, modified with AuNPs, demonstrated a better detection ability than either HCl treated of P-MWCNTs or oxidative functionalisation of P-MWCNTS. The results indicate that P-MWCNTs modified with AuNPs have the lowest noise/sensitivity ratio compared to other electrodes.

Table 3.12 CV parameters obtained for P-MWCNTs and surface modified P-MWCNTs.

Films	ΔE_p/(V)	K_s/(cm s^{-1})	Sensitivity/ (A mM^{-1} cm^{-2})	LOD/(μM)
P-MWCNTs	0.199	2.7×10^{-4}	101.9	50.2
P-MWCNTs/HCl	0.135	6.2×10^{-4}	102.0	59.8
P-MWCNTs/Piranha	0.203	2.6×10^{-4}	104.1	66.2
P-MWCNTs/ AuNPs	0.126	7.1×10^{-4}	101.9	44.8

The EIS measurements were performed in order to obtain charge transfer resistance and capacitance double layer value for P-MWCNTs and surface modified P-MWCNTs. The impedance spectra were recorded with 0.5 mM $[Fe(CN)_6]^{3-/4-}$ in 1.0 M KCl in the range of 0.1 Hz-100 KHz frequency range. The impedance spectra of the P-MWCNTs and the surface modified P-MWCNTs are displayed in Figure 3.31 as Nyquist plots. The complex plane of Nyquist plots consists of semi circles at high to medium frequencies and straight lines at low frequencies, representing the kinetic and diffusion process in the electrode, respectively. To analyses these experimental results, the Randles equivalent circuit was used to fit the impedance spectra. Table 3.13 displays the estimated EIS parameters obtained for P-MWCNTs and the surface modified P-MWCNTs.

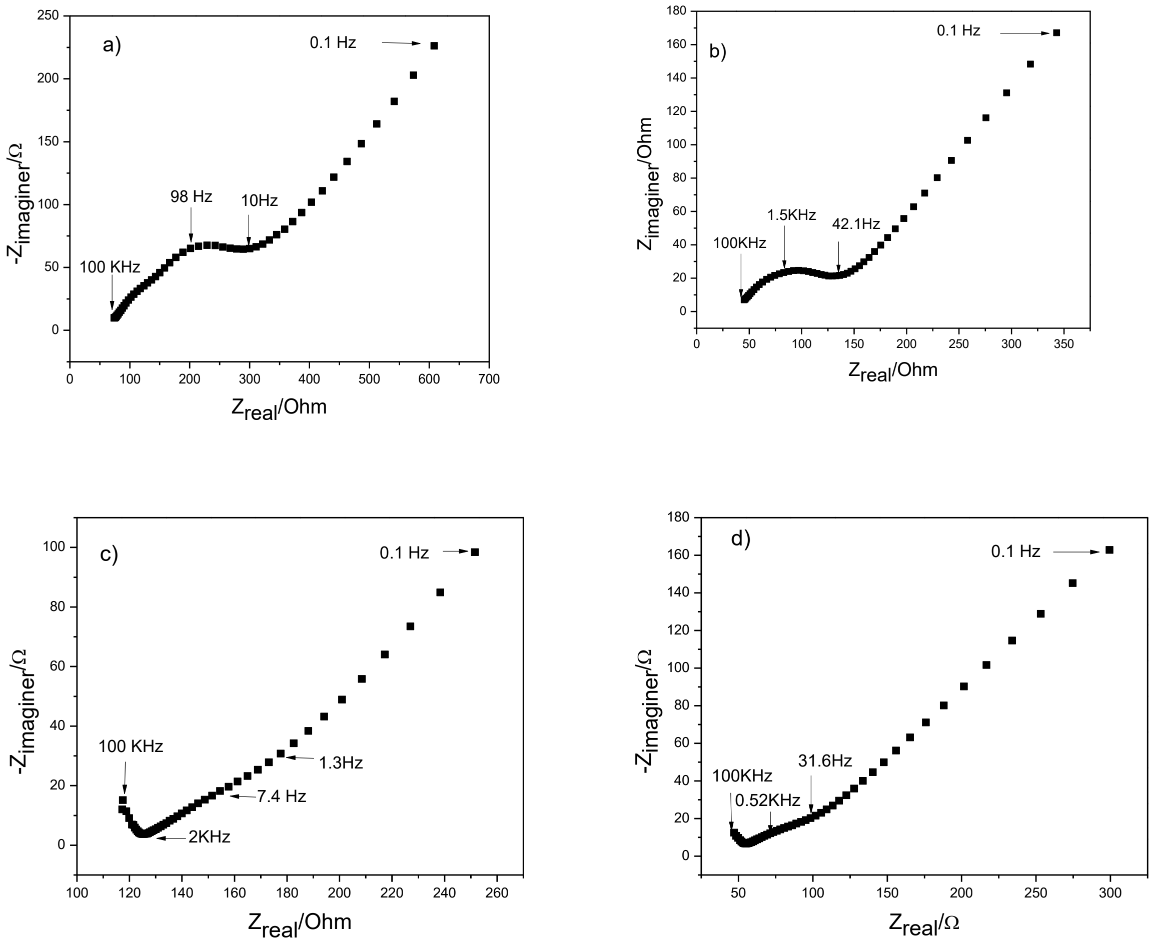

Figure 3.31 EIS recorded for 0.5 mM $[Fe(CN)_6]^{3-/4-}$(1.0 M KCl) On a).P-MWCNTs b).P-MWCNTs/HCl c).P-MWCNTs/piranha d).P-MWCNTs+ AuNPs.

The EIS spectra of all the P-MWCNTs electrodes show a different shape in high and low frequencies. The impedance spectroscopy analysis of P-MWCNTs revealed that the acid treatment with HCl, oxidative functionalisation with sulfuric acid/hydrogen peroxide mixture, and the gold nanoparticle functionalisation lead to significantly decreased of charge transfer resistance of P-MWCNTs. Thus, these experimental results reveal that the kinetic of P-MWCNTs is predominantly influenced by the morphology and surface chemistry within the material structure. The oxidative functionalisation of P-MWCNTs and the functionalisation of the P-MWCNTs with gold nanoparticle increase the C_{dl} of P-MWCNTs. The variation of C_{dl} value is connected with the change of the surface chemistry of nanotubes and the variation of the active surface area of the electrode.

Table 3.13 Estimated EIS parameters for P-MWCNTs and surface modified P-MWCNTs

Films	$R_{ct}/(\Omega\ cm^{-2})$	$C_{dl}/(\mu F)$
P-MWCNTs	155.3	3.3
P-MWCNTs/HCl	69.6	1.4
P-MWCNTs/Piranha	21.5	8.1
P-MWCNTs/ AuNPs	32.9	8.1

3.3.2. The effects of carbon sources on electrochemical characteristics of P-MWCNTs.

Typical SEM micrographs of P-MWCNTs produced by decomposition of cyclohexane or ethanol carbon sources with doping/catalyst ratio (triphenyl phosphine/ferrocene 1:1) are shown in Figure 3.32. The SEM micrographs of P-MWCNTs display that the P-MWCNTs from ethanol have a smaller diameter and are longer than the P-MWCNTs from cyclohexane. An agglomeration of carbon inclusions was found in all P-MWCNTs structures.

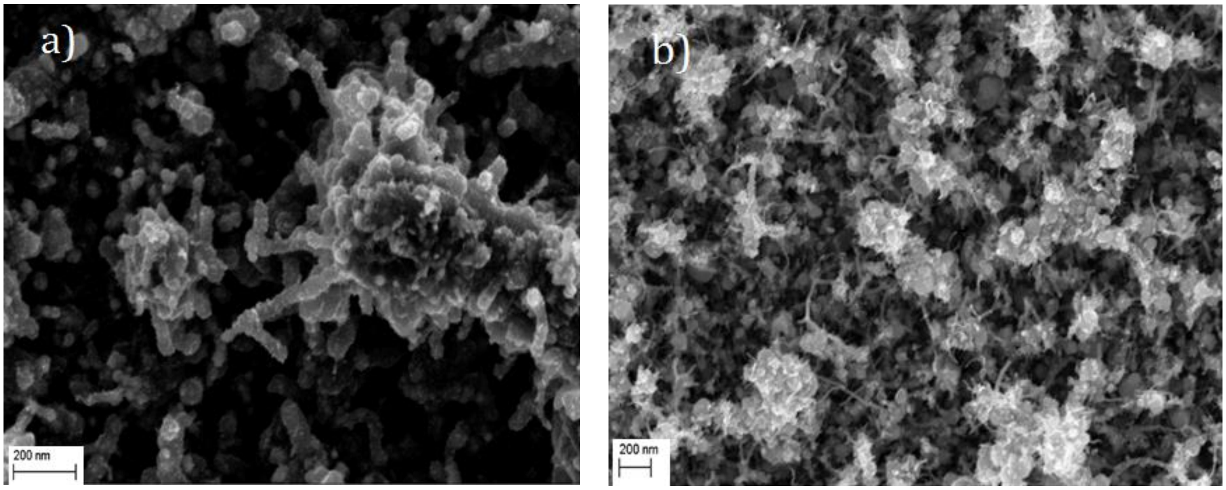

Figure 3.32 SEM images of P-MWCNTs from different carbon sources a).Cyclohexane, b).Ethanol

The TEM investigation reveals that onion-like carbon (OLC) is grown on Si/SiO_2 substrate as a reaction by-product of cyclohexane and triphenyl phosphine in the presence of ferrocene catalyst (Figure 3.33). The OLC consists of spherical structure that includes an iron closed carbon shell. Iron nanoparticles are encapsulated inside the OLC structure. The OLC possess smaller size, compared to P-MWCNTs. The OLC structure covers all kinds of concentric shells from nested fullerene to small polyhedral structure (<100 nm) [175].

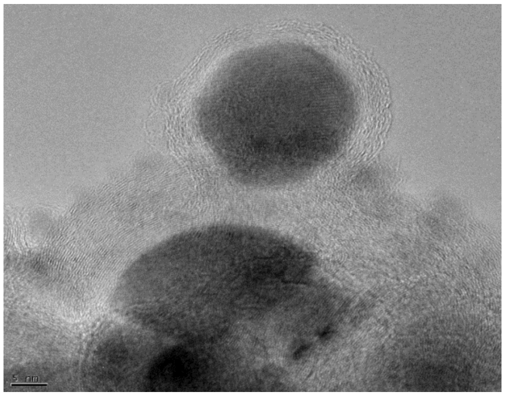

Figure 3.33 TEM images of onion-like carbon on P-MWCNTs surface.

To investigate the influence of carbon sources on the electrochemistry of P-MWCNTs, Cyclic voltammetry and electrochemical impedance spectroscopy were used to charaterise the P-MWCNTs electrode. Cyclic voltammetry responses of 0.5 mM $[Fe(CN)_6]^{3-/4-}$ (1.0 M KCl) at P-MWCNTs produced from different carbon sources are shown in Figure 3.34

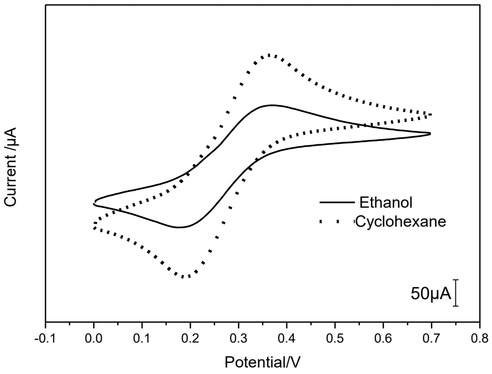

Figure 3.34 CVs recorded for 0.5 mM $[Fe(CN)_6]^{3-/4-}$ (1.0 M KCl) at a scan rate of 0.02 V s^{-1} on P-MWCNTs synthesis from different carbon sources (ethanol and cyclohexane) (vs Ag/AgCl).

The ΔE_p apparent of P-MWCNTs film fabricated by ethanol decomposition is very close to the ΔE_p of P-MWCNTs film fabricated by cyclohexane decomposition. It can be seen that the ΔE_p of P-MWCNTs electrodes from ethanol is 0.199 V, whereas the ΔE_p of P- MWCNTs electrodes from cyclohexane is 0.182 V. The electrode kinetic of P-MWCNTs from cyclohexane was slightly faster than that of the P-MWCNTs from ethanol. These results illustrate the interdependence of the electrode kinetic and the electrode structure in P-

MWCNTs. Nanotubes diameter, nanotubes agglomeration and the presence of onion-like carbon contribute to the variation of the ΔE_p of P- MWCNTs.

The impedance feature of the P-MWCNTs from ethanol and cyclohexane carbon sources at 0.5 mM $[Fe(CN)_6]^{3-/4-}$ in 1.0 M KCl were investigated by using EIS in the range of 0.1 Hz - 100 KHz and is shown in Figure 3.35. The estimated of EIS parameters are presented in Table 3.14.

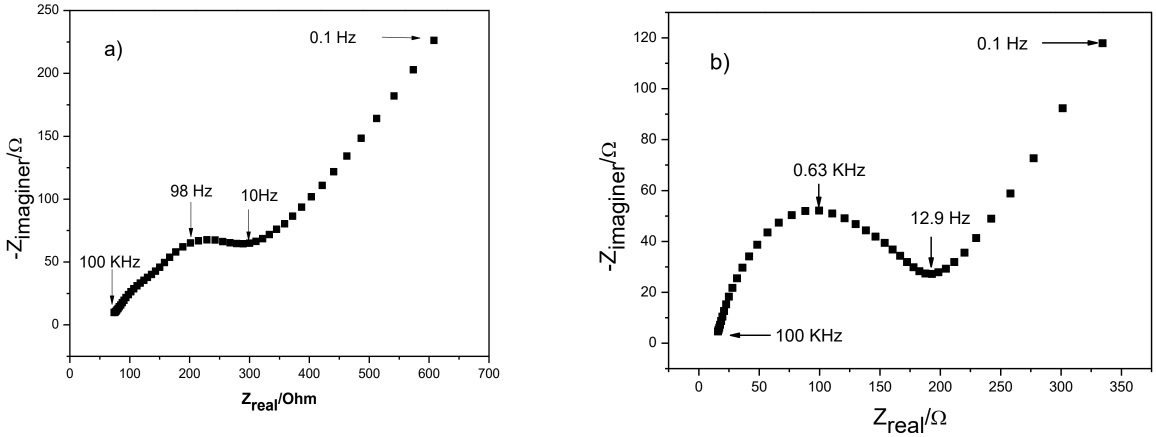

Figure 3.35 EIS recorded for 0.5 mM $[Fe(CN)_6]^{3-/4-}$ (1.0 M KCl) standard redox system at 0.02 V s^{-1} on P-MWCNTs from different carbon sources a).P-MWCNTs produced from ethanol b). P-MWCNTs produced from cyclohexane.

The quantitative analysis result of Fig 3.35. shows that the charge transfer resistance of the P-MWCNTs/EtOH is higher than of the P-MWCNTs/ CyH. The charge transfer resistance values agree with the cyclic voltammetry results, indicating that the P-MWCNTs/ CyH has faster electrodes kinetic compared to the P-MWCNTs/EtOH.

Table 3. 14 Estimated EIS and CV parameters for P-MWCNTs from ethanol and cyclohexane carbon sources

Films	ΔE_p/(V)	K_s/(cm s^{-1})	R_{ct}/ (Ω cm^{-2})	C_{dl}/ (μF)	Sensitivity/ (A mM^{-1} cm^{-2})	LOD/ (μM)
P-MWCNTs (Ethanol)	0.199	2.7 x 10^{-4}	155.3	3.3	101.9	50.2
P-MWCNTs (Cyclohexane)	0.182	3.3 x 10^{-4}	134.8	1.0	102.0	68.6

3.3.3. The effects of Doping/catalyst ratio on the electrochemical characteristics of P-MWCNTs.

SEM and TEM micrographs of various fabricated P-MWCNTs are presented in Figure 3.36 and 3.37 respectively. P-MWCNTs were grown on Si/SiO_2 substrate with cyclohexane and triphenyl phosphine pyrolysis in the presence of ferrocene catalyst by catalytic chemical vapor deposition. Both TEM and SEM images displayed that the P-MWCNTs structure was strongly affected by catalyst/doping ratio. In high catalyst/doping ratio sole and long carbon nanotubes can be clearly recognised, whereas, in a low catalyst/doping ratio, a large number of nanotubes clusters can be detected.

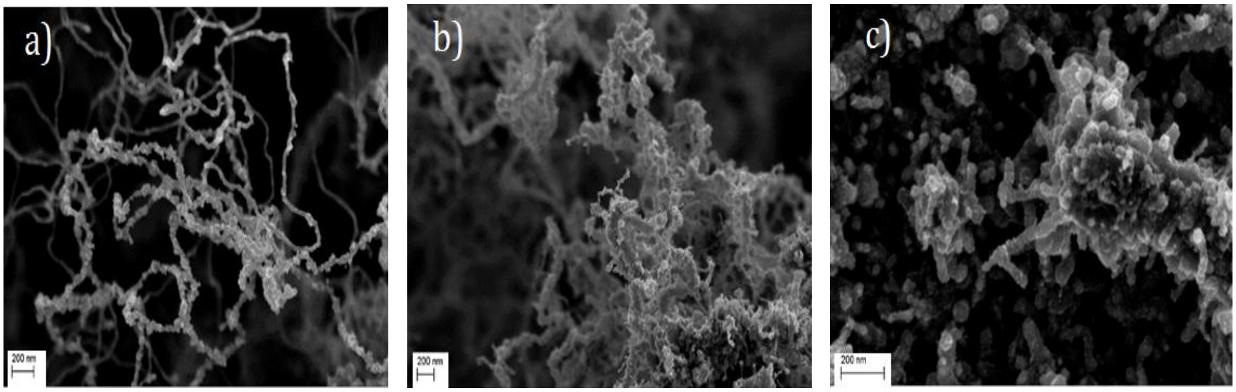

Figure 3.36 SEM images of P-MWCNTs a). $FeCp_2$/TPP (5:2 wt %), b). $FeCp_2$/TPP (2:1 wt %), c). $FeCp_2$/TPP (2:2 wt %).

The TEM revealed onion-like carbon structures that are recognised as the by-products of nanotubes synthesis. Encapsulated iron nanoparticles can be seen both in the CNTs structure and the onion-like carbons. This implies that iron may play an important role in the formation of both the OLC and the P-MWCNTs. It can be concluded that the higher the catalyst/TPP ratio, the longer the P-MWCNTs structure. Triphenyl phosphine/ferocenne in a high ratio, inhibits the growth of P-MWCNT. The formation of onion-like carbon is preferred than P-MWCNTs in the high ratio of Triphenyl phosphine/ferocenne.

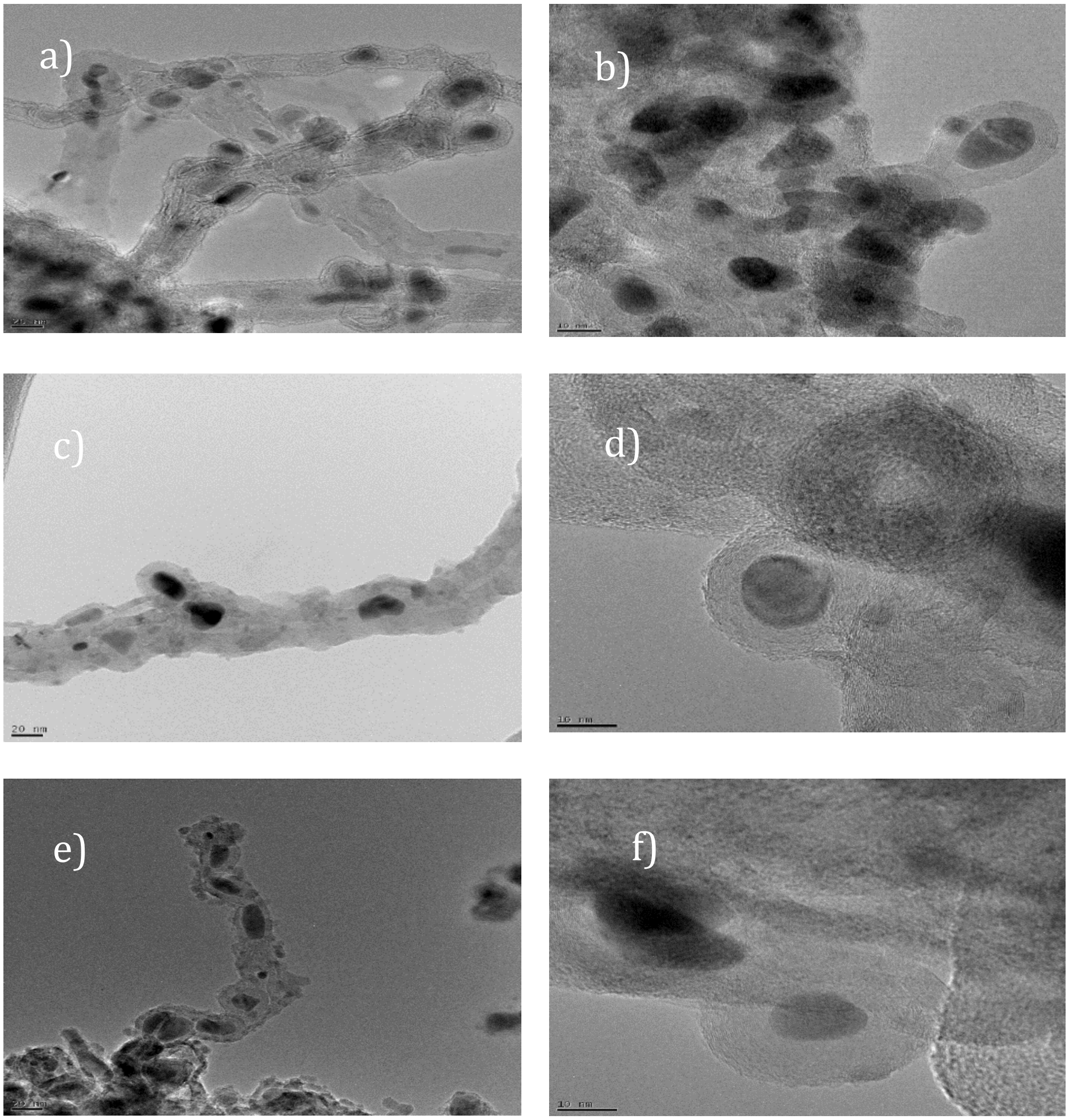

Figure 3.37 TEM images of P-MWCNTs a,b). $FeCp_2$/TPP (5:2 wt % %), c,d). $FeCp_2$/TPP (2:1 wt %), e,f). $FeCp_2$/TPP (2:2 wt %).

To investigates the influence of catalyst doping/doping ratio on electrochemical properties of P-MWCNTS, the electrochemical behaviour of 0.1- 1 mM $[Fe(CN)_6]^{3-/4-}$ in 1.0 M KCl on the P-MWCNTS film was examined by means of cyclic voltammetry. The effects of catalyst doping/doping ratio on CVs of P-MWCNTs are shown in Figure 3.38. The extracted CV parameters are reported in Table 3.15.

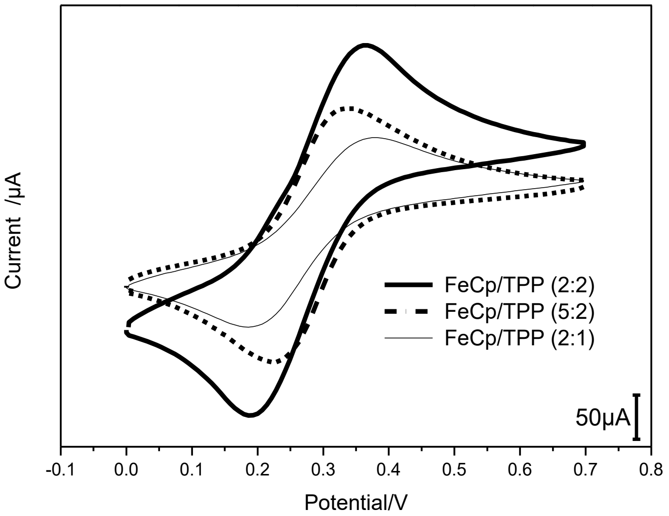

Figure 3.38 CVs recorded for 0.5mM $[Fe(CN)_6]^{3-/4-}$ (1.0 M KCl) at scan rate of 0.02 V s^{-1} on P-MWCNTs with different catalyst/doping ratio a). $FeCp_2$/TPP (5:2 wt %), b). $FeCp_2$/TPP (2:2 wt %), c). $FeCp_2$/TPP (2:1 wt %) (vs Ag/AgCl).

It can be seen that the P-MWCNTs with $FeCp_2$/TPP (5:2 wt %) has a lower ΔE_p than the P-MWCNTs with $FeCp_2$/TPP (2:2 wt %) and P-MWCNTs with $FeCp_2$/TPP (2:1 wt %). The slight difference in the ΔE_p value was observed on the P-MWCNTs with $FeCp_2$/TPP (2:2 wt %) and the P-MWCNTs with $FeCp_2$/TPP (2:1 wt %). The heterogenous electron transport (K_s) deduced for P-MWCNTs, was estimated by using the Nicholson equation[147]. The estimated K_s value of P-MWCNTs shows that the cluster of P-MWCNTs has lower electrodes kinetics compared to sole P-MWCNTs. The lower electrodes kinetics reflect low global coverage of edge plane sites [176]. The high current-concentration response of cluster P-MWCNTs is due to the low porosity and high density of the P-MWCNTs film. Similar results can be observed for P-MWCNTs produced from ethanol carbon precursor after piranha oxidation.

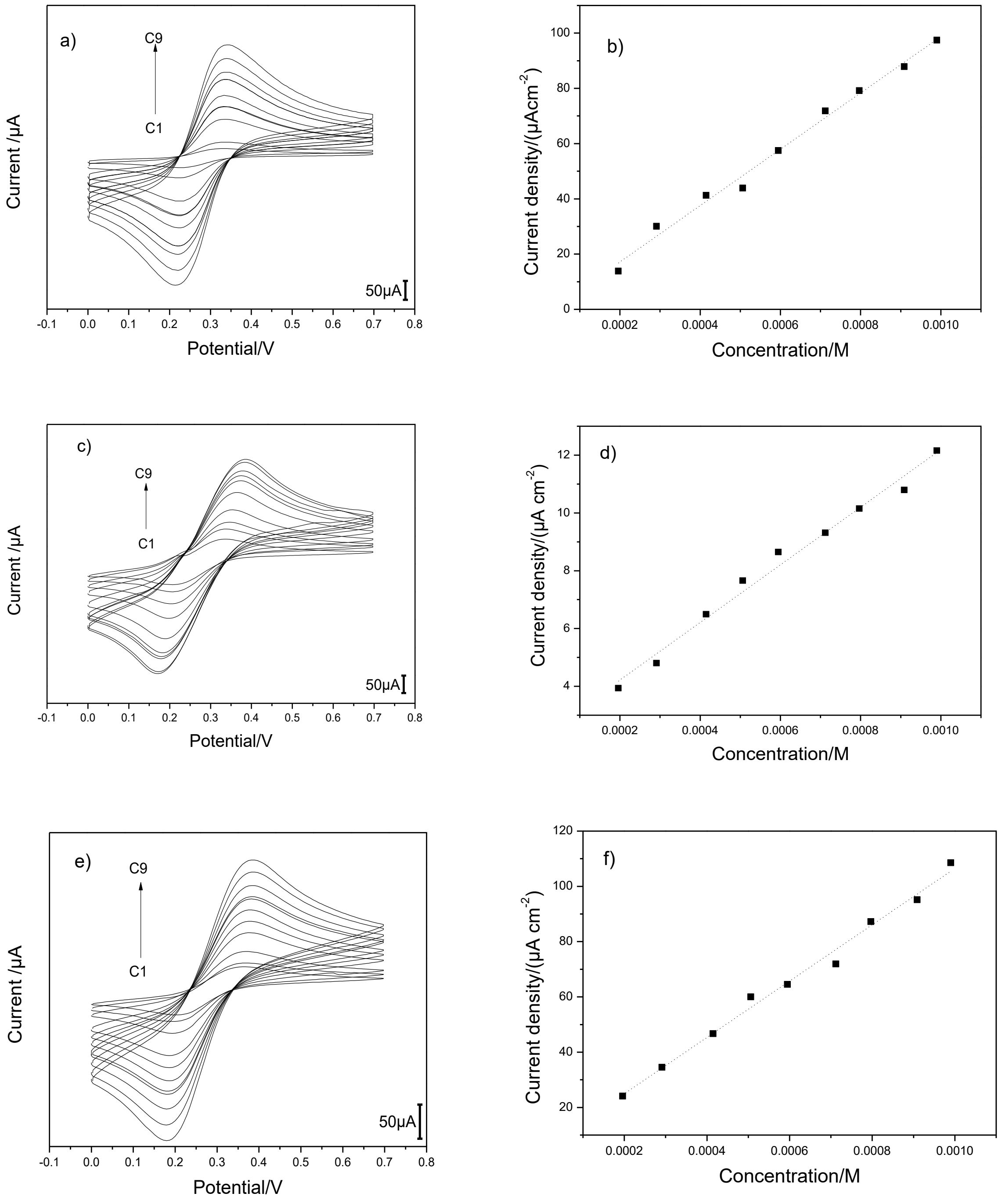

Figure 3.39 CVs and calibration curves recorded for 0.1-1 mM $[Fe(CN)_6]^{3-/4-}$ (1.0 M KCl) at scan rate of 0.02 V s^{-1} on P-MWCNTs with different doping/catalyst ratio a,b). $FeCp_2$/TPP (5:2 wt %), c,d). $FeCp_2$/TPP (2:2 wt %), e,f). $FeCp_2$/TPP (2:1 wt %) (vs Ag/AgCl).

Figures 3.39a, 3.39c, 3.39f, and 3.39b, 3.39d, and 3.39f show the cyclic voltammetry curves and the calibration curves of the P-MWCNTs with various $FeCp_2$/TPP ratio, respectively. Based on the signal-to-noise approach, from the linear concentration-current dependence curve, the detection limit and sensitivity values of P-MWCNTs with various $FeCp_2$/TPP were estimated [163]. The detection limit and sensitivity values estimated for the P-MWCNTs are summarized in Table 3.15.

The quantitative analysis of Figure 3.39 shows that the difference in the catalyst/doping ratio slightly affects the detection limit of P-MWCNTs toward $[Fe(CN)_6]^{3-/4-}$. The variation of catalyst/doping ratio (5:2, 2:2, 2:1wt %) in the P-MWCNTs does not significantly affect the sensitivity of the P-MWCNTs.

The electrochemical behavior of the redox system $[Fe(CN)_6]^{3-/4-}$ on the P-MWCNTs films with different catalyst doping ratios was investigated by means of the EIS technique. Figure 3.40 displays the impedance plots recorded in 0.1 Hz-100 KHz frequency range at the P-MWCNTs electrode in the presence of 0.5 mM $[Fe(CN)_6]^{3-/4-}$ in1.0 M KCl. The Randles equivalent circuit was used to interpret the experimental impedance spectra. The semicircle in high to medium frequency region of the Nyquist plot is connected to a kinetic of electrodes and the straight line at low frequency represents the diffusion process in the electrodes. The difference in the shape of the P-MWCNTs in high-frequency impedance is due to the variation of the kinetics of P-MWCNTs electrodes.

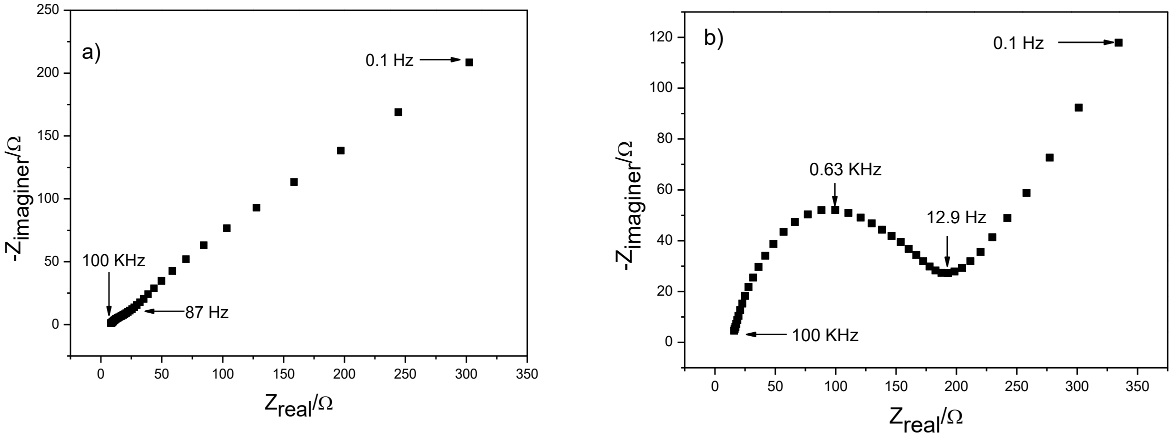

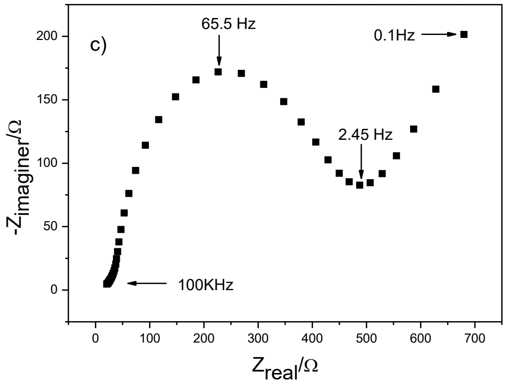

Figure 3.40 EIS recorded for 0.5 mM $[Fe(CN)_6]^{3-/4-}$ (1.0 M KCl) on P-MWCNTs with different doping/catalyst ratio a). $FeCp_2$/TPP (5:2 wt %), b). $FeCp_2$/TPP (2:2 wt %), c). $FeCp_2$/TPP (2:1 wt %)

P-MWCNTs with (5:2 wt %) $FeCp_2$/TPP exhibited a depressed semicircle with very small diameter in the high-frequency region and a straight line in the low-frequency region. The semicircle in high frequency was explained by means of the high ionic conductivity at the electrode/electrolyte interface [177]. The P-MWCNTs with (5:2 wt %) $FeCp_2$/TPP catalyst doping ratio shows lower charge transfer resistance than the P-MWCNTs with (2:2 wt %) $FeCp_2$/TPP and the P-MWCNTs with (2:1 wt %) $FeCp_2$/TPP. The results indicate that the P-MWCNTs with a long tubular structure exhibit faster electrodes kinetics compared to the P-MWCNTs clusters.

Table 3. 15 Estimated EIS and CV parameters for P-MWCNTs from various catalyst/doping ratios.

Films	ΔE_p/(V)	K_s/ (cm s^{-1})	R_{ct}/ (Ω cm^{-2})	Sensitivity/ (A mM^{-1} cm^{-2})	LOD/ (μM)
P-MWCNTs, $FeCp_2$/TPP (5:2)	122	$7.5x10^{-4}$	7.2	102.0	70.2
P-MWCNTs, $FeCp_2$/TPP (2:2)	182	$3.3x10^{-4}$	134.8	102.0	68.6
P-MWCNTs, $FeCp_2$/TPP (2:1)	180	$3.4x10^{-4}$	43.9	101.9	71.8

3.4. Electrochemical analysis of dopamine on B-MWCNTs and P-MWCNTs films

B-MWCNTs and P-MWCNTs are low-dimensional materials with large surface volume ratio. These materials demonstrate a good ability to mediate electron transfer with an electroactive material when used as an electrode. Since the surface of B-MWCNTs and P-MWCNTs contain great degree of defects in their basal plane and edge plane, it would be interesting to study the influence of production methods and surface modification on their electrochemical properties and analytical performance in biomolecule oxidation. Dopamine represents an important neurotransmitter that undergoes two electrons transport when oxidised into dopamine o-quinone (Figure 3.41). The cyclic voltammetry characteristic of dopamine is highly sensitive to the nature of carbon surfaces [178]. The oxidation of dopamine on CNTs can be investigated by means of cyclic voltammetry and impedance spectroscopy techniques [179].

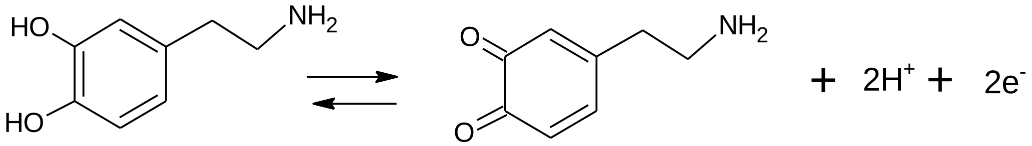

Figure 3.41 The oxidation of dopamine to dopamine quinone [136,180]

3.4.1 Electrochemical characteristics of B-MWCNTs

Cyclic voltammetry was used to study the electrochemistry of dopamine. Figure 3.40 shows the cyclic voltammogram of vertically aligned B-MWCNTs and Y-Shaped B-MWCNTs for 0.25mM dopamine in PBS (pH=7). The extracted CV parameters in Figure 3.42 are presented in Table 3.16.

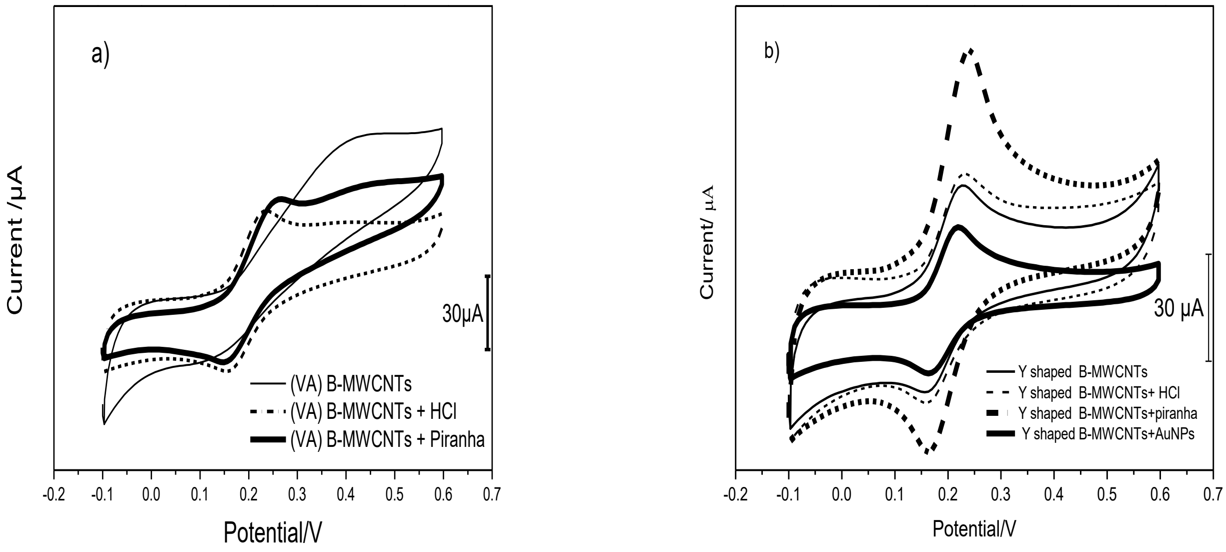

Figure 3.42 CVs recorded for 0.25 mM dopamine in PBS (pH=7) at scan rate of 0.02 V s^{-1} on a). vertically aligned B-MWCNTs, b).Y-shaped B-MWCNTs (vs Ag/AgCl).

The difference in the cyclic voltammetry current background of B-MWCNTs is due to the difference in the surface roughness of the electrode [181]. As shown in Table 3.16, the cyclic voltammogram reveals that the HCl treatment and oxidative functionalisation of vertically aligned B-MWCNTs lead to a decrease of the ΔE_p redox system. The ΔE_p of Y shaped B-MWCNTs does not significantly change after HCl treatment. The shift of ΔE_p that appeared in vertically aligned B-MWCNTs indicates that the enhancement of the electro catalytic effects corresponds with the increase of the active surface to the electroactive species. A higher proportion of edge plane sites and oxygen functional group contributed to the electrocatalytic activity of electrode [174,182].

HCl treatment of B-MWCNTs leads to the elimination of boron filling, as it can be seen in the XPS data. The consequence of boron elimination is the increase of defect density in the nanotubes structure. The change of the ΔE_p value of the vertically aligned B-MWCNTs and the Y-shaped B-MWCNTs after the HCl treatment illustrates the contribution of defect to the electrode kinetic toward dopamine/dopamine quinone redox system.

The decrease of ΔE_p relates to the increase of heterogeneous electron transport. The increase of heterogenous electron transfer of vertically aligned B-MWCNTs and Y-Shaped

B-MWCNTs film after oxidative functionalisation is due to the formation of the hydrogen bonding between the dopamine and the hydroxyl functional group in the B-MWCNTs and better hydrophilic interaction between electrode and solution [183,184].

In order to investigate further the electrochemical properties of dopamine on vertically aligned B-MWCNTs and Y-Shaped B-MWCNTs, the dependence of the current response on the concentration of dopamine was considered by varying the concentration of the electro active compound. Figure 3.40 shows the CVs observed for the oxidation of dopamine (0.1-0.5 mM) in PBS (pH=7) at various vertically aligned B-MWCNTs electrodes. The estimated CV parameters for dopamine on B-MWCNTs are presented in Table 3.16

The cyclic voltammetry results (Figure 3.43) reveals the linear relationship between the current and dopamine concentration. It can be clearly seen that the acid treatment with HCl, the oxidative functionalisation with piranha solution, and the gold nanoparticle functionalisation slightly changes the detection limit and sensitivity of the vertically aligned B-MWCNTs toward dopamine/dopamine quinone redox system. The variation of sensitivity is due to the difference in structure of the vertically aligned B-MWCNTs that probably plays a significant role in the mechanism of electrochemical oxidation of dopamine.

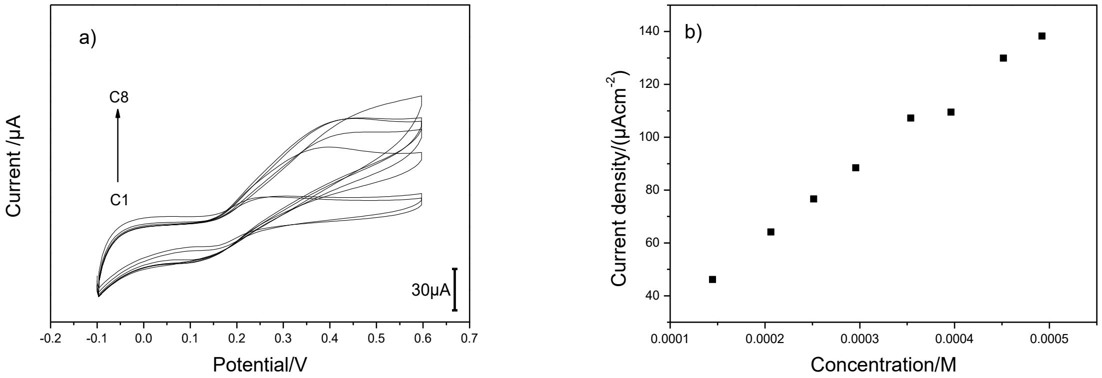

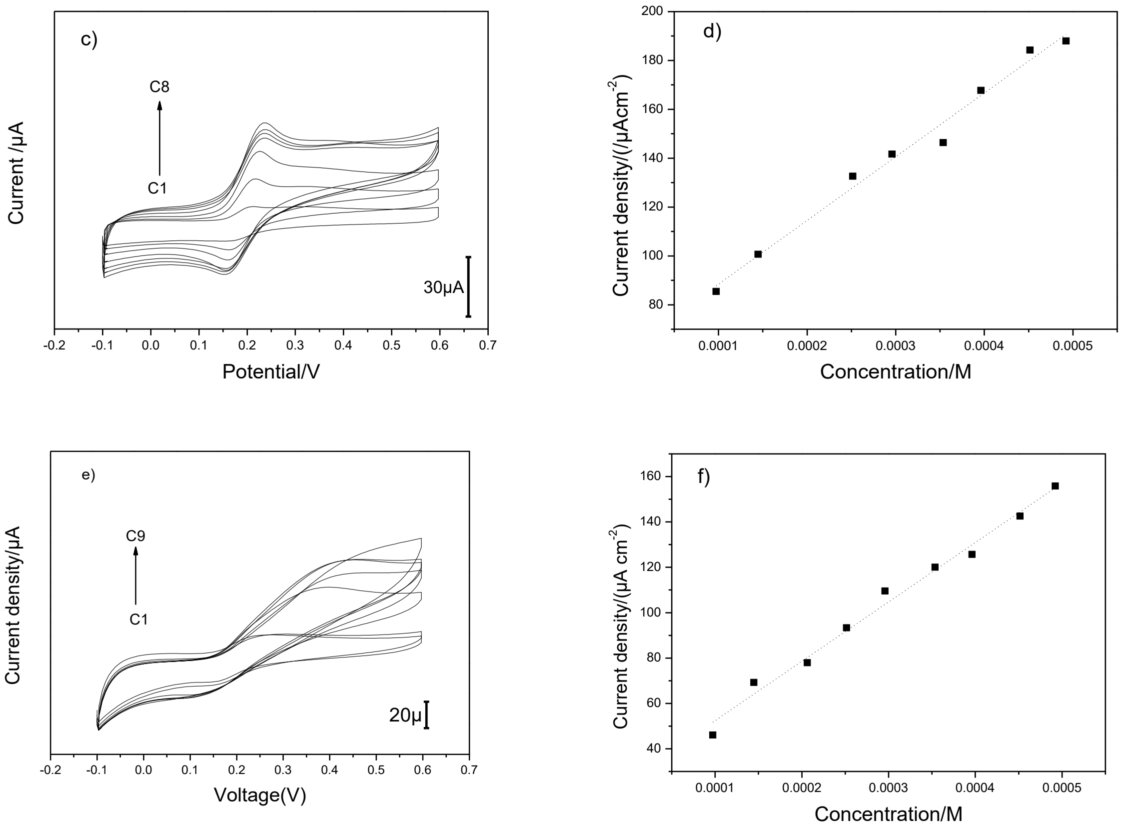

Figure 3.43 CVs and calibration curves obtained for dopamine 0.05-0.5 mM in PBS (pH=7) at scan rate of 0.02 V s^{-1} on a,b).vertically aligned B-MWCNTs, c,d).vertically aligned B-MWCNTs/HCl, e,f). vertically aligned B-MWCNTs/piranha (vs Ag/AgCl).

Figure 3.44 shows the electrochemical response of 0.1-0.5 mM dopamine in PBS (pH=7) at different Y-shaped B-MWCNTs electrodes. The calibration curve in Figure 3.42 displays the linear relationship between current and concentration that is shown by the Randles-Sevcik equation. The estimated CV parameters for various types of B-MWCNTs are presented in Table 3.16

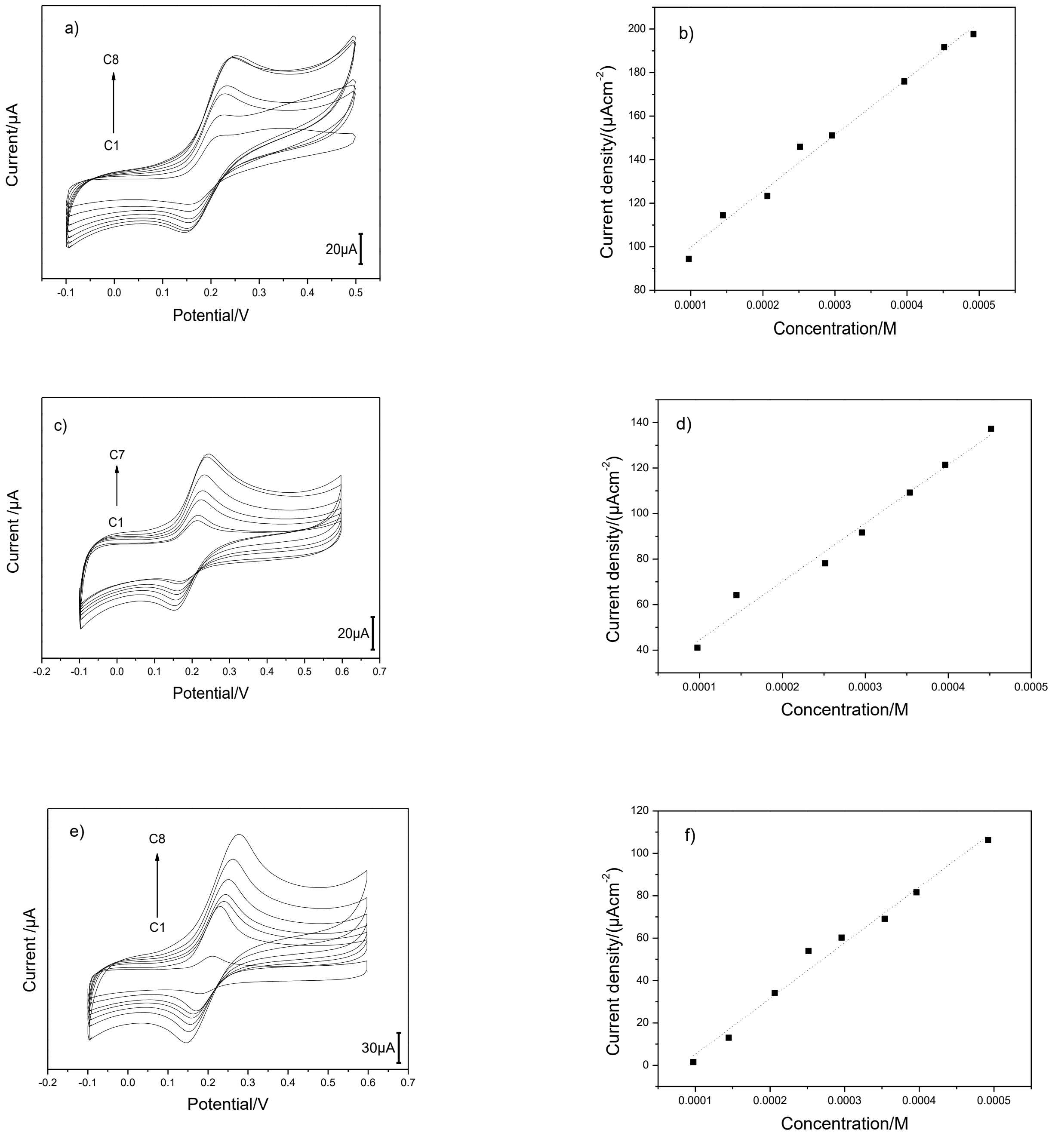
a)
C8
C1
Current/μA
20μA
-0.1
0.0
0.1
0.2
0.3
0.4
0.5
Potential/V
b)
Current density/(μAcm^{-2})
80
100
120
140
160
180
200
0.0001
0.0002
0.0003
0.0004
0.0005
Concentration/M
c)
C7
C1
Current /μA
20μA
-0.2
-0.1
0.0
0.1
0.2
0.3
0.4
0.5
0.6
0.7
Potential/V
d)
Current density/(μAcm^{-2})
40
60
80
100
120
140
0.0001
0.0002
0.0003
0.0004
0.0005
Concentration/M
e)
C8
C1
Current /μA
30μA
-0.2
-0.1
0.0
0.1
0.2
0.3
0.4
0.5
0.6
0.7
Potential/V
f)
Current density/(μAcm^{-2})
0
20
40
60
80
100
120
0.0001
0.0002
0.0003
0.0004
0.0005
Concentration/M

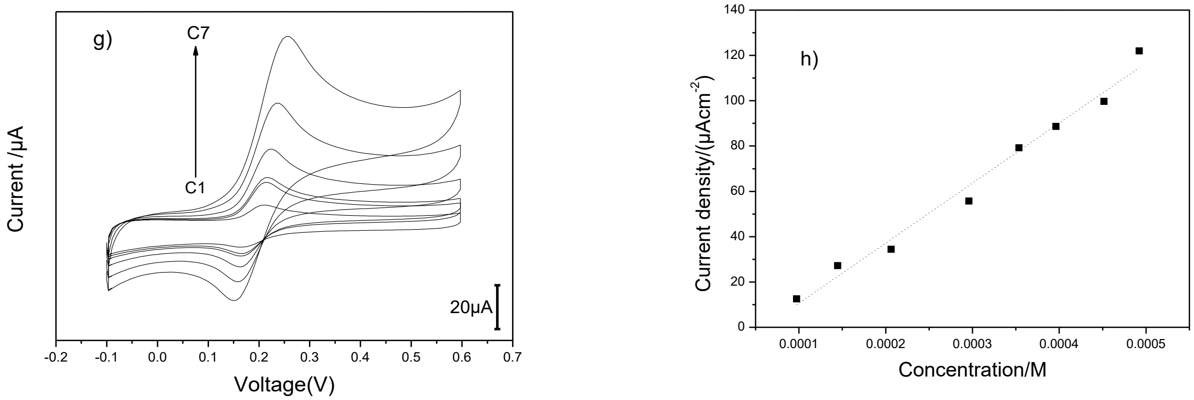

Figure 3.44 CVs and calibration curves obtained for dopamine 0.05-0.5 mM (vs Ag/AgCl) at scanrate of 0.02 V s^{-1} On a,b).Y-shaped B MWCNTs, c,d).Y-shaped B-MWCNTs/HCl, e,f) Y-shaped B-MWCNTs/piranha, g,h).Y-shaped B MWCNTs/piranha/ AuNPs (vs Ag/AgCl).

The quantitative analysis of Figure 3.44 in Table 3.16 shows that the sensitivity of the Y-shaped B-MWCNTs slightly increased after their oxidation and HCl treatment. Functionalisation with AuNPs does not significantly influence the sensitivity of the Y-shaped B-MWCNTs. Functionalisation of the Y-shaped B-MWCNTs with AuNPs improve the electrocatalytic activity of the Y-shaped B-MWCNTs. The increase of the Y-shaped B-MWCNTs sensitivity after oxidative functionalisation towards dopamine/dopamine o-quinone redox system is due to the porosity reduction and the formation of a dense film after the damage of the Y-shaped structure. A similar effect can be observed in the measurement of Y-shaped B-MWCNTs before and after the oxidative functionalisation towards $[Fe(CN)_6]^{3-/4-}$ redox system. A slight change in the detection limit of dopamine can be observed after the surface treatment of the Y-shaped B-MWCNTs with HCl, piranha solution as well as functionalisation with AuNPs.

Table 3.16 Estimated CV parameters for B-MWCNTs toward dopamine/dopamine quinone redox system

Films	ΔE_p/(V)	K_s/ (cm s^{-1})	Sensitivity/ (A mM^{-1} cm^{-2})	LOD/(μM)
Vertically aligned B-MWCNTs	0.181	4.8×10^{-4}	263.3	33.9
Vertically aligned B-MWCNTs /HCl	0.077	4.5×10^{-3}	260.7	48.1
Vertically aligned B-MWCNTs/Piranha	0.113	1.3×10^{-3}	261.7	40.6
Y-shaped B-MWCNTs	0.067	9.3×10^{-3}	258.0	41.9
Y-shaped B-MWCNTs/HCl	0.066	9.5×10^{-3}	256.7	55.4
Y-shaped B-MWCNTs/Piranha	0.077	4.5×10^{-3}	263.0	46.7
Y-shaped B-MWCNTs/ AuNPs	0.059	6.1×10^{-2}	258.0	42.9

3.3.2 Electrochemical characteristics of P-MWCNTs

The electrochemistry of dopamine at P-MWCNTs electrode was investigated by means of cyclic voltammetry. Figure 3.45 shows a typical cyclic voltammogram recorded on the different P-MWCNTs electrodes in the presence of 0.25 mM dopamine in PBS solution (pH=7) with at the scan rate of 0.02 V s^{-1}. The dopamine/dopamine quinone redox system sensing parameters, computed using different P-MWCNTs electrodes in Figure 3.45, are summarized in Table 3.17.

The ΔE_p value of P-MWCNTs toward dopamine/dopamine o-quinone redox system is 0.139 V, Whereas the ΔE_p value of the vertically aligned B-MWCNTs and Y-shaped B-MWCNTs is 0.181 V and 0.067 V respectively. These results indicate that the kinetic of Y-shaped B-MWCNTs is faster than that of vertically aligned B-MWCNTs and P-MWCNTs toward the dopamine/dopamine quinone redox system

The ΔE_p value of dopamine redox system on P-MWCNTs decreased after the HCl treatment, the oxidative functionalisation by piranha solution and the functionalisation by AuNPs. The change of the ΔE_p indicated a higher catalytical activity toward dopamine oxidation reduction on P-MWCNTs electrode after surface treatment.

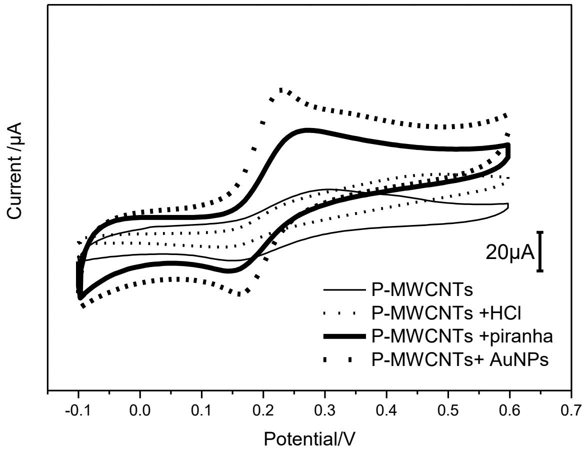

Figure 3.45 CVs recorded for 0.25 mM Dopamine in PBS (pH=7) at scan rate 0.02 V s^{-1} on different P-MWCNTs electrodes (vs Ag/AgCl)

Figure 3.46 displays the cyclic voltammograms of 0.1-0.5 mM dopamine in PBS (pH=7) at P-MWCNTs electrodes. Upon the addition of 0.05 mM, an enhancement of anodic peak current was observed. The oxidation peak currents were increased by increasing the dopamine concentration in the solution. The estimated CV parameters for the B-MWCNTs are presented in Table 3.17

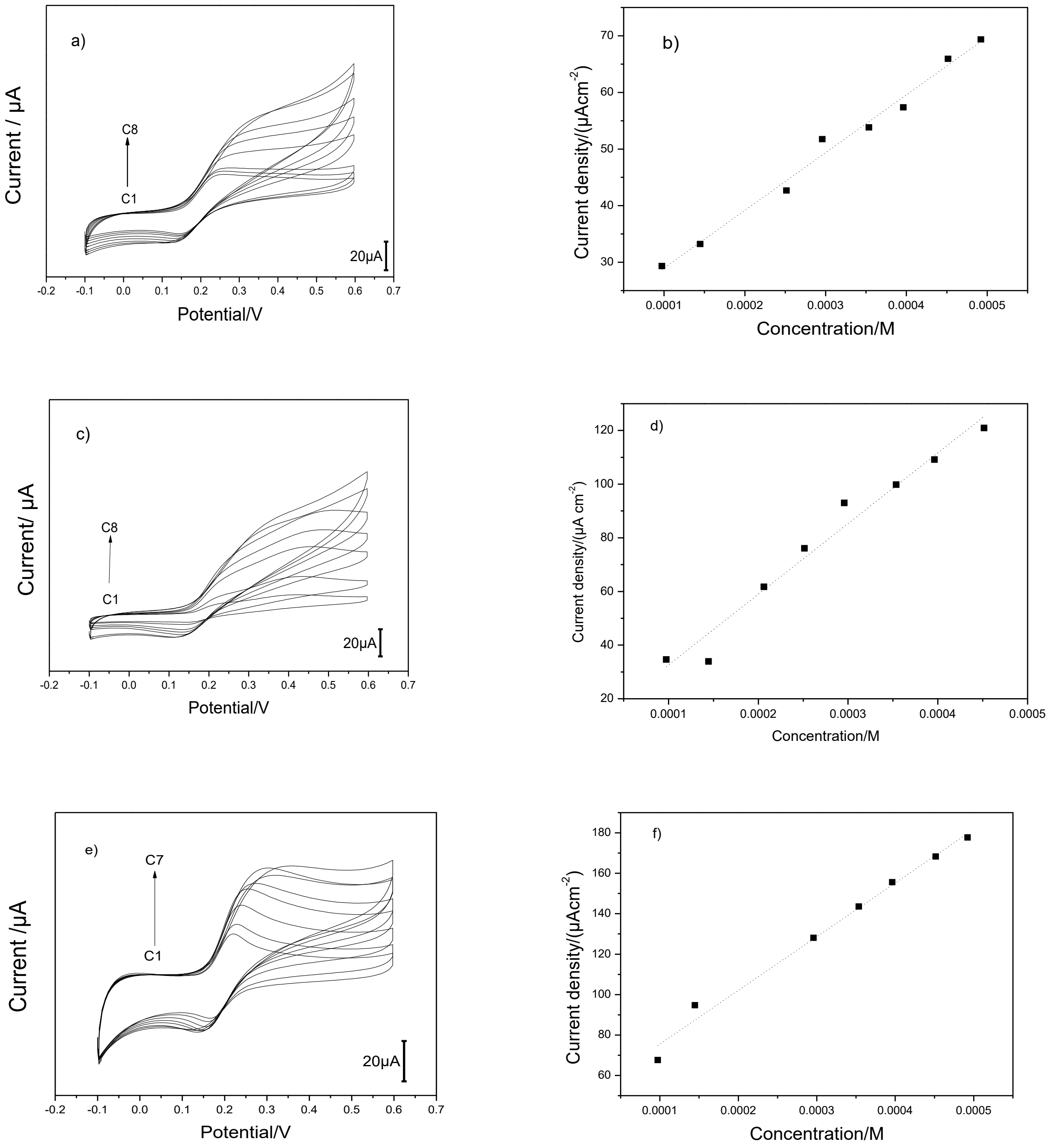
a)
C8
C1
20μA
Current / μA
Potential/V
-0.2
-0.1
0.0
0.1
0.2
0.3
0.4
0.5
0.6
0.7
b)
Current density/(μAcm^{-2})
Concentration/M
30
40
50
60
70
0.0001
0.0002
0.0003
0.0004
0.0005
c)
C8
C1
20μA
Current/ μA
Potential/V
d)
Current density/(μA cm^{-2})
Concentration/M
20
40
60
80
100
120
e)
C7
C1
20μA
Current /μA
Potential/V
f)
Current density/(μAcm^{-2})
Concentration/M
60
80
100
120
140
160
180

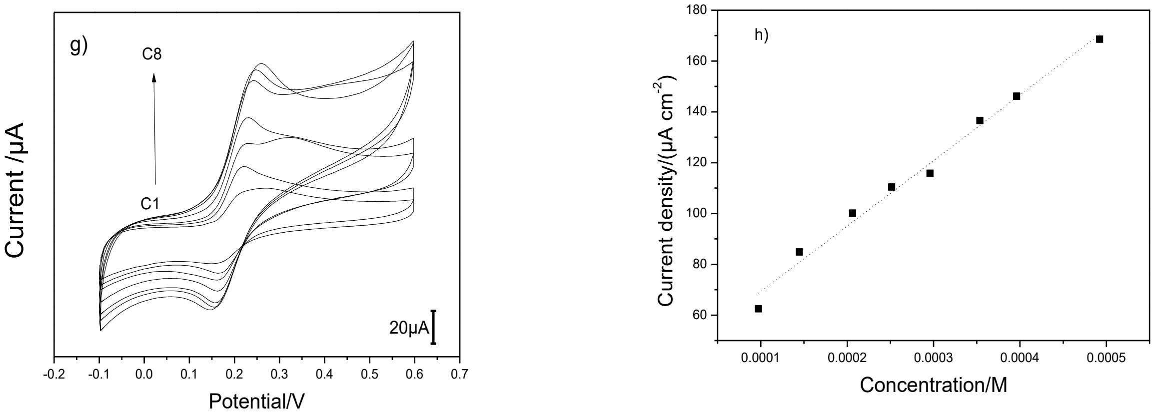

Figure 3.46 CVs and calibration curves recorded for 0.1-0.5 mM Dopamine in PBS (pH=7) at scan rate of 0.02 V s^{-1} on a,b).P-MWCNTs c,d).P-MWCNTs/HCl e,f).P-MWCNTs/piranha g,h) P-MWCNTs/piranha/ AuNPs (vs Ag/AgCl)

The quantitative analysis of the cyclic voltammogram in Figure 3.46 reveals that the acid treatment with HCl, the oxidative functionalisation as well as the surface modification with gold P-MWCNTs slightly change the detection limit and the sensitivity of P-MWCNTs in the determination of dopamine.

Table 3. 17 Estimated CV parameters for P-MWCNTs toward dopamine/dopamine quinone redox system

Films	ΔE_p/(V)	K_s/ (cm s^{-1})	Sensitivity/ (A mM^{-1} cm^{-2})	LOD/(µM)
P-MWCNTs	0.139	8.3 x10^{-4}	263.5	44.8
P-MWCNTs/HCl	0.119	1.1 x10^{-3}	267.2	45.3
P-MWCNTs/Piranha	0.104	1.5 x10^{-3}	265.6	50.9
P-MWCNTs/ AuNPs	0.068	9.1x10^{-3}	257.9	40.2

The EIS experiments were carried out in order to obtain the charge transfer resistance for electrooxidation of dopamine on different B-MWCNTs and P-MWCNTs electrodes. Figure 3.47 displays the impedance spectra over a 0.1 Hz – 100 KHz frequency range for 0.5 mM dopamine in PBS (pH=7) at different B-MWCNTs and P-MWCNTs electrodes. The impedance spectra are presented in Nyquist plots, where a semicircle in a high to medium frequency indicates the frame of electron transfer whereas a straight line in a low frequency illustrates the diffusion on the electrode surfaces.

A modified Randles equivalent circuit was used as a model to represent the physical process taking place in the system [185]. The R_{ct} results obtained from EIS spectra shown in Figures 3.47 and 3.48 are summarized in Table 3.18. A very small semicircle at the high to medium frequency region corresponds to the interfacial electron transport resistance on the electrode surfaces.

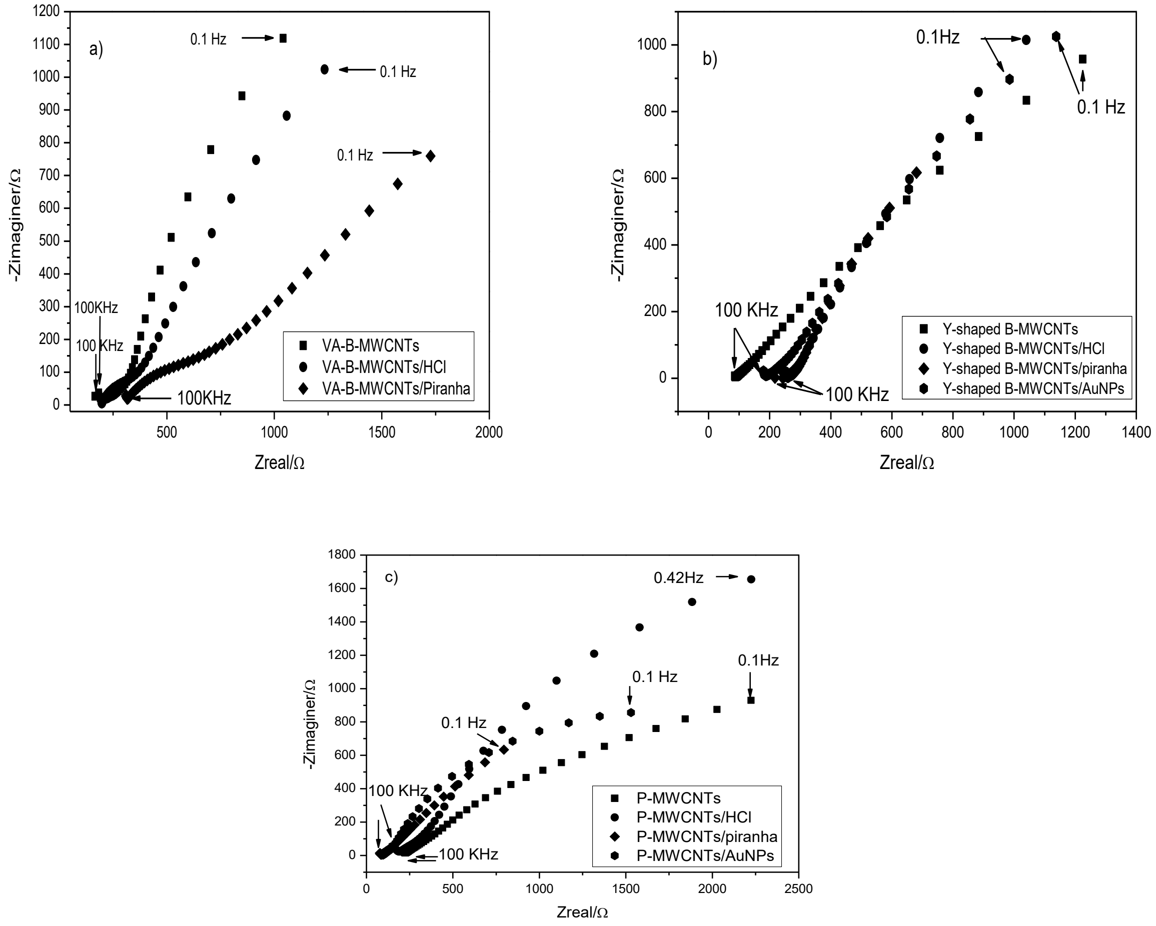

Figure 3.47 Electrochemical impedance spectra of various different electrodes of a). Vertically aligned B-MWCNTS b).Y-shaped B-MWCNTS c).P-MWCNTs in 0.25 mM dopamine (PBS pH=7) in a frequency range from 0.1Hz to 100 KHz.

As shown in Table 3.18, the charge transfer resistance increases with the following order : vertically aligned B-MWCNTs > vertically aligned B-MWCNTs/HCl > vertically aligned B-MWCNTs/piranha. The same electrochemical behavior was observed for the Y-shaped B-MWCNTs, Y-shaped B-MWCNTs/HCl and Y-shaped B-MWCNTs/AuNps. Owing to higher defect density on surface, the vertically aligned B-MWCNTs and Y-shaped B-MWCNTs treated with HCl possess a better electron transfer compared to the untreated film. It is known that the defect sites of carbon nanotubes are highly sensitive to molecule adsorption [186,187]. Partial blockage of B-MWCNTs surface by dopamine molecule afected the charge transfer resistance of electrode because of the limited access electrode surface to the solution. Hence, the dynamic range of dopamine analysis is limited by the partially blocked electrode. EIS studies reveal that B-MWCNTs and P-MWCNTs exhibits similar trend with different charge transfer resistance value toward dopamine/dopamine o-quinone redox sytem after acid treatment, oxidation with piranha and functionalization with AuNPs. The charge transfer resistance of B-MWCNTs and P-MWCNTs is reduced after acid treatment, oxidation with piranha and functionalization with AuNPs.

Table 3. 18 Estimated EIS parameters for B-MWCNTs and P-MWCNTs towards dopamine/dopamine quinone redox system

Films	$R_{ct}/(\Omega\ cm^{-2})$
Vertically aligned B-MWCNTs	96.8
Vertically aligned B-MWCNTs /HCl	60.3
Vertically aligned B-MWCNTs/Piranha	74.6
Y-shaped B-MWCNTs	43.1
Y-shaped B-MWCNTs/HCl	25.4
Y-shaped B-MWCNTs/Piranha	53.3
Y-shaped B-MWCNTs/ AuNPs	24.6
P-MWCNTs	51.6
P-MWCNTs/HCl	34.5
P-MWCNTs/Piranha	41.9
P-MWCNTs/ AuNPs	45.6

Chapter 4
Summary

The research work reports on fabrication of various B-MWCNTs and P-MWCNTs with different structure, namely vertically aligned, Y-shaped, cluster and horizontally oriented nanotubes on Si/SiO_2 by means of chemical vapour deposition. B-MWCNTs and P-MWCNTs were synthesized by using different doping and carbon sources materials. For the synthesis of the B-MWCNTs films, either ethanol or propanone was used as carbon sources, boric acid or triethyl borate was used as doping sources materials, while ferrocene was used as catalyst. For the production of P-MWCNTs films, either ethanol or cyclohexane was used as carbon source material, triphenyl phosphine was used as doping source, while ferrocene was applied as catalyst.

The B-MWCNTs and P-MWCNTs were characterized using scanning electron microscopy, transmission electron microscopy in conjunction with electron energy loss spectroscopy, X-ray photo electron spectroscopy as well as by means of Raman spectroscopy. The electrochemical properties of the produced B-MWCNTs and P-MWCNTs were investigated by means of cyclic voltammetry and impedance spectroscopy.

SEM analysis demonstrated that the structure and morphology of B-MWCNTs and P-MWCNTs are strongly affected by the doping source materials. Decomposition of ethyl alcohol and boric acid produces vertically aligned B-MWCNTs, decay of ethyl alcohol and triethyl borate produces Y-shaped B-MWCNTs while decomposition of ethyl alcohol and triphenyl phosphine results to sole P-MWCNTs with carbon nano cluster mixture. The difference in nanotube morphology was also observed for different carbon sources and catalyst/doping composition. Horizontally orientation B-MWCNTs with carbon nano cluster were produced with decomposition of propanone and triethyl borate. Depending on catalyst/doping ratio, decomposition of cyclohexane and triphenyl phosphine results to sole and cluster of P-MWCNTs.

TEM images show that vertically aligned B-MWCNTs and Y-shaped B-MWCNTs are free of nanographitic carbon cluster. Onion-like carbon is recognized as by-product of P-MWCNTs synthesis.

The effects of surface functionalisation with AuNPs, oxidation with piranha solution, and acid treatment with HCl on B-MWCNTs and P-MWCNTs were also studied. SEM and TEM analyses demonstrate that upon acid treatment with HCl the upper parts of vertically aligned B-MWCNTs and Y-shaped B-MWCNTs were eliminated. In addition, oxidation with piranha solution leads to elimination of the upper parts of vertically aligned B-MWCNTs and the nanotubes branch of Y-shaped B-MWCNTs

Raman spectra analysis exhibits that degree of defect density of produced B-MWCNTs and P-MWCNTs appeared to be different. The defect density of vertically aligned B-MWCNTs is higher than Y-shaped B-MWCNTs and P-MWCNTs cluster. The defect density of B-MWCNTs increases after acid treatments with HCl and oxidation with piranha solution. XPS analysis reveals that the amount of boron and iron of B-MWCNTs are drastically reduced after acid treatments with HCl.

Electrochemistry studies reveal that electrochemical behaviour of B-MWCNTs and P-MWCNTs toward $[Fe(CN)_6]^{3-/4-}$ and dopamine/dopamine quinone redox system are strongly affected by the nanotubes structure and configuration (sole nanotube or cluster nanotubes) as well as the presence of reaction by-product on the nanotube surface such as carbon cluster and onion-like carbon. Y-shaped B-MWCNTs are electrochemically faster toward $[Fe(CN)_6]^{3-/4-}$ and dopamine/dopamine quinone redox system compared to vertically aligned B-MWCNTs and P-MWCNTs with nanographitic carbon cluster. The surface functionalisation of vertically aligned B-MWCNTs and P-MWCNTs with AuNPs affects the electrochemical parameters of $[Fe(CN)_6]^{3-/4-}$ and dopamine/dopamine quinone redox system. It was established that upon AuNPs functionalisation an improvement of the kinetics of the electron transfer occurs.

References

[1] R.C. Alkire, P.N. Bartlett, J. Lipkowski, Electrochemistry of Carbon Electrodes, John Wiley & Sons, 2015.

[2] R.L. McCreery, Advanced carbon electrode materials for molecular electrochemistry, Chem. Rev. 108 (2008) 2646–2687. doi:10.1021/cr068076m.

[3] H.O. Pierson, The CVD of the Allotropes of Carbon, Handb. Chem. Vap. Depos. (1999) 185–216. doi:10.1016/B978-081551432-9.50010-3.

[4] C.E. Banks, R.G. Compton, New electrodes for old: from carbon nanotubes to edge plane pyrolytic graphite, Analyst. 131 (2006) 15–21. doi:10.1039/B512688F.

[5] G.E. Bacon, The interlayer spacing of graphite, Acta Crystallogr. 4 (1951) 558–561.

[6] F. De Nicola, P. Castrucci, M. Scarselli, F. Nanni, I. Cacciotti, M. De Crescenzi, Super-hydrophobic multi-walled carbon nanotube coatings for stainless steel, Nanotechnology. 26 (2015) 145701. doi:10.1088/0957-4484/26/14/145701.

[7] J.M. Nugent, K.S. V Santhanam, A. Rubio, P.M. Ajayan, Fast Electron Transfer Kinetics on Multiwalled Carbon Nanotube Microbundle Electrodes, Nano Lett. 1 (2001) 87–91. doi:10.1021/nl005521z.

[8] F. Maier, M. Riedel, B. Mantel, J. Ristein, L. Ley, Origin of surface conductivity in diamond, Phys. Rev. Lett. 85 (2000) 3472–3475. doi:10.1103/PhysRevLett.85.3472.

[9] A. Kraft, Doped Diamond: A Compact Review on a New, Versatile Electrode Material - Open Access Library, Int. J. Electrochem. Sci. 2 (2007) 355–385. doi:10.1021/jo026183k.

[10] W. Shi, J.K. Johnson, Gas Adsorption on Heterogeneous Single-Walled Carbon Nanotube Bundles, Phys. Rev. Lett. 91 (2003) 15504. doi:10.1103/PhysRevLett.91.015504.

[11] M. Valcárcel, S. Cárdenas, B.M. Simonet, Role of carbon nanotubes in analytical science, Anal. Chem. 79 (2007) 4788–4797. doi:10.1021/ac070196m.

[12] J.E. Padilha, R.G. Amorim, A.R. Rocha, A.J.R. Da Silva, A. Fazzio, Energetics and stability of vacancies in carbon nanotubes, Solid State Commun. 151 (2011) 482–486. doi:10.1016/j.ssc.2010.12.031.

[13] Q. Zhou, C. Wang, Z. Fu, H. Zhang, Y. Tang, Adsorption of formaldehyde molecule on Al-doped vacancy-defected single-walled carbon nanotubes: A theoretical study, Comput. Mater. Sci. 82 (2014) 337–344. doi:10.1016/j.commatsci.2013.09.046.

[14] B. Pan, B. Xing, Adsorption mechanisms of organic chemicals on carbon nanotubes, Environ. Sci. Technol. 42 (2008) 9005–9013. doi:10.1021/es801777n.

[15] C.E. Banks, T.J. Davies, G.G. Wildgoose, R.G. Compton, Electrocatalysis at graphite and

carbon nanotube modified electrodes: edge-plane sites and tube ends are the reactive sites., Chem. Commun. (Camb). (2005) 829–841. doi:10.1039/b413177k.

[16] P.G. Collins, Defects and Disorder in Carbon Nanotubes., in: Oxford Handb. Nanosci. Technol. Front. Adv., UC Irvine, 2010.

[17] C.-T. Lin, C.-Y. Lee, T.-S. Chin, R. Xiang, K. Ishikawa, J. Shiomi, S. Maruyama, Anisotropic electrical conduction of vertically-aligned single-walled carbon nanotube films, Carbon N. Y. 49 (2011) 1446–1452. doi:10.1016/j.carbon.2010.12.014.

[18] J.J. Gooding, R. Wibowo, J. Liu, W. Yang, D. Losic, S. Orbons, F.J. Mearns, J.G. Shapter, D.B. Hibbert, Protein electrochemistry using aligned carbon nanotube arrays, J. Am. Chem. Soc. 125 (2003) 9006–9007. doi:10.1021/ja035722f.

[19] A. V Krasheninnikov, K. Nordlund, J. Keinonen, Production of defects in supported carbon nanotubes under ion irradiation, Phys. Rev. B. 65 (2002) 165423. doi:Artn 165423\rDoi 10.1103/Physrevb.65.165423.

[20] D.-L. Feng, Y.-H. Feng, Y. Chen, W. Li, X.-X. Zhang, Effects of doping, Stone—Wales and vacancy defects on thermal conductivity of single-wall carbon nanotubes, Chinese Phys. B. 22 (2013) 16501. doi:10.1088/1674-1056/22/1/016501.

[21] L. Agüí, P. Yáñez-Sedeño, J.M. Pingarrón, Role of carbon nanotubes in electroanalytical chemistry. A review, Anal. Chim. Acta. 622 (2008) 11–47. doi:10.1016/j.aca.2008.05.070.

[22] M. Meyyappan, Carbon Nanotubes: Science and Applications, 2005.

[23] U.N. Maiti, W.J. Lee, J.M. Lee, Y. Oh, J.Y. Kim, J.E. Kim, J. Shim, T.H. Han, S.O. Kim, 25th anniversary article: chemically modified/doped carbon nanotubes & graphene for optimized nanostructures & nanodevices, Adv. Mater. 26 (2014) 40–67.

[24] M. Terrones, SCIENCE AND TECHNOLOGY OF THE TWENTY-FIRST CENTURY: Synthesis, Properties, and Applications of Carbon Nanotubes, Annu. Rev. Mater. Res. 33 (2003) 419–501. doi:10.1146/annurev.matsci.33.012802.100255.

[25] P.J.F. Harris, Carbon nanotube science: synthesis, properties and applications, Cambridge University Press, 2009.

[26] O. Zhou, R.M. Fleming, D.W. Murphy, C.H. Chen, R.C. Haddon, A.P. Ramirez, S.H. Glarum, Defects in carbon nanostructures, Science (80-.). 263 (1994) 1744–1748.

[27] I. Suarez-Martinez, G. Savini, A. Zobelli, M. Heggie, Dislocations in carbon nanotube walls, J. Nanosci. Nanotechnol. 7 (2007) 3417–3420.

[28] S.L. Mielke, D. Troya, S. Zhang, J.L. Li, S. Xiao, R. Car, R.S. Ruoff, G.C. Schatz, T. Belytschko, The role of vacancy defects and holes in the fracture of carbon nanotubes, Chem. Phys. Lett. 390 (2004) 413–420. doi:10.1016/j.cplett.2004.04.054.

[29] D. Bom, R. Andrews, D. Jacques, J. Anthony, B. Chen, M.S. Meier, J.P. Selegue,

Thermogravimetric Analysis of the Oxidation of Multiwalled Carbon Nanotubes: Evidence for the Role of Defect Sites in Carbon Nanotube Chemistry, Nano Lett. 2 (2002) 615–619. doi:10.1021/nl020297u.

[30] F. Banhart, J. Kotakoski, A. V. Krasheninnikov, Structural defects in graphene, ACS Nano. 5 (2011) 26–41. doi:10.1021/nn102598m.

[31] T.W. Ebbesen, T. Takada, Topological and SP3 defect structures in nanotubes, Carbon N. Y. 33 (1995) 973–978. doi:10.1016/0008-6223(95)00025-9.

[32] K. Suenaga, H. Wakabayashi, M. Koshino, Y. Sato, K. Urita, S. Iijima, Imaging active topological defects in carbon nanotubes., Nat. Nanotechnol. 2 (2007) 358–360. doi:10.1038/nnano.2007.141.

[33] A.J. Stone, D.J. Wales, Theoretical studies of icosahedral C60 and some related species, Chem. Phys. Lett. 128 (1986) 501–503. doi:10.1016/0009-2614(86)80661-3.

[34] F. Ding, A.R. Harutyunyan, B.I. Yakobson, Dislocation Theory of Chirality-Controlled Nanotube Growth, Proc. Natl. Acad. Sci. U. S. A. 106 (2009) 2506–9. doi:10.1073/pnas.0811946106.

[35] S. Reich, L. Li, J. Robertson, Structure and formation energy of carbon nanotube caps, Phys. Rev. B. 72 (2005) 8. doi:10.1103/PhysRevB.72.165423.

[36] J.C. Charlier, Defects in carbon nanotubes, Acc. Chem. Res. 35 (2002) 1063–1069. doi:10.1021/ar010166k.

[37] J.-C. Charlier, T. Ebbesen, P. Lambin, Structural and electronic properties of pentagon-heptagon pair defects in carbon nanotubes, Phys. Rev. B. 53 (1996) 11108–11113. doi:10.1103/PhysRevB.53.11108.

[38] M. Zhang, J. Li, Carbon nanotube in different shapes, Mater. Today. 12 (2009) 12–18. doi:10.1016/S1369-7021(09)70176-2.

[39] M. Kumar, Y. Ando, Chemical vapor deposition of carbon nanotubes: a review on growth mechanism and mass production., J. Nanosci. Nanotechnol. 10 (2010) 3739–3758. doi:10.1166/jnn.2010.2939.

[40] D. Dobrzańska-Danikiewicz,Anna D. Cichocki, MWCNTs manufactured by CCVD method, in: Carbon Nanotechnol., 2014: pp. 1–30.

[41] Y. Ando, X. Zhao, T. Sugai, M. Kumar, Growing carbon nanotubes, Mater. Today. 7 (2004) 22–29. doi:10.1016/S1369-7021(04)00446-8.

[42] W. Kern, Thin film processes II, Academic press, 2012.

[43] M. Argyle, C. Bartholomew, Heterogeneous Catalyst Deactivation and Regeneration: A Review, Catalysts. 5 (2015) 145–269. doi:10.3390/catal5010145.

[44] O.A. Nerushev, S. Dittmar, R.E. Morjan, F. Rohmund, E.E.B. Campbell, Particle size

dependence and model for iron-catalyzed growth of carbon nanotubes by thermal chemical vapor deposition, J. Appl. Phys. 93 (2003) 4185–4190. doi:10.1063/1.1559433.

[45] Q. Li, H. Yan, J. Zhang, Z. Liu, Effect of hydrocarbons precursors on the formation of carbon nanotubes in chemical vapor deposition, Carbon N. Y. 42 (2004) 829–835. doi:10.1016/j.carbon.2004.01.070.

[46] K. Hernadi, A. Fonseca, J.B. Nagy, A. Siska, I. Kiricsi, Production of nanotubes by the catalytic decomposition of different carbon-containing compounds, Appl. Catal. A Gen. 199 (2000) 245–255.

[47] Bonadiman, Lima, D. Andrade, Bergmann, Production of single and multi-walled carbon nanotubes using natural gas as a precursor compound, J. Mater. Sci. 41 (2006) 7288–7295. doi:10.1007/s10853-006-0938-2.

[48] Y. Murakami, Growth of vertically aligned single-walled carbon nanotube films on quartz substrates and their optical anisotropy, Chem. Phys. Lett. 385 (2004) 298–303. doi:10.1016/j.cplett.2003.12.095.

[49] S. Maruyama, R. Kojima, Y. Miyauchi, S. Chiashi, M. Kohno, Low-temperature synthesis of high-purity single-walled carbon nanotubes from alcohol, Chem. Phys. Lett. 360 (2002) 229–234.

[50] T. Tomie, S. Inoue, Y. Iba, Y. Matsumura, In situ mass spectroscopic analysis of alcohol catalytic chemical vapor deposition process for single-walled carbon nanotube, Chem. Phys. Lett. 536 (2012) 104–108. doi:10.1016/j.cplett.2012.03.099.

[51] R. Xiang, B. Hou, E. Einarsson, P. Zhao, S. Harish, K. Morimoto, Y. Miyauchi, S. Chiashi, Z. Tang, S. Maruyama, Carbon atoms in ethanol do not contribute equally to formation of single-walled carbon nanotubes, ACS Nano. 7 (2013) 3095–3103.

[52] E. Ordoñez-Casanova, M. Román-Aguirre, A. Aguilar-Elguezabal, F. Espinosa-Magaña, Synthesis of Carbon Nanotubes of Few Walls Using Aliphatic Alcohols as a Carbon Source, Materials (Basel). 6 (2013) 2534–2542. doi:10.3390/ma6062534.

[53] M. Bystrzejewski, A. Huczko, P. Byszewski, M. Domańska, M.H. Rümmeli, T. Gemming, H. Lange, Systematic Studies on Carbon Nanotubes Synthesis from Aliphatic Alcohols by the CVD Floating Catalyst Method, Fullerenes, Nanotub. Carbon Nanostructures. 17 (2009) 298–307. doi:10.1080/15363830902779577.

[54] L.A. Montoro, P. Corio, J.M. Rosolen, A comparative study of alcohols and ketones as carbon precursor for multi-walled carbon nanotube growth, Carbon N. Y. 45 (2007) 1234–1241. doi:10.1016/j.carbon.2007.01.025.

[55] Y. Zhang, J.M. Gregoire, R.B. Van Dover, A.J. Hart, Ethanol-promoted high-yield growth of few-walled carbon nanotubes, J. Phys. Chem. C. 114 (2010) 6389–6395. doi:10.1021/jp100358j.

[56] E. Segura-Cardenas, M. Reyes-Reyes, R. López-Sandoval, Effects of varying the content of alcohol in the reaction mixture on the graphitization of MWCNTs and their surface functionalization, J. Phys. Chem. C. 116 (2012) 9783–9792.

[57] S. Chaisitsak, J. Nukeaw, A. Tuantranont, Parametric study of atmospheric-pressure single-walled carbon nanotubes growth by ferrocene-ethanol mist CVD, Diam. Relat. Mater. 16 (2007) 1958–1966. doi:10.1016/j.diamond.2007.09.013.

[58] Y.-L. Li, L.-H. Zhang, X.-H. Zhong, A.H. Windle, Synthesis of high purity single-walled carbon nanotubes from ethanol by catalytic gas flow CVD reactions, Nanotechnology. 18 (2007) 225604. doi:10.1088/0957-4484/18/22/225604.

[59] A.M. and A.G.N. and E.I. Kauppinen, The role of metal nanoparticles in the catalytic production of single-walled carbon nanotubes—a review, J. Phys. Condens. Matter. 15 (2003) S3011. doi:10.1088/0953-8984/15/42/003.

[60] C.Q. Sun, Y. Wang, B.K. Tay, S. Li, H. Huang, Y.B. Zhang, Correlation between the melting point of a nanosolid and the cohesive energy of a surface atom, J. Phys. Chem. B. 106 (2002) 10701–10705. doi:10.1021/jp025868l.

[61] F. Danafar, A. Fakhru'l-Razi, M.A.M. Salleh, D.R.A. Biak, Fluidized bed catalytic chemical vapor deposition synthesis of carbon nanotubes-A review, Chem. Eng. J. 155 (2009) 37–48. doi:10.1016/j.cej.2009.07.052.

[62] K.J. MacKenzie, O.M. Dunens, A.T. Harris, An Updated Review of Synthesis Parameters and Growth Mechanisms for Carbon Nanotubes in Fluidized Beds, Ind. Eng. Chem. Res. 49 (2010) 5323–5338. doi:10.1021/ie9019787.

[63] A. Kukovecz, Z. Konya, N. Nagaraju, I. Willems, A. Tamasi, A. Fonseca, J.B. Nagy, I. Kiricsi, Catalytic synthesis of carbon nanotubes over Co{,} Fe and Ni containing conventional and sol-gel silica-aluminas, Phys. Chem. Chem. Phys. 2 (2000) 3071–3076. doi:10.1039/B002331K.

[64] A. Moisala, A.G. Nasibulin, D.P. Brown, H. Jiang, L. Khriachtchev, E.I. Kauppinen, Single-walled carbon nanotube synthesis using ferrocene and iron pentacarbonyl in a laminar flow reactor, Chem. Eng. Sci. 61 (2006) 4393–4402.

[65] G.S.B. McKee, K.S. Vecchio, Thermogravimetric analysis of synthesis variation effects on CVD generated multiwalled carbon nanotubes, J. Phys. Chem. B. 110 (2006) 1179–1186.

[66] A. Leonhardt, M. Ritschel, D. Elefant, N. Mattern, K. Biedermann, S. Hampel, C. Müller, T. Gemming, B. Büchner, Enhanced magnetism in Fe-filled carbon nanotubes produced by pyrolysis of ferrocene, J. Appl. Phys. 98 (2005) 74315.

[67] D. Yuan, L. Ding, H. Chu, Y. Feng, T.P. McNicholas, J. Liu, Horizontally aligned single-walled carbon nanotube on quartz from a large variety of metal catalysts, Nano Lett. 8 (2008) 2576–2579. doi:10.1021/nl801007r.

[68] D. Takagi, Y. Homma, H. Hibino, S. Suzuki, Y. Kobayashi, Single-walled carbon nanotube growth from highly activated metal nanoparticles, Nano Lett. 6 (2006) 2642–2645. doi:10.1021/nl061797g.

[69] C.L. Pint, N. Nicholas, S.T. Pheasant, J.G. Duque, a. N.G. Parra-Vasquez, G. Eres, M. Pasquali, R.H. Hauge, Temperature and Gas Pressure Effects in Vertically Aligned Carbon Nanotube Growth from Fe–Mo Catalyst, J. Phys. Chem. C. 112 (2008) 14041–14051. doi:10.1021/jp8025539.

[70] S. Noda, H. Sugime, T. Osawa, Y. Tsuji, S. Chiashi, Y. Murakami, S. Maruyama, A simple combinatorial method to discover Co-Mo binary catalysts that grow vertically aligned single-walled carbon nanotubes, Carbon N. Y. 44 (2006) 1414–1419. doi:10.1016/j.carbon.2005.11.026.

[71] J. Zhang, J.-O. Müller, W. Zheng, D. Wang, D. Su, R. Schlögl, Individual Fe-Co alloy nanoparticles on carbon nanotubes: structural and catalytic properties., Nano Lett. 8 (2008) 2738–43. doi:10.1021/nl8011984.

[72] Y. Li, W. Kim, Y. Zhang, M. Rolandi, D. Wang, H. Dai, Growth of single-walled carbon nanotubes from discrete catalytic nanoparticles of various sizes, J. Phys. Chem. B. 105 (2001) 11424–11431. doi:10.1021/jp012085b.

[73] A. Kurtz, H. Park, C.M. Lieber, Diameter-controlled synthesis of carbon nanotubes, J. Phys. Chem. B. 106 (2002) 2429–2433.

[74] A. Reina, M. Hofmann, D. Zhu, J. Kong, Growth Mechanism of Long and Horizontally Aligned Carbon Nanotubes by Chemical Vapor Deposition, J. Phys. Chem. 111 (2007) 7292–7297. doi:10.1021/jp0711500.

[75] a Bachmatiuk, E. Borowiak-Palen, R.J. Kalenczuk, Advances in engineering of diameter and distribution of the number of walls of carbon nanotubes in alcohol CVD., Nanotechnology. 19 (2008) 365605. doi:10.1088/0957-4484/19/36/365605.

[76] B.H. Hong, J.Y. Lee, T. Beetz, Y. Zhu, P. Kim, K.S. Kim, Quasi-continuous growth of ultralong carbon nanotube arrays, J. Am. Chem. Soc. 127 (2005) 15336–15337. doi:10.1021/ja054454d.

[77] A. Becker, Z. Hu, K.J. Hüttinger, Hydrogen inhibition model of carbon deposition from light hydrocarbons, Fuel. 79 (2000) 1573–1580. doi:10.1016/S0016-2361(00)00030-2.

[78] Y. Liu, W.Z. Qian, Q. Zhang, G.Q. Ning, G.H. Luo, Y. Wang, D.Z. Wang, F. Wei, Synthesis of high-quality, double-walled carbon nanotubes in a fluidized bed reactor, Chem. Eng. Technol. 32 (2009) 73.

[79] G. Ortega-Cervantez, G. Rueda-Morales, J. Ortiz-López, Catalytic CVD production of carbon nanotubes using ethanol, in: Microelectronics J., 2005: pp. 495–498. doi:10.1016/j.mejo.2005.02.062.

[80] J.-P. Tessonnier, D.S. Su, Recent progress on the growth mechanism of carbon nanotubes: a review., ChemSusChem. 4 (2011) 824–847. doi:10.1002/cssc.201100175.

[81] R.S. Wagner, W.C. Ellis, The vapor-liquid-solid mechanism of crystal growth and its application to silicon, Trans Met. Soc AIME. (1965). doi:10.1063/1.1753975.

[82] R.T.K. Baker, M.A. Barber, P.S. Harris, F.S. Feates, R.J. Waite, Nucleation and growth of carbon deposits from the nickel catalyzed decomposition of acetylene, J. Catal. 26 (1972) 51–62. doi:10.1016/0021-9517(72)90032-2.

[83] Y. Saito, Nanoparticles and filled nanocapsules, Carbon N. Y. 33 (1995) 979–988. doi:10.1016/0008-6223(95)00026-A.

[84] R.T.K. Baker, P.S. Harris, R.B. Thomas, R.J. Waite, Formation of filamentous carbon from iron, cobalt and chromium catalyzed decomposition of acetylene, J. Catal. 30 (1973) 86–95. doi:10.1016/0021-9517(73)90055-9.

[85] A. Oberlin, M. Endo, T. Koyama, Filamentous growth of carbon through benzene decomposition, J. Cryst. Growth. 32 (1976) 335–349. doi:10.1016/0022-0248(76)90115-9.

[86] H. Terrones, T. Hayashi, M. Muñoz-Navia, M. Terrones, Y.A. Kim, N. Grobert, R. Kamalakaran, J. Dorantes-Dávila, R. Escudero, M.S. Dresselhaus, M. Endo, Graphitic cones in palladium catalysed carbon nanofibres, Chem. Phys. Lett. 343 (2001) 241–250. doi:10.1016/S0009-2614(01)00718-7.

[87] C.J. Lee, J. Park, Growth model of bamboo-shaped carbon nanotubes by thermal chemical vapor deposition, Appl. Phys. Lett. 77 (2000) 3397–3399.

[88] J.M. Romo-Herrera, D.A. Cullen, E. Cruz-Silva, D. Ramírez, B.G. Sumpter, V. Meunier, H. Terrones, D.J. Smith, M. Terrones, The Role of Sulfur in the Synthesis of Novel Carbon Morphologies: From Covalent Y-Junctions to Sea-Urchin-Like Structures, Adv. Funct. Mater. 19 (2009) 1193–1199. doi:10.1002/adfm.200800931.

[89] J.W. Jang, C.E. Lee, S.C. Lyu, T.J. Lee, C.J. Lee, Structural study of nitrogen-doping effects in bamboo-shaped multiwalled carbon nanotubes, Appl. Phys. Lett. 84 (2004) 2877–2879. doi:10.1063/1.1697624.

[90] J.C. Slater, Atomic Radii in Crystals, J. Chem. Phys. 41 (1964) 3199. doi:10.1063/1.1725697.

[91] W. An, C.H. Turner, Chemisorption of transition-metal atoms on boron-and nitrogen-doped carbon nanotubes: energetics and geometric and electronic structures, J. Phys. Chem. C. 113 (2009) 7069–7078.

[92] S. Jalili, M. Akhavan, J. Schofield, Electronic and Structural Properties of BC3 Nanotubes with Defects, J. Phys. Chem. C. 116 (2012) 13225–13230.

[93] D. Carroll, P. Redlich, X. Blase, J.-C. Charlier, S. Curran, P. Ajayan, S. Roth, M. Rühle, Effects of Nanodomain Formation on the Electronic Structure of Doped Carbon Nanotubes, Phys. Rev. Lett. 81 (1998) 2332–2335. doi:10.1103/PhysRevLett.81.2332.

[94] E. Borowiak-Palen, T. Pichler, G.G. Fuentes, A. Graff, R.J. Kalenczuk, M. Knupfer, J. Fink, Efficient production of B-substituted single-wall carbon nanotubes, Chem. Phys. Lett. 378 (2003) 516–520. doi:10.1016/S0009-2614(03)01324-1.

[95] W. Han, Y. Bando, K. Kurashima, T. Sato, Boron-doped carbon nanotubes prepared through a substitution reaction, Chem. Phys. Lett. 299 (1999) 368–373. doi:10.1016/S0009-2614(98)01307-4.

[96] S. Shiraishi, M. Kibe, T. Yokoyama, H. Kurihara, N. Patel, A. Oya, Y. Kaburagi, Y. Hishiyama, Electric double layer capacitance of multi-walled carbon nanotubes and B-doping effect, Appl. Phys. A Mater. Sci. Process. 82 (2006) 585–591.

[97] Y. Sato, H. Nishizaka, K. Motomiya, G. Yamamoto, A. Okubo, H. Kimura, M. Ishikuro, K. Wagatsuma, T. Hashida, K. Tohji, Boron-assisted transformation to rod-like graphitic carbons from multi-walled carbon nanotubes in boron-mixed multi-walled carbon nanotube solids, ACS Appl. Mater. Interfaces. 3 (2011) 2431–2439. doi:10.1021/am200335n.

[98] R.J. Nicholls, Z. Aslam, M.C. Sarahan, A. Koós, J.R. Yates, P.D. Nellist, N. Grobert, Boron-mediated nanotube morphologies, ACS Nano. 6 (2012) 7800–7805. doi:10.1021/nn301770b.

[99] B.C. Satishkumar, A. Govindaraj, K.R. Harikumar, J.-P. Zhang, A.K. Cheetham, C.N.R. Rao, Boron–carbon nanotubes from the pyrolysis of C 2 H 2–B 2 H 6 mixtures, Chem. Phys. Lett. 300 (1999) 473–477.

[100] S. Ishii, T. Watanabe, S. Ueda, S. Tsuda, T. Yamaguchi, Y. Takano, Resistivity reduction of boron-doped multiwalled carbon nanotubes synthesized from a methanol solution containing boric acid, Appl. Phys. Lett. 92 (2008) 202116.

[101] P. Ayala, W. Plank, A. Grüneis, E.I. Kauppinen, M.H. Rümmeli, H. Kuzmany, T. Pichler, A one step approach to B-doped single-walled carbon nanotubes, J. Mater. Chem. 18 (2008) 5676. doi:10.1039/b809050e.

[102] K.C. Mondal, N.J. Coville, M.J. Witcomb, G. Tejral, J. Havel, Boron mediated synthesis of multiwalled carbon nanotubes by chemical vapor deposition, Chem. Phys. Lett. 437 (2007) 87–91. doi:10.1016/j.cplett.2007.01.079.

[103] R.B. Patel, T. Chou, A. Kanwal, D.J. Apigo, J. Lefebvre, F. Owens, Z. Iqbal, Boron-Filled Hybrid Carbon Nanotubes, Sci. Rep. 6 (2016).

[104] D.G. Larrude, M.E.H. Maia da Costa, F.H. Monteiro, A.L. Pinto, F.L. Freire Jr, Characterization of phosphorus-doped multiwalled carbon nanotubes, J. Appl. Phys. 111 (2012) 64315.

[105] E. Cruz-silva, D. a Cullen, L. Gu, J.M. Romo-herrera, E. Muñoz-sandoval, F. López-urías, B.G. Sumpter, V. Meunier, J. Charlier, Ḱ.D.J. Smith, H. Terrones, M. Terrones, Heterodoped Nanotubes: Theory, Synthesis, and Characterization of Phosphorus_Nitrogen Doped Multiwalled Carbon Nanotubes, ACS Nano. 2 (2008) 441–448. doi:10.1021/am200933m.

[106] E. Cruz-Silva, F. López-Urías, E. Miñoz-Sandoval, B.G. Sumpter, H. Terrones, J.C. Charlier, V. Meunier, M. Terrones, Electronic transport and mechanical properties of phosphorus- and phosphorus-nitrogen-doped carbon nanotubes, ACS Nano. 3 (2009) 1913–1921. doi:10.1021/nn900286h.

[107] V. Griadun, Doped Carbon Nanotube Properties, in: InTech, Rijeka, 2010: p. Ch. 0. doi:10.5772/39423.

[108] V. Jourdain, O. Stéphan, M. Castignolles, A. Loiseau, P. Bernier, Controlling the morphology of multiwalled carbon nanotubes by sequential catalytic growth induced by phosphorus, Adv. Mater. 16 (2004) 447–453.

[109] G. Ruiz-Soria, T. Susi, M. Sauer, K. Yanagi, T. Pichler, P. Ayala, On the bonding environment of phosphorus in purified doped single-walled carbon nanotubes, Carbon N. Y. 81 (2015) 91–95. doi:10.1016/j.carbon.2014.09.028.

[110] J. Xu, L. Guan, Diameter-selective band structure modification of single-walled carbon nanotubes by encapsulated phosphorus chains, J. Phys. Chem. C. 113 (2009) 15099–15101.

[111] P.X. Hou, C. Liu, H.M. Cheng, Purification of carbon nanotubes, Carbon N. Y. 46 (2008) 2003–2025. doi:10.1016/j.carbon.2008.09.009.

[112] D.B. Mawhinney, V. Naumenko, A. Kuznetsova, J.T. Yates, J. Liu, R.E. Smalley, Surface defect site density on single walled carbon nanotubes by titration, Chem. Phys. Lett. 324 (2000) 213–216.

[113] G. Hajime, F. Terumi, F. Yoshiya, O. Toshiyuki, Method of purifying single wall carbon nanotubes from metal catalyst impurities, Honda Giken Kogyo Kabushiki Kaisha, Japan. (2002).

[114] A. Bonard, J. M., Stora, T., Salvetat, J. P., Maier, F., Stöckli, T., Duschl, Châtelain, Purification and size-selection of carbon nanotubes, Adv. Mater. 9 (1997) 827–831. doi:10.1002/adma.19970091014.

[115] K.J. Ziegler, Z. Gu, H. Peng, E.L. Flor, R.H. Hauge, R.E. Smalley, Controlled oxidative cutting of single-walled carbon nanotubes, J. Am. Chem. Soc. 127 (2005) 1541–1547. doi:10.1021/ja044537e.

[116] K.J. Ziegler, Z. Gu, J. Shaver, Z. Chen, E.L. Flor, D.J. Schmidt, C. Chan, R.H. Hauge, R.E. Smalley, Cutting single-walled carbon nanotubes, Nanotechnology. 16 (2005) S539–S544. doi:10.1088/0957-4484/16/7/031.

[117] X. Li, Y. Liu, L. Fu, L. Cao, D. Wei, Y. Wang, Efficient synthesis of carbon nanotube-nanoparticle hybrids, Adv. Funct. Mater. 16 (2006) 2431–2437. doi:10.1002/adfm.200600339.

[118] Z. Chen, W. Thiel, A. Hirsch, Reactivity of the convex and concave surfaces of single-walled carbon nanotubes (SWCNTs) towards addition reactions: Dependence on the carbon-atom pyramidalization, ChemPhysChem. 4 (2003) 93–97. doi:10.1002/cphc.200390015.

[119] Y. Gogotsi, Nanotubes and nanofibers, CRC press, 2006.

[120] S. Niyogi, M.A. Hamon, H. Hu, B. Zhao, P. Bhowmik, R. Sen, M.E. Itkis, R.C. Haddon, Chemistry of single-walled carbon nanotubes, Acc. Chem. Res. 35 (2002) 1105–1113. doi:10.1021/ar010155r.

[121] T.J. Davies, C.E. Banks, R.G. Compton, Voltammetry at spatially heterogeneous electrodes, J. Solid State Electrochem. 9 (2005) 797–808. doi:10.1007/s10008-005-0699-x.

[122] S. Reich, C. Thomsen, Chirality dependence of the density-of-states singularities in carbon nanotubes, Phys. Rev. B. 62 (2000) 4273.

[123] I. Cabria, J. Mintmire, C. White, Metallic and semiconducting narrow carbon nanotubes, Phys. Rev. B. 67 (2003) 4–7. doi:10.1103/PhysRevB.67.121406.

[124] Aq. Chen, Q. Shao, Z. Lin, Effects of phosphorus-doping upon the electronic structures of single wall carbon nanotubes, Science (80-.). 52 (2011) 9. doi:10.1007/s11433-009-0145-7.

[125] J.-W. Wei, H.-F. Hu, H. Zeng, Z.-Y. Wang, L. Wang, L.-J. Zhang, Influence of boron distribution on the transport of single-walled carbon nanotube, Appl. Phys. A Mater. Sci. Process. 89 (2007) 789–792.

[126] P. Szroeder, Electron transfer kinetics at single-walled carbon nanotube paper: The role of band structure, Phys. E Low-Dimensional Syst. Nanostructures. 44 (2011) 470–475. doi:10.1016/j.physe.2011.09.024.

[127] I. Heller, J. Kong, K.A. Williams, C. Dekker, S.G. Lemay, Electrochemistry at single-walled carbon nanotubes: The role of band structure and quantum capacitance, J. Am. Chem. Soc. 128 (2006) 7353–7359. doi:10.1021/ja061212k.

[128] P.G. Collins, P. Avouris, Intershell conductance of multiwalled carbon nanotubes, AIP Conf. Proc. (2002) 223–226. doi:10.1063/1.1514110.

[129] F.G. Chevallier, T.J. Davies, O. V. Klymenko, L. Jiang, T.G.J. Jones, R.G. Compton, Numerical simulation of partially blocked electrodes under cyclic voltammetry conditions: Influence of the block unit geometry on the global electrochemical properties, J. Electroanal. Chem. 577 (2005) 211–221. doi:10.1016/j.jelechem.2004.11.033.

[130] X. Luo, A. Morrin, A.J. Killard, M.R. Smyth, Application of nanoparticles in electrochemical sensors and biosensors, Electroanalysis. 18 (2006) 319–326. doi:10.1002/elan.200503415.

[131] J. Kruusma, N. Mould, K. Jurkschat, A. Crossley, C.E. Banks, Single walled carbon nanotubes contain residual iron oxide impurities which can dominate their electrochemical activity, Electrochem. Commun. 9 (2007) 2330–2333. doi:10.1016/j.elecom.2007.06.024.

[132] C.M. Welch, R.G. Compton, The use of nanoparticles in electroanalysis: a review, Anal. Bioanal. Chem. 384 (2006) 601–619.

[133] F.S. Greenspan, D.G. Gardner, Basic & clinical endocrinology, Appleton & Lange Stamford, CT, 1997.

[134] D.L. Robinson, A. Hermans, A.T. Seipel, R.M. Wightman, Monitoring rapid chemical communication in the brain, Chem. Rev. 108 (2008) 2554–2584. doi:10.1021/cr068081q.

[135] Y. Li, M. Liu, C. Xiang, Q. Xie, S. Yao, Electrochemical quartz crystal microbalance study on growth and property of the polymer deposit at gold electrodes during oxidation of dopamine in aqueous solutions, Thin Solid Films. 497 (2006) 270–278. doi:10.1016/j.tsf.2005.10.048.

[136] P.J. Britto, K.S. V Santhanam, P.M. Ajayan, Carbon nanotube electrode for oxidation of dopamine, in: Bioelectrochemistry Bioenerg., 1996: pp. 121–125. doi:10.1016/0302-4598(96)05078-7.

[137] S.H. DuVall, R.L. McCreery, Control of catechol and hydroquinone electron-transfer kinetics on native and modified glassy carbon electrodes, Anal. Chem. 71 (1999) 4594–4602. doi:10.1021/ac990399d.

[138] Y. Wang, Y. Li, L. Tang, J. Lu, J. Li, Application of graphene-modified electrode for selective detection of dopamine, Electrochem. Commun. 11 (2009) 889–892. doi:10.1016/j.elecom.2009.02.013.

[139] N.G. Tsierkezos, U. Ritter, Synthesis and electrochemistry of multiwalled carbon nanotube films directly attached on silica substrate, J. Solid State Electrochem. 14 (2010) 1101–1107. doi:10.1007/s10008-009-0924-0.

[140] J.M. Köhler, S. Li, A. Knauer, Why is micro segmented flow particularly promising for the synthesis of nanomaterials?, Chem. Eng. Technol. 36 (2013) 887–899.

[141] L. Hafermann, J.M. Köhler, Photochemical Micro Continuous-Flow Synthesis of Noble Metal Nanoparticles of the Platinum Group, Chem. Eng. Technol. 38 (2015) 1138–1143.

[142] J.H. Lehman, M. Terrones, E. Mansfield, K.E. Hurst, V. Meunier, Evaluating the characteristics of multiwall carbon nanotubes, Carbon N. Y. 49 (2011) 2581–2602.

doi:10.1016/j.carbon.2011.03.028.

[143] A. Jorio, M.A. Pimenta, A.G. Souza Filho, R. Saito, G. Dresselhaus, M.S. Dresselhaus, Characterizing carbon nanotube samples with resonance Raman scattering, New J. Phys. 5 (2003). doi:10.1088/1367-2630/5/1/139.

[144] R. Saito, A. Jorio, A.G. Souza Filho, G. Dresselhaus, M.S. Dresselhaus, M.A. Pimenta, Probing phonon dispersion relations of graphite by double resonance Raman scattering, Phys. Rev. Lett. 88 (2002) 274011–274014. doi:10.1103/PhysRevLett.88.020601.

[145] R.A. DiLeo, B.J. Landi, R.P. Raffaelle, Purity assessment of multiwalled carbon nanotubes by Raman spectroscopy, J. Appl. Phys. 101 (2007). doi:10.1063/1.2712152.

[146] M. Himmerlich, S. Krischok, V. Lebedev, O. Ambacher, J.A. Schaefer, Morphology and surface electronic structure of MBE grown InN, J. Cryst. Growth. 306 (2007) 6–11.

[147] R.S. Nicholson, Theory and Application of Cyclic Voltammetry f m Measurement of Electrode Reaction Kinetics, Anal. Chem. 37 (1965) 1351–1355. doi:10.1021/ac60230a016.

[148] J.E.B. Randles, Kinetics of rapid electrode reactions, Discuss. Faraday Soc. 1 (1947) 11–19.

[149] M.S. Dresselhaus, P.C. Eklund, Phonons in carbon nanotubes, Adv. Phys. 49 (2000) 705–814. doi:10.1080/000187300413184.

[150] J. Maultzsch, S. Reich, C. Thomsen, S. Webster, R. Czerw, D.L. Carroll, S.M.C. Vieira, P.R. Birkett, C.A. Rego, Raman characterization of boron-doped multiwalled carbon nanotubes, Appl. Phys. Lett. 81 (2002) 2647–2649. doi:10.1063/1.1512330.

[151] D. Hulicova-Jurcakova, M. Seredych, G.Q. Lu, N.K.A.C. Kodiweera, P.E. Stallworth, S. Greenbaum, T.J. Bandosz, Effect of surface phosphorus functionalities of activated carbons containing oxygen and nitrogen on electrochemical capacitance, Carbon N. Y. 47 (2009) 1576–1584. doi:10.1016/j.carbon.2009.02.006.

[152] F. Tuinstra, J.L. Koenig, Raman Spectrum of Graphite, J. Chem. Phys. 53 (1970) 1126–1130. doi:10.1063/1.1674108.

[153] S. Costa, E. Borowiak-Palen, Raman study on doped multiwalled carbon nanotubes, Acta Phys. Pol. A. 116 (2009) 32–35.

[154] V. Datsyuk, M. Kalyva, K. Papagelis, J. Parthenios, D. Tasis, A. Siokou, I. Kallitsis, C. Galiotis, Chemical oxidation of multiwalled carbon nanotubes, Carbon N. Y. 46 (2008) 833–840. doi:10.1016/j.carbon.2008.02.012.

[155] H.-B. Zhang, G.-D. Lin, Z.-H. Zhou, X. Dong, T. Chen, Raman spectra of MWCNTs and MWCNT-based H 2-adsorbing system, Carbon N. Y. 40 (2002) 2429–2436.

[156] N.G. Tsierkezos, U. Ritter, Y.N. Thaha, C. Downing, P. Szroeder, Synthesis,

characterization, and electrochemical application of phosphorus-doped multi-walled carbon nanotubes, J. Solid State Electrochem. 19 (2015) 891–905.

[157] L.P. Biró, Z.E. Horváth, G.I. Márk, Z. Osváth, A.A. Koós, A.M. Benito, W. Maser, P. Lambin, Carbon nanotube Y junctions: Growth and properties, Diam. Relat. Mater. 13 (2004) 241–249. doi:10.1016/j.diamond.2003.10.014.

[158] G.E. Scuseria, Negative curvature and hyperfullerenes, Chem. Phys. Lett. 195 (1992) 534–536. doi:10.1016/0009-2614(92)85558-R.

[159] T.I.T. Okpalugo, P. Papakonstantinou, H. Murphy, J. McLaughlin, N.M.D. Brown, High resolution XPS characterization of chemical functionalised MWCNTs and SWCNTs, Carbon N. Y. 43 (2005) 153–161. doi:10.1016/j.carbon.2004.08.033.

[160] N.G. Tsierkezos, U. Ritter, Y.N. Thaha, S. Krischok, M. Himmerlich, C. Downing, Properties and electrochemical characteristics of boron-doped multi-walled carbon nanotubes, Chem. Phys. Lett. 639 (2015) 217–224.

[161] W.M. Silva, H. Ribeiro, L.M. Seara, H.D.R. Calado, A.S. Ferlauto, R.M. Paniago, C.F. Leite, G.G. Silva, Surface properties of oxidized and aminated multi-walled carbon nanotubes, J. Braz. Chem. Soc. 23 (2012) 1078–1086.

[162] R. Ekins, P. Edwards, On the meaning of "sensitivity," Clin. Chem. 43 (1997) 1824–1831.

[163] G.L. Long, J.D. Winefordner, Limit of detection. A closer look at the IUPAC definition, Anal. Chem. 55 (1983) 712A–724A.

[164] I. Taurino, S. Carrara, M. Giorcelli, A. Tagliaferro, G. De Micheli, Comparing sensitivities of differently oriented multi-walled carbon nanotubes integrated on silicon wafer for electrochemical biosensors, Sensors Actuators B Chem. 160 (2011) 327–333.

[165] M. Pandurangachar, B.E. Kumara Swamy, B.N. Chandrashekar, O. Gilbert, S. Reddy, B.S. Sherigara, Electrochemical investigations of potassium ferricyanide and dopamine by 1-butyl-4-methylpyridinium tetrafluoro borate modified carbon paste electrode: A cyclic voltammetric study, Int. J. Electrochem. Sci. 5 (2010) 1187–1202.

[166] B.N. Chandrashekar, B.E.K. Swamy, M. Pandurangachar, S.S. Shankar, O. Gilbert, J.G. Manjunatha, B.S. Sherigara, Electrochemical oxidation of dopamine at polyethylene glycol modified carbon paste electrode: a cyclic voltammetric study, Int. J. Electrochem. Sci. 5 (2010) 578–592.

[167] E. Barsoukov, J.R. Macdonald, Impedance Spectroscopy: Theory, Experiment, and Applications, 2005. doi:10.1002/0471716243.

[168] Y. Barsukov, J.R. Macdonald, Electrochemical impedance spectroscopy, Charact. Mater. (2012).

[169] A. Bard, T., Faulkner, LR, 1980. Electrochemical Methods, Fundam. Appl. (n.d.).

[170] N.G. Tsierkezos, P. Szroeder, U. Ritter, Multi-walled carbon nanotubes as electrode materials for electrochemical studies of organometallic compounds in organic solvent media, Monatshefte Für Chemie-Chemical Mon. 142 (2011) 233–242.

[171] A. Ambrosi, M. Pumera, Amorphous carbon impurities play an active role in redox processes of carbon nanotubes, J. Phys. Chem. C. 115 (2011) 25281–25284. doi:10.1021/jp209734t.

[172] M.D. Levi, D. Aurbach, Impedance of a single intercalation particle and of non-homogeneous, multilayered porous composite electrodes for Li-ion batteries, J. Phys. Chem. B. 108 (2004) 11693–11703. doi:10.1021/jp0486402.

[173] J.P. Meyers, M. Doyle, R.M. Darling, J. Newman, The Impedance Response of a Porous Electrode Composed of Intercalation Particles, J. Electrochem. Soc. 147 (2000) 2930. doi:10.1149/1.1393627.

[174] C.E. Banks, T.J. Davies, G.G. Wildgoose, R.G. Compton, Electrocatalysis at graphite and carbon nanotube modified electrodes: edge-plane sites and tube ends are the reactive sites, Chem. Commun. (2005) 829. doi:10.1039/b413177k.

[175] J. McDonough, Y. Gogotsi, Carbon Onions: Synthesis and Electrochemical Applications, Electrochem. Soc. Interface. 22 (2013) 61–66. doi:http://electrochem.org/dl/interface/fal/fal13/fal13_p61_66.pdf.

[176] D.A.C. Brownson, C.W. Foster, C.E. Banks, The electrochemical performance of graphene modified electrodes: An analytical perspective, Analyst. 137 (2012) 1815. doi:10.1039/c2an16279b.

[177] X. Li, J.P. Rong, B.Q. Wei, Electrochemical Behavior of Single-Walled Carbon Nanotube Supercapacitors under Compressive Stress, ACS Nano. 4 (2010) 6039–6049. doi:10.1021/nn101595y.

[178] M. Poon, R.L. McCreery, In situ laser activation of glassy carbon electrodes, Anal. Chem. 58 (1986) 2745–2750.

[179] F.C. Moraes, M.F. Cabral, L.H. Mascaro, S.A.S. Machado, The electrochemical effect of acid functionalisation of carbon nanotubes to be used in sensors development, Surf. Sci. 605 (2011) 435–440.

[180] S. Senoh, C.R. Creveling, S. Udenfriend, B. Witkop, Chemical, Enzymatic and Metabolic Studies on the Mechanism of Oxidation of Dopamine1, J. Am. Chem. Soc. 81 (1959) 6236–6240. doi:10.1021/ja01532a030.

[181] C. Deng, J. Chen, M. Wang, C. Xiao, Z. Nie, S. Yao, A novel and simple strategy for selective and sensitive determination of dopamine based on the boron-doped carbon nanotubes modified electrode, Biosens. Bioelectron. 24 (2009) 2091–2094. doi:10.1016/j.bios.2008.10.022.

[182] K. Wu, J. Fei, S. Hu, Simultaneous determination of dopamine and serotonin on a glassy

carbon electrode coated with a film of carbon nanotubes, Anal. Biochem. 318 (2003) 100–106.

[183] R.A. Marcus, On the theory of oxidation-reduction reactions involving electron transfer. I, J. Chem. Phys. 24 (1956) 966–978.

[184] M.E. Rice, Z. Galus, R.N. Adams, Graphite paste electrodes. Effects of Paste compositions and surface states on Electron-Transfer rates, J. Electroanal. Chem. Interfacial Electrochem. 143 (1983) 89–102. doi:10.1016/S0022-0728(83)80256-3.

[185] N.G. Tsierkezos, U. Ritter, Oxidation of dopamine on multi-walled carbon nanotubes, J. Solid State Electrochem. 16 (2012) 2217–2226.

[186] X. Feng, S. Irle, H. Witek, K. Morokuma, R. Vidic, E. Borguet, Sensitivity of ammonia interaction with single-walled carbon nanotube bundles to the presence of defect sites and functionalities, J. Am. Chem. Soc. 127 (2005) 10533–10538.

[187] M. Grujicic, G. Cao, R. Singh, The effect of topological defects and oxygen adsorption on the electronic transport properties of single-walled carbon-nanotubes, Appl. Surf. Sci. 211 (2003) 166–183.